Magnetic X-ray Spectroscopy Studies of Dilute Magnetic Semiconductors

Adam Alexander Freeman, MSci (Hons)

Thesis submitted to the University of Nottingham

for the degree of Doctor of Philosophy

February 2009

Abstract

Dilute magnetic semiconductors are an important family of materials that have many potential applications in spintronics; (Ga,Mn)As, (In,Ga,Mn)As and (Ga,Mn)N are of major interest. This thesis investigates different aspects of these, using the synchrotron radiation techniques of x-ray magnetic circular dichroism (XMCD) and x-ray magnetic linear dichroism (XMLD), supported by superconducting quantum interference device (SQUID) magnetometry and magnetotransport measurements.

A large anisotropic XMLD signal is observed for the Mn L-edge in (Ga,Mn)As. In unannealed (Ga,Mn)As, an apparently reduced Mn magnetic moment is commonly observed. It is thought to be related to compensation of both carriers and magnetic moment, caused by interstitial Mn. This issue is investigated using combined data from XMCD, XMLD and SQUID magnetometry. The findings suggest that substitutional and interstitial Mn form 'non-magnetic' pairs which do not have a preferred spin orientation.

(Ga,Mn)N is studied by x-ray absorption and field-dependent XMCD at the Mn L-edge. Two distinct Mn configurations are identified: Mn^{2+} is prevalent towards the surface with nearly paramagnetic behaviour, while a weakly ferromagnetic Mn^{2+}/Mn^{3+} mixed valence exists within the bulk. The weak ferromagnetism, often observed in (Ga,Mn)N, is attributed to coupling between the impurities by the double exchange mechanism.

Finally, XMCD is used to measure the orbital polarization of As $4p$ states of (III,Mn)As materials. These states correspond to those of the holes involved in the itinerant exchange interaction in ferromagnetic semiconductors. The coupling between the localized d states of the magnetic impurities and the valence band p states of the host is demonstrated by an anisotropy in the orbital moment of these states. This is experimental confirmation of the origin of the magnetocrystalline anisotropy in dilute magnetic semiconductors.

Acknowledgements

Thanks to my supervisor Kevin Edmonds for the invaluable help and guidance he provided with my work and showing patience with my endless questions, and to Nicola Farley, for her friendly advice which made difficult experiments go much more smoothly. I also really appreciated the help of: Andrew Rushforth, Gerrit van der Laan, Elke Arenholz, Bryan Gallagher, Kaiyou Wang and Lixia Zhao. Tom Foxon, Sergei Novikov and Richard Campion gave me useful advice about the samples.

Thanks to EPSRC and CCLRC Daresbury for funding my PhD.

I am grateful to (in alphabetical order): Andrew Henning, Arianna Casiraghi, Chris King, Devin Giddings, Jacqueline Hall, Pete Wadley, Robin Marshall and Vicki Grant, whose friendship I have valued, and have all given me help and inspiration in different ways, which made a huge difference.

I would like to thank my Mum, Dad, Lucy, and Granny and Grandad Napierski for their unconditional love, patience and support. Finally thanks to Aspa for believing in me, having the patience to listen to me, being wonderfully supportive and making me so happy.

Contents

Chapter 1

Introduction and Background

1.1 Motivation for research in Spintronics

With the maturation of the information age, the information processing demands of modern life are increasing rapidly. The relentless drive for greater information storage capacity in physically smaller devices has pushed the size of components to scales where quantum mechanical effects become important. To aid such an increase in information density, both the electron spin and charge are exploited in the field of spin transport electronics; hence the portmanteau *spintronics*. The 2007 Nobel Prize for Physics was awarded for the discovery of giant magnetoresistance (GMR) [1, 2], which greatly enhanced the sensitivity of computer hard drive read-heads using devices called 'spin-valves', allowing for much greater areal density of information to be read from the disk. The capabilities of solid-state memory could soon surpass those of hard disks. By storing the state of the electron spin, the promise of magnetoresistive random access memory (MRAM) is to give fast, low power-consumption, non-volatile memory*, using tunnelling magnetoresistance (TMR) in metal/insulator structures.

The advantage of *semiconductor spintronics* is that devices based on metal spintronics could be incorporated into existing semiconductor heterostructure systems, and would permit new possibilities to unite magnetic storage with the processing capabilities of semicon-

*An existing and popular form of non-volatile solid state memory is *flash memory*. In its most widely-used form it is not random access, and retains information by charge stored on transistors, rather than by magnetic means.

ductors. A key criterion for such a material is that it behaves as a standard semiconductor, so that it has the flexibility afforded by doping or gating. It must be ferromagnetic above room temperature if it is to function properly in computer components. The material must also be able to carry a highly-polarized spin current with a long coherent lifetime, so that information is not lost at device interfaces. A candidate class of materials is the dilute magnetic semiconductors (DMS), in which magnetic moments are incorporated into a semiconductor lattice (see section 1.5).

The remainder of this chapter will begin with some background theory on magnetism, moving on to the phenomenon of spin-orbit coupling and sources of magnetic anisotropy, which are important in later experimental chapters (e.g. Chapter 5). The focus then shifts to an introduction to DMS, with descriptions of two popular examples: (Ga,Mn)As and (Ga,Mn)N. Finally, the Hall effect is introduced, to shed light on the magnetotransport measurements discussed in Chapter 5.

1.2 Types of magnetism

1.2.1 Paramagnetism

Elements which have unfilled outer shells possess a permanent magnetic dipole moment — for example materials containing the $3d$ transition metals or $4f$ rare earths. At sufficiently high temperatures, the dipole moments are randomly orientated, with zero net magnetization. The application of an external magnetic field **H** causes some moments to begin to align parallel to the field direction. It can be assumed that there is no interaction between magnetic moments; they only respond to the effect of the external magnetic field. The magnetization induced by an applied magnetic field is given by a material's susceptibility, χ, which is positive for paramagnets.

At low magnetic fields, the magnetic susceptibility *chi* is inversely proportional to the temperature, T, as described by the Curie Law:

$$\chi = \frac{C}{T} \tag{1.1}$$

where the Curie constant is given by

$$C = \frac{N\mu_0{\mu_B}^2}{3k_B}$$

where μ_B is the Bohr magneton and N is the number of magnetic moments in the material. The susceptibility also relates the sample magnetization to the applied magnetic field:

$$\chi = \frac{\mu_0 M}{B} \tag{1.2}$$

Semiclassical treatment ignores the quantization of the moments' direction, effectively assuming that the total angular momentum quantum number $J = \infty$. For a quantum mechanical system, the directions which the spins can point in are constrained by quantization.

At larger magnetic fields, the dependence of the magnetization upon both temperature and applied magnetic field can be described by a Brillouin function:

$$\frac{M}{M_S} = B_J = \frac{2J+1}{2J}\coth\left(\frac{2J+1}{2J}y\right) - \frac{1}{2J}\coth\left(\frac{y}{2J}\right) \tag{1.3}$$

where

$$y = \frac{g_J\mu_B JB}{k_B T} \tag{1.4}$$

is essentially a dimensionless measure of the applied magnetic field. Thus, the spins are aligned by increasing the magnetic field, but disordered by increasing the temperature.

1.2.2 Ferromagnetism

Ferromagnets have a finite spontaneous magnetization in the absence of an externally applied field, due to the alignment of some of the magnetic dipole moments to a particular direction. In this case, the interaction between the magnetic moments can no longer be ignored. The parallel alignment is communicated by an *exchange* interaction. The exchange interaction can be 'direct', due to the overlap of the wavefunctions of magnetic electrons on neighbouring atoms; or 'indirect', for example due to the interactions between

localized moments and conduction electrons in a metal.

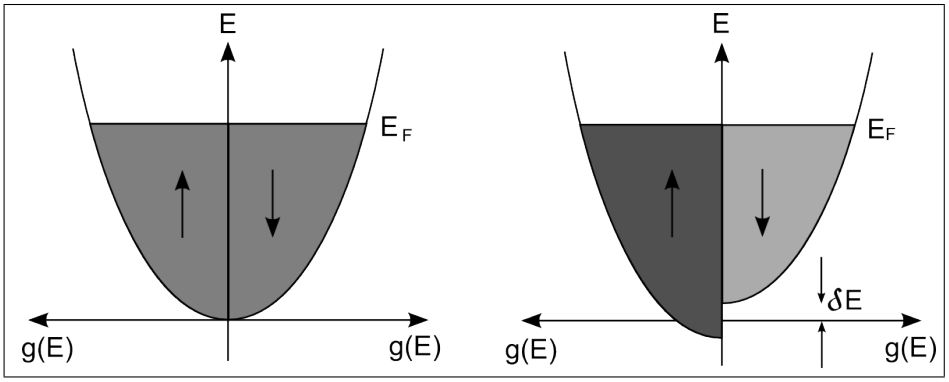

Figure 1.1: Schematic representation of the density of states at $T = 0$ in a normal metal (left) and in a ferromagnetic metal (right). $g(E)\delta E$ electrons have moved from spin-down to spin-up states, and the band energies are shifted to equalize the Fermi energy of both bands.

In a magnetized material, the spins can be thought of as interacting with an average exchange field $B_{mf} = \lambda M$ produced by all their neighbours (λ is a constant which indicates the strength of the molecular field for a given magnetization; $\lambda > 0$ for ferromagnets). In magnetic metals, magnetization is due to spontaneously spin-split energy bands. The energy splitting in the density of states (DOS) is depicted in figure 1.1. If each electron has a magnetic moment of 1 μ_B, the magnetization is given by the number densities of up- and down-spins: $M = \mu_B(n_\uparrow - n_\downarrow) = \mu_B\ g(E_F)\delta E$, where $g(E_F)$ is the density of states at the Fermi level.

There is a kinetic energy cost in moving some electrons from the spin-down band into the spin-up band:

$$\Delta E_{K.E.} = \frac{1}{2} g(E_F)(\delta E)^2 \tag{1.5}$$

The small spin population imbalance sets up a molecular field; this acts to stabilize the spontaneously split energy bands by providing a potential energy saving for aligning the spins to the molecular field.

$$\Delta E_{P.E.} = -\frac{1}{2}\mu_0 \lambda M^2 = -\frac{1}{2} U\ (g(E_F)\delta E)^2 \tag{1.6}$$

U is a measure of Coulomb energy, i.e. the high-spin-state.

$$\Delta E_{K.E.} + \Delta E_{P.E} = -\frac{1}{2} g(E_F)(\delta E)^2 (1 - U\ g(E_F)) \tag{1.7}$$

The interplay between these two energies determines whether the metal magnetizes spontaneously; this occurs if the Stoner criterion ($U\ g(E_F) \geq 1$) is satisfied. This requires that the Coulomb energy is large enough, and the density of states at the Fermi energy is large (*i.e.* the system is metallic).

The exchange energy of the whole solid can be approximated as the sum over all the individual exchange interactions. The Heisenberg Hamiltonian below is the starting point for many calculations to determine the properties of magnetically ordered materials:

$$\hat{\mathcal{H}} = -\sum_i \sum_{i \neq j} \mathsf{J} \mathbf{S}_i \cdot \mathbf{S}_j \tag{1.8}$$

The effect of the exchange interaction between all the individual magnetic atoms in a ferromagnet can be approximated as a classical Weiss molecular field/mean field, where the spin operators in the Heisenberg Hamiltonian are replaced by their average values, so fluctuations are ignored. The Weiss mean field treats the system as a paramagnet in a magnetic field of $B + \lambda M$, so at low temperature the moments are aligned by the molecular field, even for $B = 0$. Above the temperature at which spontaneous magnetization occurs, the susceptibility for small B is given by:

$$\chi = \frac{\mu_0 M}{B} = \frac{C}{T - T_{CW}} \tag{1.9}$$

where the Curie-Weiss temperature $T_{CW} = \lambda C \simeq T_C$, and λ is a dimensionless constant proportional to the summed exchange energies of one spin with all the other spins in the solid. At $T = T_C$, the susceptibility becomes infinite, signifying a phase transition between paramagnetism and ferromagnetism.

1.2.3 Antiferromagnetism

If the exchange energy between two nearest neighbouring atoms is negative, the preferred spin orientation is antiparallel. This means that the spins are aligned to a common axis,

but the orientation alternates within the structure so that there is no net magnetization. This lattice of magnetic atoms with opposing spin directions may be thought of as two sublattices, each with a spontaneous magnetization but of antiparallel orientation. The Néel approach of antiferromagnetism imagines that each sublattice experiences a Weiss molecular field caused by the other.

$$\chi = \frac{M_A + M_B}{H} = \frac{C}{T + T_N} \tag{1.10}$$

where $T_N = \lambda C/2$ is the Néel temperature, above which the antiferromagnetic order is broken.

1.2.4 Diamagnetism

Diamagnetism is the property of a material which causes it to create a magnetic field in opposition to an externally applied magnetic field, causing a repulsive effect. All materials exhibit some degree of diamagnetism, but only those which do not exhibit other forms of magnetism are termed 'diamagnetic materials'. It occurs when a material is placed in a magnetic field, inducing electric currents which oppose the magnetic field that induced it. The diamagnetic response increases with the externally applied field, but is independent of temperature; usually it is dwarfed by ferro- or paramagnetic behaviour, if present. It is important to take a diamagnetic signal into consideration in magnetometry experiments: temperature-dependent measurements of Mn-doped GaAs in non-zero magnetic field show a constant negative offset caused by the diamagnetic GaAs; field-dependent measurements have a negative gradient superimposed on the field-dependence of the Mn.

1.3 Spin-orbit coupling

An electron orbiting its nucleus has orbital angular momentum, $\mathbf{l}$. In addition, the electron has an intrinsic magnetic momentum, $\mathbf{s}$, called its 'spin' because of the analogy to a classically rotating body about an axis. For a light atom ($Z \leq 30$) with a partially occupied outer electron shell, the spin and orbital angular momenta are summed separately over all the electrons to give $\mathbf{L}$ and $\mathbf{S}$, the total spin and orbital momenta for the atom. These

angular momenta contribute to the magnetic moment: $\mu = -\mu_B(\mathbf{L} + 2\mathbf{S})$.

The spin-orbit interaction occurs when we consider the picture of an electron orbiting its nucleus. From the electron's reference frame, there is a positive charge orbiting it. This current generates a magnetic field, which interacts with the electron spin. When $\mathbf{L}$ and $\mathbf{S}$ are coupled, they are no longer individually conserved; however the total angular momentum $\mathbf{J} = \mathbf{L} + \mathbf{S}$ is conserved. According to Hund's Rules, the ground state of the ion minimizes Coulomb repulsion energy by first maximizing S and then by maximizing L. Finally, the spin-orbit energy is minimized, using $J = |L - S|$ if the outer shell is less than half full and $J = |L + S|$ if it is more than half full. In the presence of a magnetic field (either externally applied or as an internal molecular field), the electron states split into $2J + 1$ energy levels (or m_J states). Although the orbital angular momentum is usually only a small contribution to the magnetic moment, it is sensitive to the crystal environment and can hold sway over the spin moment orientation if the spin-orbit interaction is strong.

1.4 Magnetic anisotropy

Magnetic anisotropy is a preference of a material to magnetize in a certain direction. The direction in which the magnetization saturates with the least applied field is known as the 'easy' magnetic axis. There are different sources of magnetic anisotropy, whose interplay can lead to some complex anisotropic behaviour. Factors which may affect the strength of the magnetization, such as carrier concentration [3] and temperature [4], can have a concomitant effect on the magnetic anisotropy.

1.4.1 Shape anisotropy

This type of magnetic anisotropy occurs for any magnetic domains which are non-spherical in shape. For the example of a magnetic material consisting of a single domain, the magnetization of the sample results in magnetic poles forming at its surface, which create a demagnetizing field inside the material to oppose the internal magnetization. The demagnetizing field for a spherically symmetric domain would be isotropic. For an oblong domain, the demagnetizing field would be stronger when the magnetization is along its short axis

than its long axis. The smallest demagnetizing field corresponds to the lowest energy configuration: in the example of thin films, a shape anisotropy term leads to an energetic saving for keeping the magnetization in the plane of the film. However, the contribution of shape anisotropy is generally small for DMS, due to the low moment density.

1.4.2 Magnetocrystalline anisotropy

The coupling of magnetization to a crystalline lattice is known as magnetocrystalline anisotropy (MCA). This plays a central role in technological applications of ferromagnetism, from permanent magnetic materials to ultrathin films, and is a vital attribute of many DMS. The origin of MCA lies with the spin-orbit interaction, leading to a preference for the magnetization to align to certain crystalline directions. The energy required to rotate a material's magnetization from its easy to hard magnetic axis is known as the magnetocrystalline anisotropy energy (MAE), and is shown to be directly related to the anisotropic part of the spin-orbit interaction [5]. The crystal symmetry therefore strongly affects the direction of the easy and hard magnetization axes.

1.5 Dilute Magnetic Semiconductors

The DMS consist of a single-crystal (usually) semiconductor doped with a small amount of transition metal (TM) atoms. This is usually achieved during growth of the crystal, but it is also possible to implant the magnetic impurities afterward. The predictions of the Zener mean-field model of carrier-mediated ferromagnetism [6] have been the primary inspiration for research into potential DMS compounds. This model predicts that (Ga,Mn)N should have the highest Curie temperature T_C ($\approx$400 K) of the III-V DMS; of the II-VI compounds, (Zn,Mn)O is also predicted to be ferromagnetic above room temperature. Since then, ZnO- and GaN-based DMS have been keenly pursued, as the host semiconductors are already used for many existing semiconductor applications, seemingly promising much for both applications and underlying physics of spintronics. Despite a great deal of interest in TM-doped ZnO, generated by the Zener mean-field predictions for highly p-type material [6], (Zn,Mn)O and (Zn,Co)O films have been shown to be purely paramagnetic at all

temperatures [7, 8]. (Ga,Mn)N has yielded similar disappointments; this emphasizes that the mean-field model is inapplicable to these systems.

Much of the early research into DMS pursued the II-VI compounds, such as (Zn,Mn)Te and (Cd,Mn)Te. Although preparing isovalent TM-doped II-VI compounds is relatively easy, forcing them to be p-type or n-type is difficult, making them less attractive for applications. More success has been found in the III-V DMS with narrow band-gaps, where the magnetic dopant is a shallow acceptor. The first DMS to exhibit robust, carrier-mediated ferromagnetism was (In,Mn)As [9], followed later by (Ga,Mn)As [10]. (In,Mn)As is a very narrow band-gap material, and its Curie temperature is fairly limited ($\sim$ 90 K [11]), while the T_C of (Ga,Mn)As has risen to around 185 K [12]. Extensive research into the latter has exposed rich magnetic anisotropic and magnetotransport properties. Although it seems unlikely that bulk (Ga,Mn)As material will achieve room temperature ferromagnetism, investigations at low temperatures are important for understanding the material's behaviour in the absence of thermal influences.

For extensive reviews of theoretical approaches for DMS, Refs. [13, 14] are recommended.

1.5.1 MBE Growth of DMS

The technique of molecular beam epitaxy (MBE) is the growth of single-crystal structures by the deposition of evaporated atoms or molecules onto the face of a crystal substrate. Elemental sources in effusion cells are heated until they evaporate in ultra-high vacuum (UHV) conditions. The molecular beams produced are shuttered to allow precise control over the layer thickness. The molecules then proceed otherwise uninterrupted to the substrate, which rotates about the growth axis to improve the uniformity of deposition. Alloyed compounds are routinely grown by the simultaneous use of multiple sources; their composition is controlled by balancing the relative fluxes of each element, determined by the cell temperatures. The substrate itself is also heated; choice of the correct growth temperature is important because it determines how the adatom is incorporated, and the resulting structure and quality of the sample. During growth, reflection high energy electron diffraction (RHEED) is used *in-situ* to measure the atomic spacing

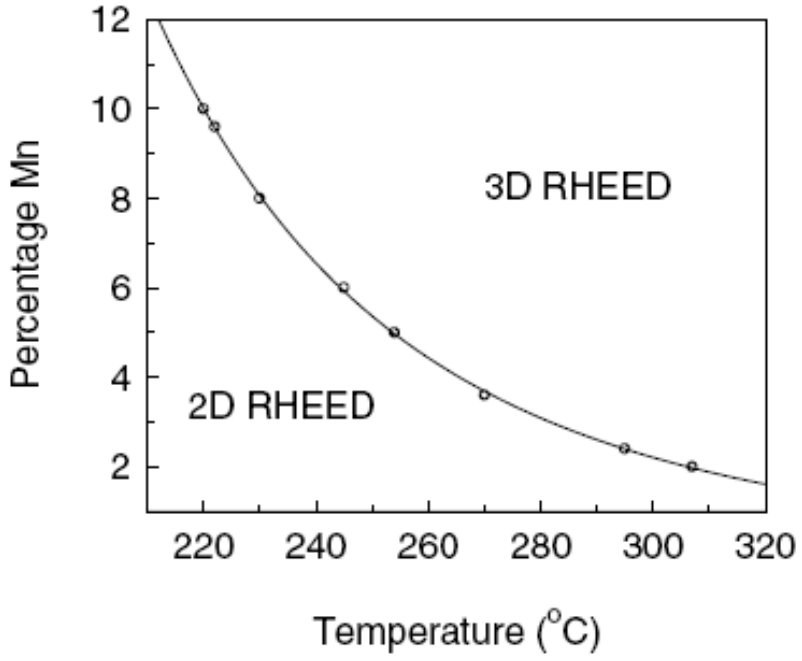

Figure 1.2: Surface phase diagram for the growth of (Ga,Mn)As. Image taken from Campion *et al.* [15].

and crystal structure of the surface layer, which determine the angles at which diffracted electrons constructively interfere. The growth rate is monitored by observing the intensity oscillations in the RHEED pattern caused by the formation of successive monolayers. For the growth of thin films, it is important that the material's lattice parameter is close to that of the substrate, otherwise structural lattice defects can form (such as dislocations or vacancies) in an attempt to relax the lattice and reduce the strain energy. However, some degree of epitaxial strain can be advantageous, because of its influence on the anisotropies in the magnetic and magnetotransport properties.

The low thermodynamic solubility limits of TM ions in III-V semiconductors can be overcome by non-equilibrium MBE growth. This was demonstrated first with the growth of (In,Mn)As [16] and later with (Ga,Mn)As [10], approaching the Mn concentrations required for itinerant ferromagnetism in a DMS. However, at such dopant concentrations ($\geq 1\%$), segregation of the Mn can occur where it accumulates at the surface and forms complexes with the As atoms [17]. This occurrence can be observed in the *in-situ* RHEED pattern as a transition from 2D to 3D growth conditions. From figure 1.2 it can be seen that

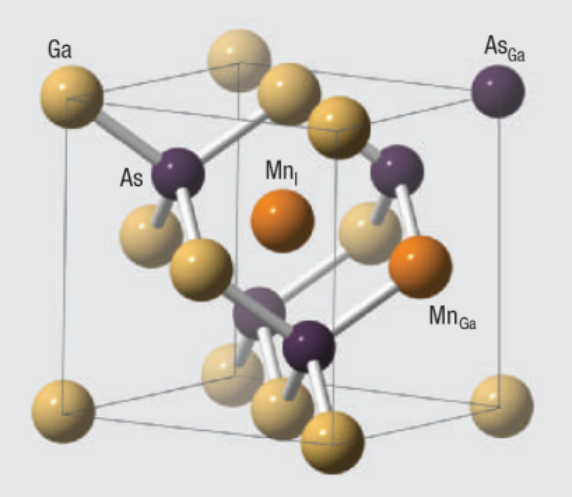

Figure 1.3: The zinc-blende structure of (Ga,Mn)As. Substitutional Mn (Mn_{Ga}), interstitial Mn (Mn_I) and As antisites (As_{Ga}) are shown. Image taken from MacDonald, et al. [18]

low growth temperatures are required to incorporate large amounts of Mn. 2D growth is preferable, allowing uniform film growth and reducing structural defects; the optimal electrical and magnetic properties are achieved for the films grown close to the 2D/3D boundary.

1.5.2 (Ga,Mn)As

Structure

The host crystal GaAs has a zinc-blende crystal structure, which is two interpenetrating face-centred cubic lattices displaced by $a_0/4$ along each [1 0 0] crystalline direction, depicted in figure 1.3. The lattice constant is $a_0 = 5.653$ Å at $T = 300$ K. The growth plane is most commonly (0 0 1). The natural cleavage planes are the {1 1 0} planes. Doping with Mn in low concentrations ideally results in the Mn locating at Ga sites (Mn_{Ga}). The Mn^{2+} ion is significantly larger than Ga^{3+}, so the lattice parameter increases linearly with Mn_{Ga} concentration [19], in agreement with Vegard's law. The commonest impurity defects that occur in (Ga,Mn)As are As antisites (where As substitutes for a Ga atom) and Mn located in interstitial lattice sites; these are both depicted in figure 1.3. Both of these drastically increase the lattice parameter, again in direct proportion to their concentration [20].

Electronic properties

The electronic shell structure of a Mn atom is [Ar] $4s^2$ $3d^5$. For Ga, its complete $3d$ shell becomes lower in energy than the $4s$ shell: [Ar] $3d^{10}$ $4s^2$ $4p^1$. When bonded in GaAs, the Ga $4p$ and $4s$ electrons form the bonds with neighbouring As ions. The half-filled d shell of the substitutional Mn is relatively stable, so it only donates its $4s$ electrons to the bond. The missing bonding electron corresponds to each Mn_{Ga} donating a hole to the semiconductor lattice. The highest hole concentration of as-grown (Ga,Mn)As is $p \sim 5 \times 10^{20}$ cm^{-3}, while in annealed material it can reach as high as $p \sim 10^{21}$ cm^{-3} [21].

GaAs is a direct band-gap semiconductor, with an energy gap of 1.424 eV at 300 K. Substitutional Mn^{2+} in GaAs is a shallow acceptor; in the dilute limit it forms a narrow impurity band $\sim$ 110 meV above the GaAs valence band, with the Fermi level pinned to it. With increasing Mn concentration, the impurity band broadens and moves closer to the valence band. Above $\sim$ 2% substitutional Mn, the hole concentration becomes great enough for the material to be metallic. Above the metal-insulator transition, the Mn impurity band merges with the valence band. This allows the delocalization of the Mn d states, permitting the p-d itinerant exchange interaction. A wealth of experimental data and simulations support this picture [22].

The GaAs valence band is spin-orbit split into $J = 3/2$ and $J = 1/2$ bands, offset by $\Delta_{SO} = 0.34$ eV [6]. An additional splitting of the $J = 3/2$ band occurs because of the different effective masses of the $m_J = \pm 1/2$ and $m_J = \pm 3/2$ states (termed 'light holes' (LH) and 'heavy holes' (HH) respectively), which are degenerate at $k = 0$ but have different energy dispersion profiles. Their degeneracy at $k = 0$ is lifted in the presence of epitaxial strain.

Ferromagnetism and Curie temperature

The merging of the Mn impurity band with the GaAs valence band permits the hybridization of the Mn $3d$ and GaAs $4p$ states. The itinerant holes are polarized by antiferromagnetic coupling to the local Mn $J = 5/2$ magnetic moments, thereby mediating ferromagnetic order between the Mn_{Ga}.

The principal influences determining the temperature at which the onset of ferromagnetism occurs are the concentrations of Mn_{Ga} (x) and of holes (p). The simplest mean-field Zener model [6] predicts that the Curie temperature scales as $T_C \propto x \cdot p^{1/3}$; correspondingly, ferromagnetism at room-temperature ($\sim$ 300 K) should be possible for (Ga,Mn)As with 10% substitutional Mn, yet this goal remains elusive. The theory is in qualitative agreement with experiment, but overestimates T_C for large x and underestimates it at low x. More advanced microscopic models have since been developed [23]: the current view is that T_C is roughly linear with x, with a small dependence on p for metallic material.

Suggestions that the Curie temperature of (Ga,Mn)As was limited to 110 K [24, 25] were dispelled with the use of low-temperature ($\sim$ 175°C) resistance-monitored annealing [26, 27]. Recent refinements in the growth and annealing process have yielded incremental improvements to $T_C \approx 185$ K [12], but there is little hope of further significant improvement. The experimental results diverge from Dietl's predictions of room-temperature ferromagnetism in (Ga,Mn)As with 10% substitutional Mn, possibly because this model neglects disorder and direct antiferromagnetic Mn-Mn interactions.

Magnetocrystalline anisotropy

The DMS (Ga,Mn)As has a particularly interesting MCA behaviour. It is absent in the dilute dopant limit, but a strong uniaxial MCA emerges with higher Mn concentration, which is strongly dependent on strain [28]. Epitaxial strain can be induced in thin ferromagnetic films if their lattice parameter is mismatched to that of the substrate. The distortion of the chemical bonds of the crystal lattice augments the MCA. A thin film of (Ga,Mn)As grown on a GaAs substrate is compressively strained, usually causing an in-plane easy axis; using (In,Ga)As as the substrate results in tensile strain, orientating the easy axis perpendicular to the (0 0 1) growth plane. By tuning the stoichiometry of the constituent elements in the thin film layer, the lattice parameter can be adjusted to influence the easy axis direction. There is also competition between in-plane cubic anisotropy (along [1 0 0] and [0 1 0]) and uniaxial anisotropy along the $[1\,\bar{1}\,0]$ axis. This interplay is found to be dependent upon temperature [4, 29].

Self-Compensation

The As_{Ga} defect replaces a group V ion with a III ion. The Mn_I sits in an interstitial lattice site and as an unbonded atom, so keeps its $4s$ electrons. These defects (known as *double-donors*) each donate their two surplus electrons to the lattice; therefore each defect compensates the holes provided by two substitutional Mn ions, making them very undesirable.

Self-compensating impurities like As_{Ga} and Mn_I occur when trying to incorporate Mn in concentrations above its solubility limit in GaAs; this is because the associated high carrier concentration is energetically unfavourable. The double-donor defects form to keep the hole concentration low, thereby increasing the stability of the system. Using low growth temperatures increases the probability of Mn_I [30] and As_{Ga} [31, 32] forming. While Mn_I may be removed post-growth by low-temperature annealing [26, 27], As_{Ga} are not so easily eliminated [33]. The probability of its formation may be substantially reduced by growing with As_2 dimers [31].

Besides limiting the hole concentration and Curie temperature, interstitial Mn are found to directly compensate the magnetic moment of substitutional Mn, by a direct antiferromagnetic coupling [34]. This lowers the average magnetic moment per Mn of the material; on annealing the magnetic moment nearly recovers its full atomic value [35]. The causes of magnetization deficit are reviewed in detail in Chapter 3.

1.5.3 (Ga,Mn)N

Structure

GaN has found particular use in recent years for bright LEDs. It is a direct, wide band-gap semiconductor and is a very hard material. GaN may exist in a thermodynamically stable wurtzite phase (figure 1.4) or a metastable zinc-blende phase. Both are found to be n-type, attributed to auto-doping due to N vacancies [36]. By using zinc-blende (cubic) substrates, (Ga,Mn)N may be epitaxially grown in a cubic structure instead of the favoured wurtzite. Zinc-blende (Ga,Mn)N is found to be naturally p-type by Hall-effect measurements [37], with no need for co-doping. Zener mean-field theory predicts that cubic GaN should have

a 6% higher T_C than for wurtzite [6].

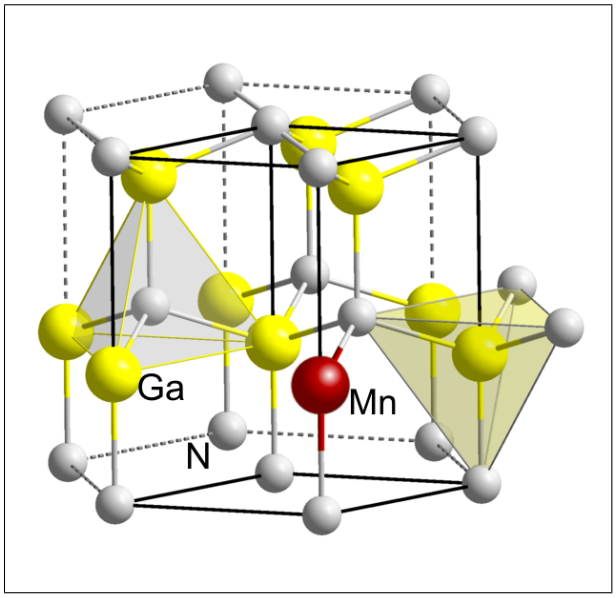

Figure 1.4: The wurtzite structure of GaN doped with Mn. The unit cell is drawn in thick black lines. Tetrahedra are highlighted, showing a Ga atom surrounded by its four N nearest neighbours, and the reverse for a N atom. Image adapted from `commons.wikimedia.org/wiki/Category:Wurtzite`.

Electronic properties

The band-gap of GaN is much larger than GaAs; ∼3.4 eV for the wurtzite phase. The hole density seems to be limited to about $p \sim 10^{18}$ cm^{-3}, less than the optimal hole density required by the Zener model for ferromagnetic order, and much less than typical hole densities of (Ga,Mn)As (typically $p \sim 10^{20}$ cm^{-3}). The majority of research has been done on wurtzite (Ga,Mn)N, engendering attempts to make it p-type and attain a hole density comparable with that of the best (Ga,Mn)As films, usually by co-doping with acceptors such as Mg, Be or C. Yet there are many studies reporting ferromagnetism in n-type wurtzite (Ga,Mn)N, often in excess of room temperature [38–40]. The weak interaction between the conduction electrons and the magnetic ions is thought to make ferromagnetism in n-type DMS unfavourable. Consequently, the application of the Zener model of hole-mediated ferromagnetism [6] is likely to be insufficient to describe any observed ferromagnetism.

Ferromagnetism, T_C

The meagre hole densities achievable in (Ga,Mn)N mean that the Zener mean-field model is inappropriate to describe any observed ferromagnetism. Moreover, the positioning of the impurity band deep within the band-gap means that the carrier states remain very localized around the Mn centres, unable to hybridize with the valence band p-states and resulting in a strong but very short-range exchange interaction. In this case, the ferromagnetism is mediated by holes in the impurity band, and p-type conductivity is permitted by the double-exchange mechanism, i.e. d-electron hopping between the coexisting Mn^{2+} and Mn^{3+} states. Calculations accounting for the percolation effect of the short-range exchange interaction predict much lower values for T_C, down to 55 K at $x = 0.05$ [41] or 30 K at $x = 0.06$ [42], with high T_C being expected only in the presence of valence-band holes [43].

Experimentally, there had been some controversy on the T_C achievable in (Ga,Mn)N. Reported Curie temperatures range from 10 K or less [44,45] to well above room-temperature [38,39,46], the latter perhaps encouraged by the overestimates of the mean-field model and apparent support from early *ab initio* results [47]. Some experimental studies are based on the strength of magnetometry data alone. To validate such claims, the inclusion of XMCD data is essential. Often this ferromagnetic signal can be attributed to a minority phase or nanoclusters within the material [48]. This view is supported by calculations which show that Mn_xN_y clusters and various configurations of dimerized Mn can lead to substantial enhancements of T_C [49–51]. The formation of such clusters may be important in a wide range of similar DMS systems with very low carrier concentration and apparently high-temperature ferromagnetism [52].

1.6 The Hall Effect

The Hall effect encompasses a number of similar phenomena, whereupon an electrostatic potential arises perpendicular to the direction of a current flowing through a conductor. In the scope of this study, only the ordinary Hall effect (OHE) and anomalous Hall effect (AHE) are considered. The OHE occurs when the symmetry is broken by application of a magnetic field **B** perpendicular to the current direction; the resulting Lorentz force acting

on the electrons orthogonal to **B** and **I** causes their path to deviate, so that there is a gradient in carrier concentration from one side of the conductor to the other, hence a Hall voltage.

The AHE occurs when an electric current passes through a ferromagnet, and depends on the magnetization rather than the external field itself. The anomalous Hall voltage is set up by electrons being scattered in a direction perpendicular to the current and magnetization directions, because the symmetry of the scattering is broken by the spin-orbit interaction between charge carriers in the band states and crystal defects.

Since OHE and AHE are dependent upon the applied magnetic field and magnetization respectively, the Hall resistivity may be written like this:

$$\rho_H = \rho^{OHE} + \rho^{AHE} = R_O B_z + R_S M_z \tag{1.11}$$

where R_O and R_S are the ordinary and anomalous Hall coefficients. Although the anomalous component is greatest (*i.e.* saturated) at temperatures below T_C, it can be the dominant part of the Hall voltage several hundred degrees into the paramagnetic regime.

In magnetic and non-magnetic metals alike, $R_O = 1/n_e ed$ where d is the thickness of the conductor, n_e (or p) is the electron (or hole) concentration and e is the electron charge, with the obvious implication that the OHE is the opposite sign for n-type and p-type materials. The AHE is linked to carrier scattering, which increases with increasing temperature, as does the bulk resistivity ρ_{xx}. The Hall coefficient may be modelled as

$$R_S = \gamma_H \rho_{xx}^{\alpha}(T) \tag{1.12}$$

The parameter γ_H is nearly independent of temperature above T_C; the exponent α may vary continuously between 1 and 2, and relates to the nature of the electron scattering process responsible for the AHE.

Berger and Bergmann [53] give a historical overview of the AHE, and explore the scattering mechanisms in detail for ferromagnetic metals.

1.7 Layout of Thesis

This Thesis contains three experimental studies, in which detailed magnetic characteristics of different (III,Mn)V DMS are investigated, primarily by the use of sophisticated magnetic x-ray spectroscopy techniques. The research chapters are preceded by a survey of how synchrotrons produce radiation, and the experimental techniques which form the majority of this thesis. Chapter 3 begins with an experiment showing a strongly anisotropic XMLD signal in Mn with respect to a crystal field. Following on from this, an investigation is made into the well-observed magnetization deficit of (Ga,Mn)As, combining information from XMLD, XMCD and SQUID experiments. Chapter 4 is a study of features in the Mn L-edge x-ray absorption and XMCD spectra from (Ga,Mn)N samples. In Chapter 5, the observed anisotropy in the magnetization of (Ga,Mn)As observed is linked to an anisotropy of the orbital moment of valence band states, in support of the generally held view that the magnetocrystalline anisotropy comes from coupling of the localized Mn $3d$ spin moments to the the orbital moment of the valence band states. Finally, these investigations are summarized, and potential future studies are considered.

References

[1] M. N. Baibich, J. M. Broto, A. Fert, F. N. Van Dau, F. Petroff, P. Etienne, G. Creuzet, A. Friederich, and J. Chazelas, *Phys. Rev. Lett.* **61**, 2472 (1988).

[2] G. Binasch, P. Grünberg, F. Saurenbach, and W. Zinn, *Phys. Rev. B* **39**, 4828 (1989).

[3] T. Dietl, H. Ohno, and F. Matsukura, *Physical Review B* **63**, 195205 (2001).

[4] K. Y. Wang, M. Sawicki, K. W. Edmonds, R. P. Campion, S. Maat, C. T. Foxon, B. L. Gallagher, and T. Dietl, *Physical Review Letters* **95**, 217204 (2005).

[5] G. van der Laan, *Physical Review Letters* **82**, 640 (1999).

[6] T. Dietl, H. Ohno, F. Matsukura, J. Cibert, and D. Ferrand, *Science* **287**, 1019 (2000).

[7] N. R. S. Farley, K. W. Edmonds, A. A. Freeman, G. van der Laan, C. R. Staddon, D. H. Gregory, and B. L. Gallagher, *New Journal of Physics* **10**, 055012 (2008).

[8] T. C. Kaspar, T. Droubay, S. M. Heald, P. Nachimuthu, C. M. Wang, V. Shutthanandan, C. A. Johnson, D. R. Gamelin, and S. A. Chambers, *New Journal of Physics* **10**, 055010 (18pp) (2008).

[9] H. Ohno, H. Munekata, S. von Molnár, and L. L. Chang, New III-V diluted magnetic semiconductors (invited), volume 69, pp. 6103–6108, AIP, 1991.

[10] H. Ohno, A. Shen, F. Matsukura, A. Oiwa, A. Endo, S. Katsumoto, and Y. Iye, *Applied Physics Letters* **69**, 363 (1996).

[11] T. Schallenberg and H. Munekata, *Journal of Crystal Growth* **301-302**, 623 (2007), 14th International Conference on Molecular Beam Epitaxy - MBE XIV.

[12] M. Wang, R. P. Campion, A. W. Rushforth, K. W. Edmonds, C. T. Foxon, and B. L. Gallagher, *Applied Physics Letters* **93**, 132103 (2008).

[13] C. Liu, F. Yun, and H. Morkoç, *Journal of Materials Science: Materials in Electronics* **16**, 555 (2005).

[14] T. Jungwirth, J. Sinova, J. Masek, J. Kucera, and A. H. MacDonald, *Reviews of Modern Physics* **78**, 809 (2006).

[15] R. P. Campion, V. A. Grant, K. W. Edmonds, B. L. Gallagher, and C. T. Foxon, *Phys. Stat. Sol. (b)* **244**, 2944 (2007).

[16] H. Munekata, H. Ohno, S. von Molnar, A. Segmüller, L. L. Chang, and L. Esaki, *Phys. Rev. Lett.* **63**, 1849 (1989).

[17] D. DeSimone, C. E. C. Wood, and J. C. A. Evans, *Journal of Applied Physics* **53**, 4938 (1982).

[18] A. H. MacDonald, P. Schiffer, and N. Samarth, *Nature Materials* **4**, 195 (2005).

[19] L. X. Zhao, C. R. Staddon, K. Y. Wang, K. W. Edmonds, R. P. Campion, B. L. Gallagher, and C. T. Foxon, *Applied Physics Letters* **86**, 071902 (2005).

[20] J. Mašek, J. Kudrnovský, and F. Máca, *Phys. Rev. B* **67**, 153203 (2003).

[21] K. W. Edmonds, K. Y. Wang, R. P. Campion, A. C. Neumann, C. T. Foxon, B. L. Gallagher, and P. C. Main, *Applied Physics Letters* **81**, 3010 (2002).

[22] T. Jungwirth, J. Sinova, A. H. MacDonald, B. L. Gallagher, V. Novák, K. W. Edmonds, A. W. Rushforth, R. P. Campion, C. T. Foxon, L. Eaves, E. Olejník, J. Mašek, S.-R. E. Yang, J. Wunderlich, C. Gould, L. W. Molenkamp, T. Dietl, and H. Ohno, *Physical Review B* **76**, 125206 (2007).

[23] T. Jungwirth, K. Y. Wang, J. Mašek, K. W. Edmonds, J. König, J. Sinova, M. Polini, N. A. Goncharuk, A. H. MacDonald, M. Sawicki, A. W. Rushforth, R. P. Campion, L. X. Zhao, C. T. Foxon, and B. L. Gallagher, *Physical Review B* **72**, 165204 (2005).

[24] F. Matsukura, H. Ohno, A. Shen, and Y. Sugawara, *Physical Review B* **57**, R2037 (1998).

[25] K. M. Yu, W. Walukiewicz, T. Wojtowicz, W. L. Lim, X. Liu, U. Bindley, M. Dobrowolska, and J. K. Furdyna, *Physical Review B* **68**, 041308 (2003).

[26] K. W. Edmonds, K. Y. Wang, R. P. Campion, A. C. Neumann, N. R. S. Farley, B. L. Gallagher, and C. T. Foxon, *Applied Physics Letters* **81**, 4991 (2002).

[27] K. C. Ku, S. J. Potashnik, R. F. Wang, S. H. Chun, P. Schiffer, N. Samarth, M. J. Seong, A. Mascarenhas, E. Johnston-Halperin, R. C. Myers, A. C. Gossard, and D. D. Awschalom, *Applied Physics Letters* **82**, 2302 (2003).

[28] A. Shen, H. Ohno, F. Matsukura, Y. Sugawara, N. Akiba, T. Kuroiwa, A. Oiwa, A. Endo, S. Katsumoto, and Y. Iye, *Journal of Crystal Growth* **175-176**, 1069 (1997).

[29] M. Sawicki, F. Matsukura, A. Idziaszek, T. Dietl, G. M. Schott, C. Ruester, C. Gould, G. Karczewski, G. Schmidt, and L. W. Molenkamp, *Physical Review B* **70**, 245325 (2004).

[30] K. M. Yu, W. Walukiewicz, T. Wojtowicz, I. Kuryliszyn, X. Liu, Y. Sasaki, and J. K. Furdyna, *Physical Review B* **65**, 201303 (2002).

[31] R. P. Campion, K. W. Edmonds, L. X. Zhao, K. Y. Wang, C. T. Foxon, B. L. Gallagher, and C. R. Staddon, *Journal of Crystal Growth* **247**, 42 (2003).

[32] A. Wolos, M. Kaminska, M. Palczewska, A. Twardowski, X. Liu, T. Wojtowicz, and J. K. Furdyna, *Journal of Applied Physics* **96**, 530 (2004).

[33] M. Kaminska, Z. Liliental-Weber, E. R. Weber, T. George, J. B. Kortright, F. W. Smith, B.-Y. Tsaur, and A. R. Calawa, *Applied Physics Letters* **54**, 1881 (1989).

[34] J. Blinowski and P. Kacman, *Physical Review B* **67**, 121204 (2003).

[35] K. W. Edmonds, N. R. S. Farley, T. K. Johal, G. van der Laan, R. P. Campion, B. L. Gallagher, and C. T. Foxon, *Physical Review B* **71**, 064418 (2005).

[36] P. Boguslawski and J. Bernholc, *Physical Review B* **72**, 115208 (2005).

[37] K. W. Edmonds, S. V. Novikov, M. Sawicki, R. P. Campion, C. R. Staddon, A. D. Giddings, L. X. Zhao, K. Y. Wang, T. Dietl, C. T. Foxon, and B. L. Gallagher, *Applied Physics Letters* **86**, 152114 (2005).

[38] M. L. Reed, N. A. El-Masry, H. H. Stadelmaier, M. K. Ritums, M. J. Reed, C. A. Parker, J. C. Roberts, and S. M. Bedair, *Applied Physics Letters* **79**, 3473 (2001).

[39] S. Sonoda, S. Shimizu, T. Sasaki, Y. Yamamoto, and H. Hori, *Journal of Crystal Growth* **237-239**, 1358 (2002).

[40] M. C. Park, K. S. Huh, J. M. Myoung, J. M. Lee, J. Y. Chang, K. I. Lee, S. H. Han, and W. Y. Lee, *Solid State Communications* **124**, 11 (2002).

[41] L. Bergqvist, O. Eriksson, J. Kudrnovsky, V. Drchal, P. Korzhavyi, and I. Turek, *Physical Review Letters* **93**, 137202 (2004).

[42] K. Sato, W. Schweika, P. H. Dederichs, and H. Katayama-Yoshida, *Physical Review B* **70**, 201202 (2004).

[43] T. C. Schulthess, W. M. Temmerman, Z. Szotek, W. H. Butler, and G. M. Stocks, *Nature Materials* **4**, 838 (2005).

[44] M. E. Overberg, C. R. Abernathy, S. J. Pearton, N. A. Theodoropoulou, K. T. McCarthy, and A. F. Hebard, *Applied Physics Letters* **79**, 1312 (2001).

[45] E. Sarigiannidou, F. Wilhelm, E. Monroy, R. M. Galera, E. Bellet-Amalric, A. Rogalev, J. Goulon, J. Cibert, and H. Mariette, *Physical Review B* **74**, 041306 (2006).

[46] S. J. Pearton, C. R. Abernathy, M. E. Overberg, G. T. Thaler, D. P. Norton, N. Theodoropoulou, A. F. Hebard, Y. D. Park, F. Ren, J. Kim, and L. A. Boatner, *Journal of Applied Physics* **93**, 1 (2003).

[47] K. Sato and H. Katayama-Yoshida, *Semiconductor Science and Technology* **17**, 367 (2002).

[48] S. Dhar, O. Brandt, A. Trampert, L. Daweritz, K. J. Friedland, K. H. Ploog, J. Keller, B. Beschoten, and G. Guntherodt, *Applied Physics Letters* **82**, 2077 (2003).

[49] B. K. Rao and P. Jena, *Phys. Rev. Lett.* **89**, 185504 (2002).

[50] G. Bouzerar, T. Ziman, and J. Kudrnovsky, *Applied Physics Letters* **85**, 4941 (2004).

[51] T. Hynninen, H. Raebiger, J. von Boehm, and A. Ayuela, *Applied Physics Letters* **88**, 122501 (2006).

[52] S. Kuroda, N. Nishizawa, K. Takita, M. Mitome, Y. Bando, K. Osuch, and T. Dietl, *Nature Materials* **6**, 440 .

[53] L. Berger and G. Bergmann, *The Hall Effect and its Applications*, chapter 2: The Hall Effect of Ferromagnets.

Chapter 2

Synchrotron Radiation Techniques

2.1 Synchrotrons and their applications

Synchrotrons are essentially large x-ray sources, where a range of different techniques are employed. Many experiments are run in parallel at these facilities; although the experiments themselves are grounded in physics, the benefits of synchrotron light are exploited by the fields of chemistry, biology and medical research. The radiation produced by synchrotrons is characterized by a number of useful properties: high brilliance (typically 10^{18} photons per second in third generation sources), high collimation, high level of polarization, widely tunable in photon energy (< 1 eV to ~ 1 MeV), and pulsed light emission (< 1 ns). A host of techniques are available to the synchrotron user. Structural studies possible include powder diffraction, protein crystallography, and surface diffraction. Surface-science studies use photoemission, while high-energy x-rays can explore the bulk using fluorescence yield detection. Time-resolved techniques exploit the pulsed nature of synchrotron radiation to achieve high temporal-resolution, most useful for the study of fast chemical reactions. The x-ray absorption of materials by techniques such as x-ray absorption near-edge structure (XANES) and extended x-ray absorption fine structure (EXAFS) provides rich structural and chemical information; polarization-dependent dichroism studies can be made with XMLD and XMCD.

(a) Aerial view of the Diamond synchrotron, UK.

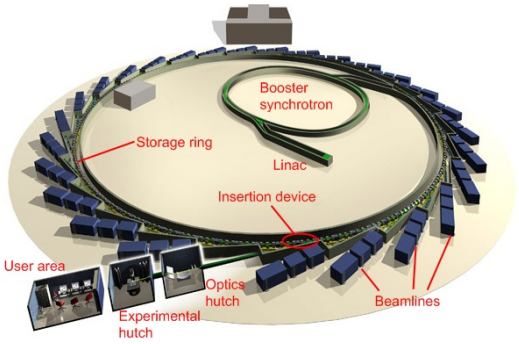

(b) Schematic layout of the Diamond synchrotron.

Figure 2.1: Images of synchrotrons, taken from the Diamond website: `www.diamond.ac.uk`.

2.2 Producing x-rays

Synchrotrons produce their radiation by bending the path of electrons moving at relativistic speeds, using magnetic fields. The path of a charge moving through a uniform magnetic field is deflected by the Lorentz force, acting perpendicular to its velocity. The acceleration of an electric charge causes it to emit electromagnetic waves (for example, the oscillation of the electrons in a radio antenna). The radiation emitted by electrons deflected by the Lorentz force is known as *cyclotron* radiation. If the charge is travelling at relativistic speeds, the emitted radiation is called *synchrotron* radiation.

Rather than being truly toroidal, a synchrotron storage ring is made of many straight sections, and the path of the electrons is bent at the corners using dipole *bending magnets*. These force the electrons to follow part of a circular trajectory as they pass through, then continue on a straight path until the next bending magnet. In third-generation light sources, periodic magnetic structures known as an insertion devices are used in addition to bending magnets. The insertion device is installed into a straight section of the storage ring, which forces the electrons to follow some form of sinusoidal trajectory. There are two types of these, known as *wigglers* and *undulators*. Figure 2.1 shows an aerial view and schematic layout of a typical third-generation synchrotron. Electrons are accelerated to almost the speed of light by a linear accelerator and booster ring, then sent to the main

storage ring. To compensate for the energy losses as the electron bunch emits energy, it receives an energy 'kick' as it passes through a radio frequency (RF) cavity, tuned to the frequency at which the charge circulates the storage ring.

The relativistic effects of Lorentz contraction and Doppler shift both help to shorten the wavelength of the emitted light, to yield x-rays. Another very important result of relativity affects the angular spread of the radiation. To help describe the Lorentz contraction, a parameter γ is defined so that

$$\gamma = \frac{1}{\sqrt{1 - \frac{u^2}{c^2}}} \tag{2.1}$$

where c is the speed of light and u is the relative speed of the two frames of reference.

For electrons approaching c, photons which are radiated perpendicular to the direction of motion in the electron frame have a very large forward component of velocity when viewed from the laboratory frame, due to the invariance of c. This causes the radiated energy to be bent forwards in the direction of electron motion in a very narrow cone, and its angular spread is determined by $1/\gamma$. Figure 2.2 depicts the cones of radiation produced by a bending magnet, wiggler and undulator, along with their typical spectral distribution profile. The bending magnet and wiggler produce a continuum of photon energies, while the undulator yields narrow peaks at harmonics of the fundamental frequency. This relativistic folding of the dipole radiation gives extremely collimated x-rays in the direction of propagation. The x-rays are (horizontally) linearly polarized in the bending plane, but above and below this plane there is a vertical component which results in elliptical polarization.

Wigglers consist of an array of dipole magnets (typically in a Halbach array) which deflect the electron path sinusoidally as they pass through it. The angular deflection is large enough so that there is only incoherent superposition of the overlapping radiation cones. At each deflection, a cone of radiation is emitted. The photon flux scales as $2N$, where N is the number of magnetic periods of the wiggler.

An undulator consists of a similar arrangement, but the angular deflection of the electrons is much smaller, so they follow a tighter trajectory. The closer overlapping of the radiation cones allows coherent interference, which produces sharp peaks in the photon

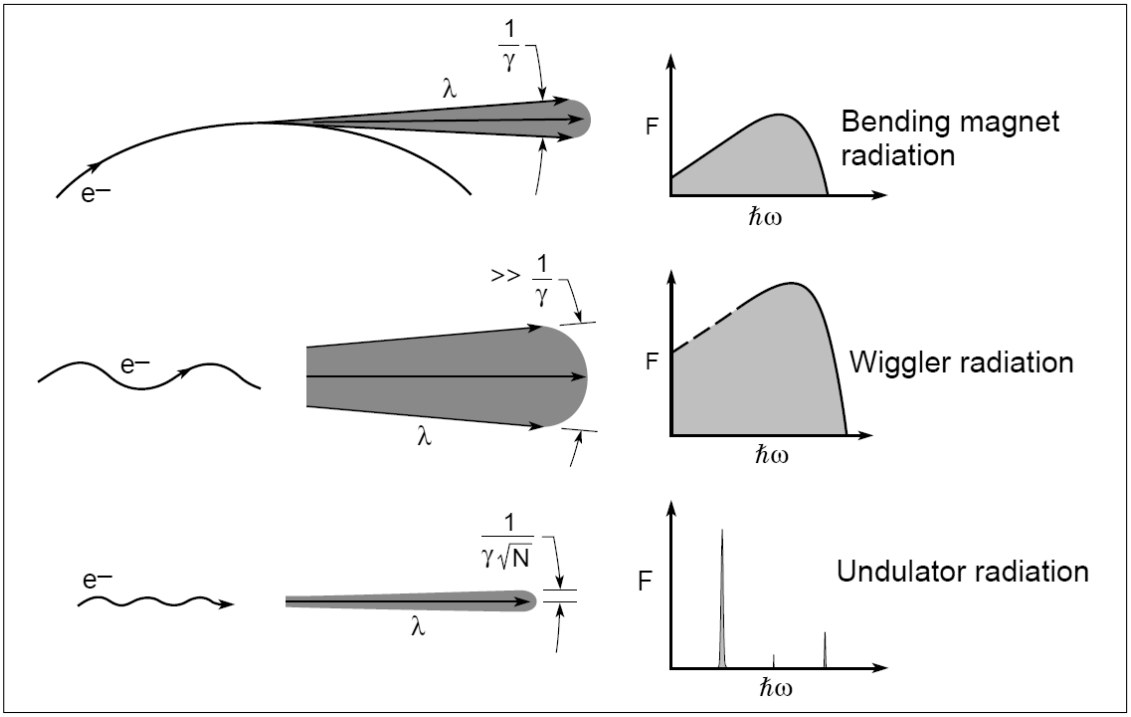

Figure 2.2: The spectra distribution profiles of radiation produced by bending magnet, wiggler and undulator devices. Taken from a lecture series by D. Attwood [1].

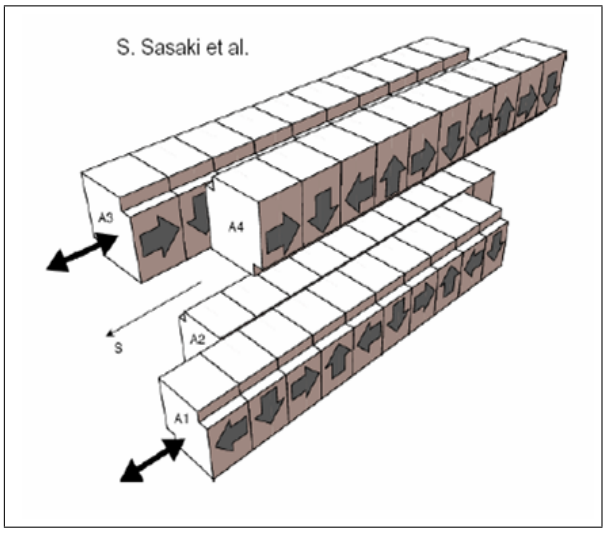

Figure 2.3: A variable polarization helical undulator, composed of four banks of permanent magnets in Halbach arrays (APPLE-II design [2, 3]). The orientations of the individual permanent magnets are indicated by the arrows; the photon polarization may be tuned by offsetting the horizontal alignment of diagonal pairs arrays (image taken from SRS 5U.1 VPU upgrade presentation: `http://www.srs.ac.uk/srs/stations/station5U.1.htm`).

flux at harmonics of the fundamental energy. In this case, intensity of the flux is proportional to N^2, allowing orders of magnitude greater brilliance than that available from bending magnets. The polarization and photon energy of maximal flux may be selected by adjusting the position and gaps between the magnets arrays.

Figure 2.3 shows a helical undulator which allows variation between linear and elliptical polarization. The angular spread of the radiation from an undulator source is determined not by $1/\gamma$, but by $1/\gamma\sqrt{N}$. The x-rays produced by undulators have a number of laser-like qualities: the Lorentz contraction serves to confine the emitted photons into a very narrow angle of emission, effectively collimating them, and the tight angular deflection of the electrons allows coherent superposition of the emitted x-rays.

The book by G. Margaritondo [4] provides an introduction to the workings of synchrotrons, useful to the newcomer and experienced user alike; the book by D. Attwood [5] and an accompanying lecture series [1] go into much greater depth.

2.3 Beamlines

The x-rays produced at bending magnets or insertion devices pass down beamlines, connected at a tangent from the storage ring, toward the experimental area. The beam is reflected, monochromated and focussed in the optics hutch, before being sent to the experimental chamber where it meets the sample. A typical beamline arrangement is shown in figure 2.4.

2.3.1 Beamline optics

To reflect the x-rays, plane crystals must be used in grazing incidence. The desired frequency is selected by a monochromator. There are two classes of monochromator, based on *diffraction gratings* or *crystals*. When two rays of a particular wavelength λ are reflected from different (but equivalent) points on a crystal or diffraction grating, they interfere constructively when their path difference is equal to a whole number of periods of the wave. This is the Bragg condition, $n\lambda = 2d\sin\theta$, where d is the spacing of the grating (or atoms, in a crystal monochromator).

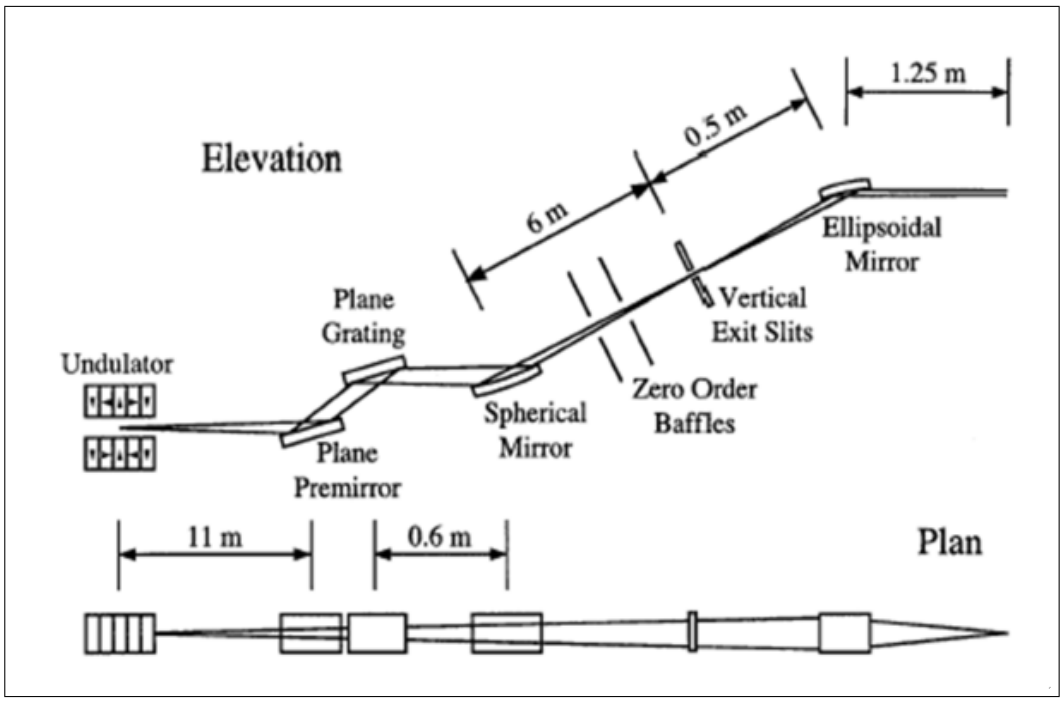

Figure 2.4: A typical soft x-ray beamline layout (image taken from SRS VPU upgrade presentation: `http://www.srs.ac.uk/srs/stations/station5U.1.htm`)

Diffraction grating monochromators are used for 'soft' x-rays ($\sim 500 - 2000$ eV). These consist of a periodic array of lines of equal spacing, as depicted in figure 2.5; the spacing of features on the grating is the important parameter. When two incoming rays are reflected from equivalent points on the grating, the condition for maximum intensity is given by $d(\sin\theta_i + \sin\theta_d) = n\lambda$, where d is the grating spacing, and θ_i and θ_d are the incident and diffracted angles respectively. The wavelengths from higher orders of reflections may be removed by positioning slits after the monochromator crystals.

Crystal monochromators are used for so-called 'hard' x-rays with short wavelengths ($\lambda < 6$Å); the spacing between atoms of a single crystal (e.g. Si(1 1 1)) are of a similar order to the x-ray wavelength. Typically, a double-crystal configuration is used, which further reduces the flux from unwanted wavelengths being allowed through. After monochromation, curved mirrors are then used to focus the beam, and slits further reduce the beam size for when it meets the sample.

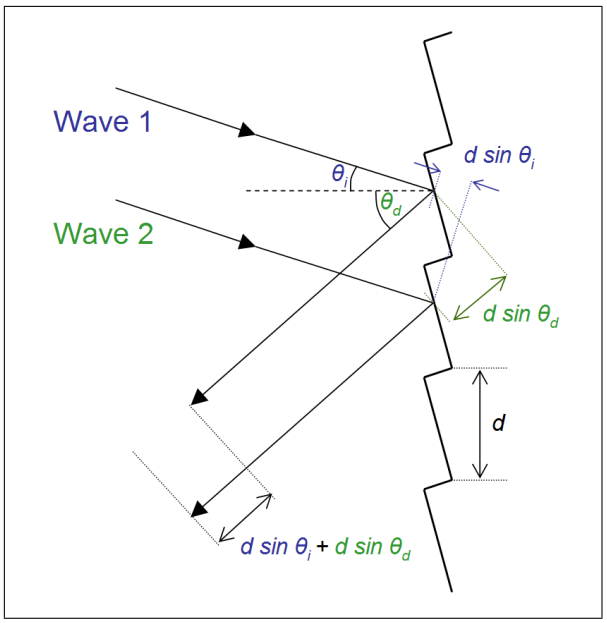

Figure 2.5: A 'sawtooth' diffraction grating of a monochromator. Two incoming waves are incident at equivalent points on the surface of the grating. d is the spacing between the gratings, θ_i and θ_d are the incident and diffracted (reflected) angles, respectively.

2.3.2 End-station details

At the end-stations where the experiment takes place, the samples are typically attached on the end of a liquid He cooled cryostat to allow low temperature measurements (~ 4 K). In some cases the samples are mounted on some form of manipulator arm, which allows the translation and rotation of the sample about multiple axes. Room temperature x-ray absorption spectroscopy (XAS) experiments can be performed at atmospheric pressure. If the sample is to be cryogenically cooled, the chamber must be in vacuum; any gases present condense onto surfaces inside the chamber. H_2O is one of the most difficult to remove, and it condenses mostly upon the coldest thing in the chamber, which is usually the sample itself. The build-up of ice can attenuate soft x-rays before reaching the sample, and reduce the signal-to-noise ratio. Generally, low-temperature XAS and XMCD do not require UHV conditions; below $\sim 10^{-5}$ mbar is usually sufficient.

Detection of the absorption signal may be made by several methods, including measurement of: (i) the drain current of the sample to detect the total electron yield (TEY) signal, (ii) the fluorescence yield (FY) by use of a photodiode, (iii) the transmitted x-ray

intensity, (iv) the x-ray reflection. The choice of which detection mode used depends on the type of sample; sometimes two modes can be measured simultaneously. Additionally, the x-ray intensity must be measured before it reaches the sample — this is the I_0 signal. The absorption signal is normalized to I_0 to account for fluctuations in beam intensity.

Sometimes an apparent drift in the position of an elemental absorption edge can occur, shifting slightly with respect to the photon energy, posing significant problems. Such shifts in the photon energy of the x-ray absorption can cause a derivative absorption signal to be present in the difference spectrum, which may be mistaken for a real dichroism. It is important to correct for these shifts to avoid spurious results. This is explained in detail in Chapter 5.

2.3.3 Beamlines used

5U.1 at SRS, Daresbury: The APPLE-II variable polarization undulator [3] on this beamline allows the selection of left- and right-circularly polarized x-rays, in addition to continuous variation between vertical and horizontal linear polarization. Typically the polarization is ∼70% for circular and ∼100% linear. The photon energy is selected with a plane-grating monochromator. The end-station may be fitted with either a flipper magnet, or (since 2006) a Portable Octopole Magnet System (POMS), which allows a magnetic field of up to 0.5 T to be applied in any direction. This is extremely useful for performing combined XMCD and XMLD experiments, where the magnetic field needs to be applied in parallel, antiparallel and perpendicular directions to the photon polarization, or particular crystalline axes. This beamline has been permanently closed since September 2008.

4.0.2 at ALS, Berkeley: This beamline [6] features the same APPLE-II model of helical undulator as 5U.1, but the Advanced Light Source (ALS) offers far greater flux, and better control of the proportion of circular polarization (≤98%). It uses a plane-grating monochromator, and also has the same type of octopole magnet system [7] as 5U.1.

ID08 at ESRF, Grenoble: This beamline is equipped with a 'Dragon' spectrometer [8], a grating monochromator designed for selection of soft x-ray photon energies. There are

several end-stations, which allow a greater number of experimental options. It has a low-temperature superconducting magnet, allowing magnetic fields up to 7 T. Nearly 100% circular/linear beam polarization is achievable. For one experiment, the POMS system from 5U.1 was installed as the end-station, to facilitate combined XMCD and XMLD measurements.

ID12 at ESRF, Grenoble: This beamline can perform XMCD like ID08, except in the hard x-ray regime ($2-20$ keV). It has 3 undulators which complement each other in terms of achievable photon fluxes in the desired energy range and helicity reversal time. We used the APPLE-II undulator in our experiments. A double-crystal, fixed exit monochromator (a pair of Si (1 1 1) crystals) was employed for the energy range used in our experiments, though there are other crystals available for higher energies. It offers exceptional beam stability, which is necessary when measuring the very small XMCD signal at transition metal K-edges. The magnet used was a 7 T superconducting system.

2.4 X-ray absorption

2.4.1 Absorption and decay process

X-ray Absorption Spectroscopy (XAS) is a technique used to probe the electronic configuration of a specific element within a material. Scanning the photon energy over the chosen element's absorption edge results in a sharp increase in the x-ray absorption. Electrons from an initial core state are promoted to the lowest unfilled state with allowed symmetry, just above the Fermi level. After absorption, the atom relaxes by one of two channels. In the Auger process, an intermediate electron recombines with the core hole and the energy of the excitation is carried away by the ejection of a secondary electron. The other channel is fluorescent photon emission, the inverse of the absorption process, where the excited electron recombines with the core hole and emits a photon.

2.4.2 Spectral structure

The strength of the x-ray absorption by an atom is primarily influenced by the occupancy of the initial state; more electrons in this level gives more opportunities for absorption of a photon. In a single-electron picture of absorption, the absorption edge is an abrupt discontinuity in the absorption coefficient. However, the XANES profile is normally complicated by several other interactions — such as a crystal field, multiplet effects, and polarization-dependent transition probability — which give it a profound fine structure. This can make it quite difficult to analyze, but the properties of core level initial states are quite simple, making it easier to extract information about the final states.

In a solid crystal, the formation of chemical bonds modifies the density of states in the valence band, which results in some significant modulation of the absorption intensity over the absorption edge. This can be broadly simulated by considering the symmetry of the system in a crystal field approximation.

There are also final-state effects which occur in the excited atom configuration. When the photoelectron enters the valence shell, the hole it leaves behind in the core level can give rise to multiplet interactions. These are a variety of distinct interactions between the different core and valence states, which produce peaks at corresponding distinct energies in the absorption spectrum. In insulators, the core-hole interaction with the localized valence states forms exciton states, which manifest as very narrow hydrogen-like absorption peaks in the absorption spectrum. In metals the core-hole is screened by the free carriers, so there is no interaction with the valence states, resulting in smooth broader peaks in the absorption spectrum. For materials with intermediate carrier concentrations, like (Ga,Mn)As, the core-hole is not fully screened, so some multiplet fine structure is still weakly evident.

A spin-orbit interaction of the core states can cause a large peak splitting in the absorption spectra, for example as seen in TM L-edge spectra, of the order of ~ 12 eV. The branching ratio of these spin-orbit split peaks is determined by the occupancy of the final state. In Chapter 4 this is exploited to qualitatively estimate the relative valency of different Mn atoms in (Ga,Mn)N. The ground state configuration of these core levels determines which of the final multiplet states are accessible to different photon polarizations accord-

ing to certain *selection rules*: transitions are either allowed or forbidden by the quantum numbers which define the system in its initial and final states.

2.4.3 Selection rules

Considering the transition as a two-step process, the electron is excited from a core state to a valence state. The initial and final states a and b are defined by a set of quantum numbers: the principle, orbital and magnetic quantum numbers (nlm_l) and $(n'l'm'_l)$, respectively. A dipolar transition $a \rightarrow b$ is defined by the dipole matrix element $|D_{ba}|$. The wavefunctions of a and b form the integral defining the matrix element. The matrix element can be expressed in radial and angular integral components: the former are always non-zero, but the angular integrals are only non-zero for certain values of (lm_l) and $(l'm'_l)$.

A dipole transition can only take place if $\Delta l = \pm 1$ and either $\Delta m = 0$ or $\Delta m = \pm 1$, in which case the transition is said to be *allowed*. These criteria are imposed because, for all other values of l and m, the angular integrals of the dipole matrix element vanish, *i.e.* there is no transition. Quadrupolar transitions ($\Delta l = \pm 2$) are much weaker, about 1% the probability of dipolar transitions. Transitions from p states to higher p states are forbidden, *i.e.* $\Delta l \neq 0$. A more detailed explanation of the origin of the electric dipole selection rules may be found in the book by Bransden and Joachain [9].

2.4.4 Practicalities of experiment

Real spectra

A typical K-edge As absorption spectrum is shown in figure 2.6(a), for the excitation from $1s$ to $4p$ level. The initial step region is called the XANES, and provides information on the electronic configuration of the element. The ensuing undulating region extending ~ 1 keV above the edge is known as the EXAFS, from which the structural environment of the material may be deduced. The intensity of the absorption edge is proportional to the amount of that element within the sample. A Mn L-edge absorption spectrum is shown in figure 2.6(b). The separate L_3 and L_2 edges arise from the spin-orbit splitting of the $2p$ core level (see inset). The L_3 region shows a strong 'white-line', or sharp peak, in contrast

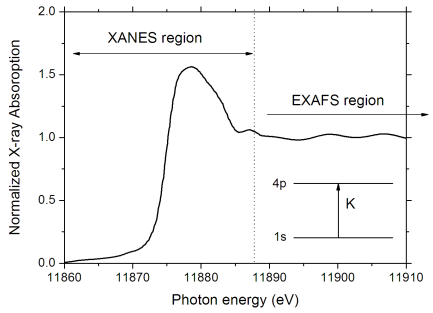

(a) As at the K-edge. The EXAFS region extends far off to the right towards higher photon energies. Inset: transition from $1s$ to $4p$ levels.

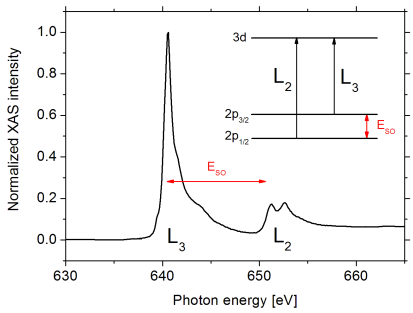

(b) Mn at the L-edge. Inset: schematic of the transitions from the spin-orbit split $2p$ level.

Figure 2.6: Typical absorption spectra for dipole transitions.

with the more step-like K-edge in figure 2.6(a). The multiplet splitting features are not very well defined here because the core states are screened by free carriers, weakening the core-valence states exchange interaction.

For Mn L-edge measurements, nearly all of the excitations decay by Auger emission, so TEY is most commonly used. At the K-edge of Mn and As, the ratio of fluorescence to Auger decay is nearly even, so either TEY or FY may be used. Figures comparing the proportion of excitation decay by Auger and fluorescence yields are presented in a paper by M. O. Krause [10]. The conductivity of the sample must also be considered when choosing the detection mode: if it is insulating, the TEY data may be distorted by charge building up on the sample.

Broadening

As with any experiment, the accuracy of the data collected at synchrotrons is limited by the equipment used, giving imperfect measurements of the physical effect. There is a Gaussian broadening of spectral features due to the finite energy resolution of the monochromator, which outputs a narrow band of wavelengths rather than a single wavelength. There is also an inherent Lorentzian broadening of the spectra, originating from the finite lifetime of the core-hole created during absorption.

Background subtraction

Besides giving information relating to the absorption edge of the element of interest, the absorption spectra contain a background of absorption from the other elements in the sample. Undesirable contaminants and oxides may add to the unwanted background information (for example, the Mn L-edge is about 100 eV above the O K-edge, in its EXAFS region). Other factors which may affect the spectra include a diminishing beam intensity (from the gradual decay of storage ring current), and secondary electron events (such as scattering and vibrational processes).

Generally absorption from the other elements is only very weakly dependent upon energy and may be accounted for by removing a linear function. However, it is not unusual to encounter spectra with nonlinear backgrounds. These can prove problematic, because to fit a function to the background relies on some sense of aesthetic and is very much subject to human judgement. An attempt to fit a difficult nonlinear background is included in Chapter 4.

2.5 XMCD

With XMCD, one can probe the magnitude and orientations of both orbital and spin magnetic moments of specific elements within a sample. Consequently, this versatile and powerful technique has become popular in recent years. It has been extensively used to measure magnetic metals, and has proven especially useful when applied to DMS. XMCD can probe specific elements of ferromagnetically ordered materials, but it is insensitive to antiferromagnetic order. This is because the signal is proportional to the average magnetic moment $\langle M \rangle$; the signal from parallel and antiparallel orientated spins cancel each other out.

The modern definition of *dichroism* is the polarization-dependence of a material's absorption of light. Dichroism occurs when the symmetry of the system is broken, for example by the ordering of chemical bonds, molecular chains, or by the presence of a magnetic or crystal field. A photon has a unit of spin angular momentum, $\hbar$, whose direction is determined by the polarization. Circularly polarized light has a rotating electric field vector.

For right-circular polarization (RCP), the photon carries one unit of angular momentum $+\hbar$ in its direction of motion; its *helicity* is $\sigma = +1$. For left-circular polarization (LCP), the angular momentum is $-\hbar$, opposite to the direction of motion, so $\sigma = -1$.

For positive helicity ($\sigma = +1$ is abbreviated to σ_+) and a magnetization along the same direction (denoted M_+), an absorption spectrum is obtained where $\Delta m_J = +1$ transitions are accessed; this spectrum is denoted I_+. An antiparallel alignment accesses the $\Delta m_J = -1$ transitions, resulting in an absorption spectrum denoted I_-. Reversing the magnetization for a fixed helicity should give the same spectra for parallel and perpendicular orientations. In practice, both σ and M are reversed to eliminate any experimental effects which are not due to the XMCD. Taking difference spectrum from I_+ and I_- gives the XMCD spectrum; the XMCD is obtained from four absorption spectra:

$$I_{\mathrm{XMCD}} = I_+ - I_- \tag{2.2}$$

where

$$I_+ = \left(\frac{I(\sigma_+, M_+) + I(\sigma_-, M_-)}{2} \right) \tag{2.3}$$

$$I_- = \left(\frac{I(\sigma_+, M_-) + I(\sigma_-, M_+)}{2} \right) \tag{2.4}$$

A schematic diagram of the density of states is shown in figure 2.7, depicting the spin-dependent absorption as a single-electron two-step process. The TM $2p$ core states are split by the spin-orbit interaction into $j = 3/2$ and $j = 1/2$ levels. The photon spin angular momentum is transferred to the *orbital* momentum of the absorbing electron, not its spin. However, in the presence of an on-site spin-orbit coupling, the electron's orbital and spin momenta align to the same axis. For this reason, the orientation of the spin makes the absorption sensitive to the photon polarization ('spin-up' and 'spin-down' are defined relative to the photon spin direction). RCP light preferentially excites spin-up electrons at the L_3-edge, because the orbital and spin angular momenta are parallel. On the other hand, at the L_2 edge the spin and orbital angular momenta are antiparallel, so RCP photons preferentially excite spin-down electrons. The reverse holds for LCP photons.

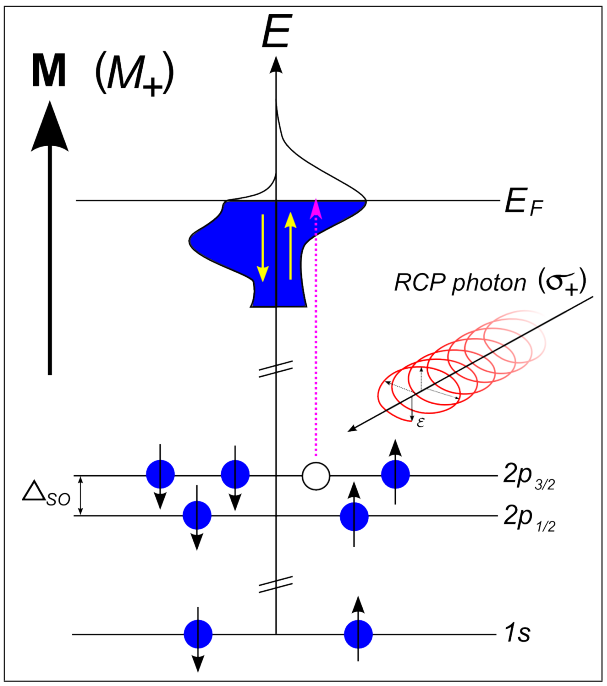

Figure 2.7: Schematic diagram depicting the absorption of a right-circular polarized photon by a electron from a spin-orbit-split core level, and its promotion into spin-split valence states.

This is the reason that, in an $L_{2,3}$ XMCD spectrum, the L_3 and L_2 peaks are opposite in sign.

In a ferromagnetic metal, the valence band states are split by the exchange interaction. The imbalance of unoccupied valence states above the Fermi level imposes a spin-dependent transition probability on the promoted electrons. By integrating the difference spectrum over the L_3 and L_2 edges, a dichroism is only observed if the valence shell has an orbital moment. The spin moment cannot be detected this way because both spin-up and spin-down states are summed over: to become sensitive to the spin moment, the difference spectrum must be integrated over the L_3 and L_2 edges separately. This is done is using sum rules.

2.5.1 Sum rules

The XMCD sum rules allow the separate determination of orbital [11] and spin [12] magnetic moments from the spectral features with elemental-specificity, and have been confirmed in many experimental studies [13–16]. From the general rules given in Refs. [11]

and [12], sum rules for specific transitions are shown below.

Orbital moment sum rule

From Thole et al. [11], the orbital magnetic moment $\langle L_z \rangle$ is determined from the parameter ρ:

$$\rho = \frac{\int_{j_+ + j_-} (I_+ - I_-)}{\int_{j_+ + j_-} (I_+ + I_- + I_0)} \tag{2.5}$$

$$= \frac{1}{2} \frac{c(c+1) - l(l+1) - 2}{l(l+1)(4l + 2 - n_e)} \langle L_z \rangle \tag{2.6}$$

Here, c and l denote the orbital angular momentum quantum number of the initial and final states, and n_e is the number of electrons in the shell of the final state. n_h, the number of holes in this shell, is equivalent to $(4l + 2 - n_e)$. I_+, I_-, and I_0 are the absorption with **B** applied parallel, antiparallel, and perpendicular to the photon angular momentum, respectively; similarly, j_+ and j_- indicate that the integration is over states with spin parallel and antiparallel to the photon angular momentum.
Let

$$p = \int_{j_+} (I_+ - I_-) \tag{2.7}$$

$$q = \int_{j_+ + j_-} (I_+ - I_-) \tag{2.8}$$

$$r = \int_{j_+ + j_-} (I_+ + I_-) \tag{2.9}$$

so 2.5 becomes:

$$\rho = \frac{q}{\frac{3}{2} r} \tag{2.10}$$

Let us first consider the following dipole transitions:
For $s \rightarrow p$ transitions, $c = 0$ and $l = 1$:

$$\rho = -\frac{4}{4} \frac{\langle L_z \rangle}{n_h}$$

$$\langle L_z \rangle = -\frac{2}{3} \frac{q}{r} n_h \tag{2.11}$$

For $p \rightarrow d$ transitions, $c = 1$ and $l = 2$:

$$\begin{aligned} \rho &= -\frac{1}{2}\frac{\langle L_z \rangle}{n_h} \\ \langle L_z \rangle &= -\frac{4}{3}\frac{q}{r} n_h \end{aligned} \tag{2.12}$$

For $p \rightarrow s$ transitions, $c = 1$ and $l = 0$:

$$\begin{aligned} \rho &= -\frac{0}{2}\frac{\langle L_z \rangle}{n_h} \\ \langle L_z \rangle &= 0 \end{aligned} \tag{2.13}$$

because an s state cannot have orbital angular momentum.

The orbital moment is given by $m_l = -\langle L_z \rangle \mu_B$.

Spin moment sum rule

From the paper by Carra et al. [12], the spin-dependent part of the local magnetic field per hole is given by:

$$\delta = \frac{\int_{j_+} d\omega(I_+ - I_-) - [(c+1)/c]\int_{j_-} d\omega(I_+ - I_-)}{\int_{j_+ + j_-} d\omega(I_+ + I_- + I_0)} \tag{2.14}$$

$$= \frac{l(l+1) - 2 - c(c+1)}{3c(4l + 2 - n_e)} \langle S_z \rangle + \frac{l(l+1)[l(l+1) + 2c(c+1) + 4] - 3(c-1)^2(c+2)^2}{6lc(l+1)(4l + 2 - n_e)} \langle T_z \rangle \tag{2.15}$$

For a $p \rightarrow d$ transition, $c = 1$ and $l = 2$:

$$\begin{aligned} \delta &= \frac{6 - 2 - 2}{3(10 - n_e)} \langle S_z \rangle + \frac{6(6 + 4 + 4) - 0}{36(10 - n_e)} \langle T_z \rangle \\ &= \frac{2}{3}\frac{\langle S_z \rangle}{n_h} + \frac{7}{3}\frac{\langle T_z \rangle}{n_h} \end{aligned} \tag{2.16}$$

Combining Equations 2.7 and 2.8 gives $(q - p) = \int_{j_-} d\omega(I_+ - I_-)$, so Equation 2.14 can be rewritten as:

$$\delta = \frac{p - \frac{c+1}{c}(q - p)}{\frac{3}{2}r}$$

so for $c = 1$,

$$\delta = \frac{6p - 4q}{3r} \tag{2.17}$$

Combining Equations 2.16 and 2.17 gives

$$\frac{2}{3}\frac{\langle S_z \rangle}{n_h} + \frac{7}{3}\frac{\langle T_z \rangle}{n_h} = \frac{6p - 4q}{3r}$$
$$2\langle S_z \rangle = \frac{6p - 4q}{r} n_h - 7\langle T_z \rangle$$

The spin magnetic moment $m_{spin} = -g\langle S_z \rangle$, where the Landé g-factor is taken as $g = 2$, so:

$$m_s = -\frac{6p - 4q}{r} n_h + 7\langle T_z \rangle \tag{2.18}$$

$\langle T_z \rangle$ is the expectation value of the magnetic dipole operator. It is a measure of the anisotropy of the spin distribution; for systems with cubic symmetry it is zero, so for our purposes this term is negligible.

Additional considerations

There are two additional factors which must be accounted for when determining the magnetic moments, and are not included in the equations above. The first is that the degree of circular polarization of the light used, P, decreases the magnetic moment values obtained from sum rules — except for 100% circular polarization ($P = 1$). The second consideration is that in localized systems the $2p_{3/2}$ and $2p_{1/2}$ core levels can mix, caused by interactions between the core and valence states. This necessitates a correction factor which is dependent upon the type of ion. In the case of the Mn $L_{2,3}$-edge, $C = 1.47$; this value is derived by comparing calculated spectra with their ground state moments [13].

Including these extra factors, the L-edge XMCD sum rules used for $2p$ to $3d$ transitions

are (neglecting $\langle T \rangle$):

$$\mu_{orb} = -\frac{4q}{3rP}(10 - n_d) \tag{2.19}$$

$$\mu_{spin} = -\frac{6p - 4q}{rP}(10 - n_d) \times C \tag{2.20}$$

n_d is the number of electrons in the $3d$ band; for Mn n_d taken to be 5.1, because the sign of the Mn orbital and spin moments are parallel in (Ga,Mn)As [13], and photoemission experiments indicate that the number of d electrons in Mn is of this order [17].

2.6 XMLD

The XMLD technique, discovered even before XMCD was observed [18], is the linearly-polarized counterpart of XMCD. The XMLD signal is proportional to $\langle M^2 \rangle$, so both ferro- and antiferromagnetically ordered moments contribute to its signal. It is sensitive to the magnetization axis of a material rather than its direction, so it is well suited to studying the spin orientation of ordered antiferromagnets [19, 20] and frustrated ferromagnetic interactions [21]. XMLD also offers the possibility to directly probe the anisotropy of the spin-orbit interaction, which is proportional to the magnetocrystalline anisotropy energy [22–24].

For linearly-polarized light, the angular momentum direction is determined by the electric field vector, $\boldsymbol{\varepsilon}$, which points perpendicular to the photon wavevector $\mathbf{k}$ and oscillates at a frequency determined by the photon energy. The XMLD signal comes from the difference in absorption spectra taken for parallel and perpendicular orientations of $\boldsymbol{\varepsilon}$ and sample magnetization axis $\mathbf{M}$. Typical XMLD experimental geometry has the beam in normal incidence, with the sample magnetized in-plane. If the magnetization were set to be horizontal to the ground, parallel and perpendicular orientations of $\boldsymbol{\varepsilon}$ and $\mathbf{M}$ would be achieved by setting the polarization to be horizontal and then vertical. As with XMCD, the magnetization direction must also be changed, to eliminate effects which are not due to the XMLD. Therefore the XMLD spectrum is obtained from:

$$XMLD = I_{\parallel} - I_{\perp} \tag{2.21}$$

where

$$I_{\parallel} = \frac{I(\varepsilon_{\uparrow}, M_{\uparrow}) + I(\varepsilon_{\rightarrow}, M_{\rightarrow})}{2} \tag{2.22}$$

$$I_{\perp} = \frac{I(\varepsilon_{\uparrow}, M_{\rightarrow}) + I(\varepsilon_{\rightarrow}, M_{\uparrow})}{2} \tag{2.23}$$

The oscillation of the electric field vector means that the $\mathbf{M} \parallel \boldsymbol{\varepsilon}$ orientation allows both $\Delta M_J = +1$ and $\Delta M_J = -1$. When $\mathbf{M} \perp \boldsymbol{\varepsilon}$, angular momentum is still transferred to the electron, but not along the quantization axis (i.e. the magnetization axis). In this case $\Delta M_J = 0$, meaning non-magnetic absorption. Thus, the XMLD signal comes from the difference in absorption for $\Delta M_J = \pm 1$ and $\Delta M_J = 0$.

2.6.1 Sum rule

The sum rule developed for XMLD allows the evaluation of the anisotropic spin-orbit coupling, which is proportional to the MAE [22,23]. XMLD also scales with the anisotropy in the spin-orbit interaction, λ_a, and the final-state exchange interaction [25,26]. The sum rule is presented here as stated in [24]. For uniaxial symmetry:

$$MAE = \frac{\zeta \lambda_a}{2} = \zeta n_h \frac{4\sqrt{3}}{5} \frac{(s - 2t)}{u} \tag{2.24}$$

$$s = \int_{j_+} \left(I_{\parallel} - I_{\perp}\right) \tag{2.25}$$

$$t = \int_{j_-} \left(I_{\parallel} - I_{\perp}\right) \tag{2.26}$$

$$u = \int_{j_+ + j_-} \left(I_{\parallel} + I_{\perp}\right) \tag{2.27}$$

where n_h is the number of holes in the $3d$ band, ζ is the radial part of the spin-orbital interaction, and $(s + t)$ and u are the integrated intensities over the $L_{2,3}$ edges of the absorption spectra and XMLD spectra, respectively.

2.7 The Problem of Saturation and Self-Absorption

2.7.1 Description

It is important to be aware that XAS measurements do not always record the true absorption coefficient for certain detection modes and experimental geometries. Spectra measured by FY may strongly depend on the elemental composition, sample thickness and detection geometry when concentrated or thick samples are measured: this is due to the *saturation* effect. On the other hand, TEY spectra are less prone to this problem, and are a more reliable measure of the absorption cross-section [27] (although TEY is not immune to saturation, as shown in the case of bulk ferromagnetic metals [28]).

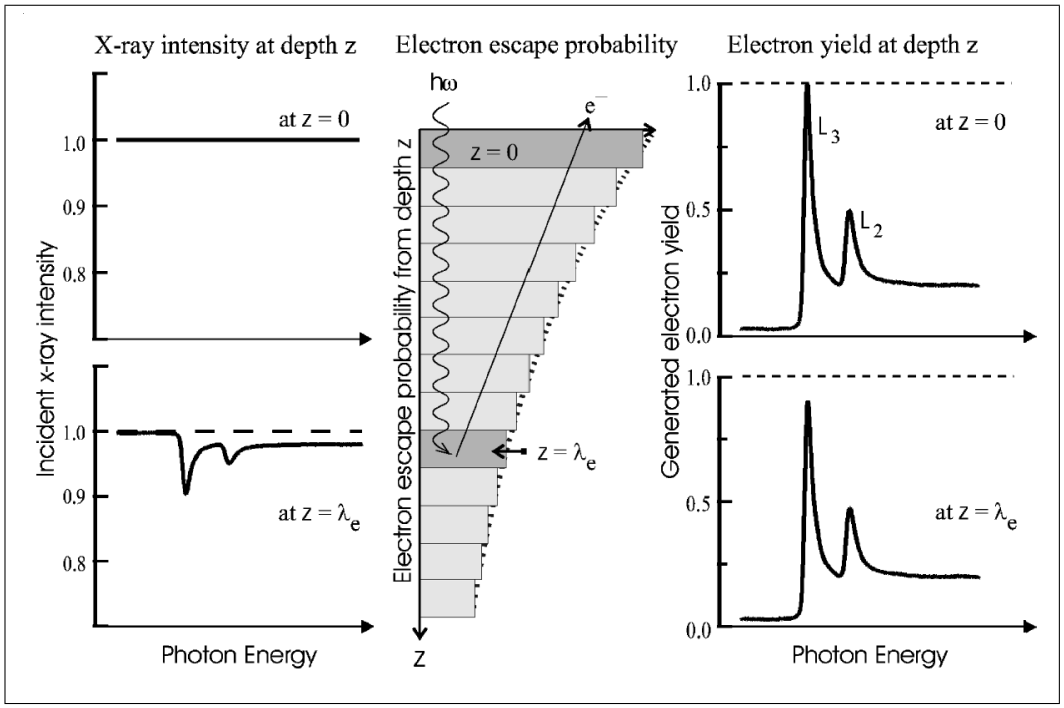

Figure 2.8: Illustration of the saturation effect in TEY. Left: the difference in x-ray intensity arriving at the surface and at a depth λ_e. Centre: probability of electron escape as a function of depth z, equal to unity for $z = 0$. Right: hypothetical absorption spectra from the layers at depths of $z = 0$ and $z = \lambda_e$. Figure taken from Nakajima et al. [28].

In sufficiently thick or concentrated samples, the attenuation length of incident photons may be less than, or on the order of, the information depth (the escape depth of Auger electrons or fluorescence photons). In this case, the photon intensity profile arriving at deeper absorbing atoms is diminished at the atom's absorption edges, especially if the

edge has a strong 'white line' like the Mn L-edge. Beyond the attenuation length of the absorbing atom, the photon intensity at the absorption edge approaches zero, so that the measured absorption peaks reach a maximum (i.e. *saturated*), while the other regions of the spectrum can increase yet further. The effect on the absorption spectrum is to curb the intensity of the largest absorption peaks compared to the rest of the spectrum: they seem to become diminished and broadened, sometimes with an apparent energy shift of the peak [29]. This distortion is well illustrated in figure 2.8, taken from Ref. [28]. Detection modes whose information depth is much less than the photon penetration depth (such as TEY) are much less prone to saturation.

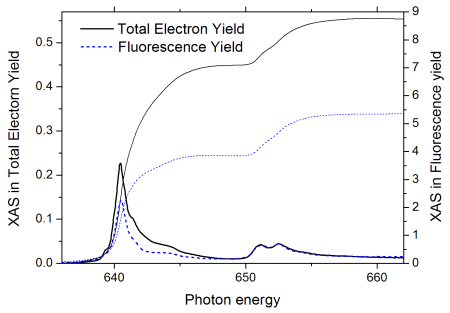

(a) Mn022 (2% Mn) XAS

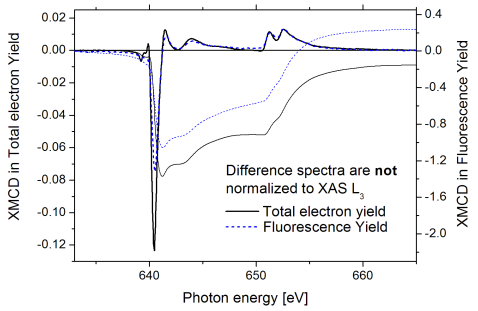

(b) Mn022 (2% Mn) XMCD

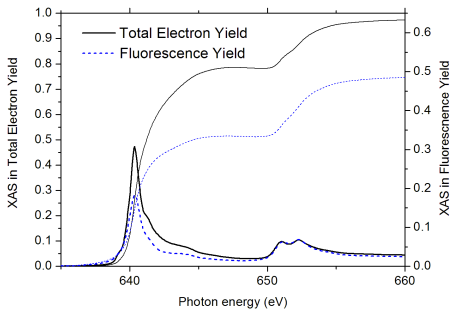

(c) Mn110 (8% Mn) XAS

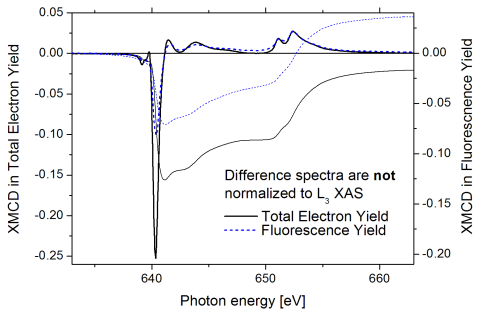

(d) Mn110 (8% Mn) XMCD

Figure 2.9: Comparison of TEY (solid line) and FY (dashes) measurements on the same samples, at $B = 2$ T and $T = 6$ K. 5th-order polynomial functions were subtracted to remove the nonlinear backgrounds of the summed absorption spectra. The angle of incidence from the sample surface for (a) and (b) is 10°; for (c) and (d) it is 20°.

Self-absorption occurs when emitted photons or photoelectrons are re-absorbed before

they can exit the material. When atoms deep in the sample receive a saturated photon intensity profile, the fluorescence photons have a chance of being re-absorbed before they escape the sample. Therefore, self-absorption actually acts to prevent saturated absorption information from being measured, mitigating the saturation effect. The 'self-absorption effect' often referred to in the literature [30, 31] actually refers to the distortion of spectra caused by a *lack* of self-absorption. Unfortunately, the terms saturation and self-absorption are often used interchangeably, which further obfuscates matters. In this thesis, the term *saturation effect* will be preferentially used when referring to the effect which distorts spectra, while *self-absorption* is used to simply describe the re-absorption of fluorescence photons (or indeed Auger electrons).

Spectra taken at a grazing angle of incidence and normal angle of emission (with respect to the sample surface) are likely to be most prone to saturation, because the incoming photons must pass a greater distance through the sample than the fluorescence photons do to exit the material. Conversely, choosing normal incidence and grazing emission angle is the best arrangement to minimize the saturation effect.

Figure 2.9 shows both TEY and FY absorption and XMCD spectra for two (Ga,Mn)As samples, having 2% and 8% nominal Mn content. Both samples were measured in grazing incidence, at 10° and 20° to the sample surface, respectively. FY is collected at 90° to the incident photon direction. The vertical axis has been scaled so that the L_2 features appear to be the same height, emphasizing the huge suppression seen in the L_3 peak of the FY spectra. From the integrated absorption spectra (2.9(a) and 2.9(c)), it is clear that the branching ratio is smaller for FY. In the XMCD (2.9(b) and 2.9(d)), the features in the FY measurement have broadened so much that the pre-edge feature of the L_3 peak is absent. The distortion is significantly greater in the more concentrated sample, as one might expect (despite it being measured at a more oblique grazing angle). The suppression of the FY XMCD L_3 peak is so great that its integrated spectrum implies a negative orbital magnetic moment, opposite in sign to that measured by TEY; this demonstrates how saturation-affected data can result in huge errors.

2.7.2 Correction for saturation effect

It has been demonstrated that the distortion caused by the saturation effect may be reversed entirely. Mostly this has been applied to the EXAFS region of absorption spectra [31, 32]. This method may also be applied to the XANES region [29, 30], but the presence of the absorption edge makes it much more difficult. To determine if saturation significantly affects our spectra in Chapters 4 and 5, the correction procedure used by Iida and Noma [30] is followed. In their paper, they successfully reverse the distortion of the FY so that the adjusted spectrum closely resembles the TEY, which is negligibly affected by saturation in their experiment.

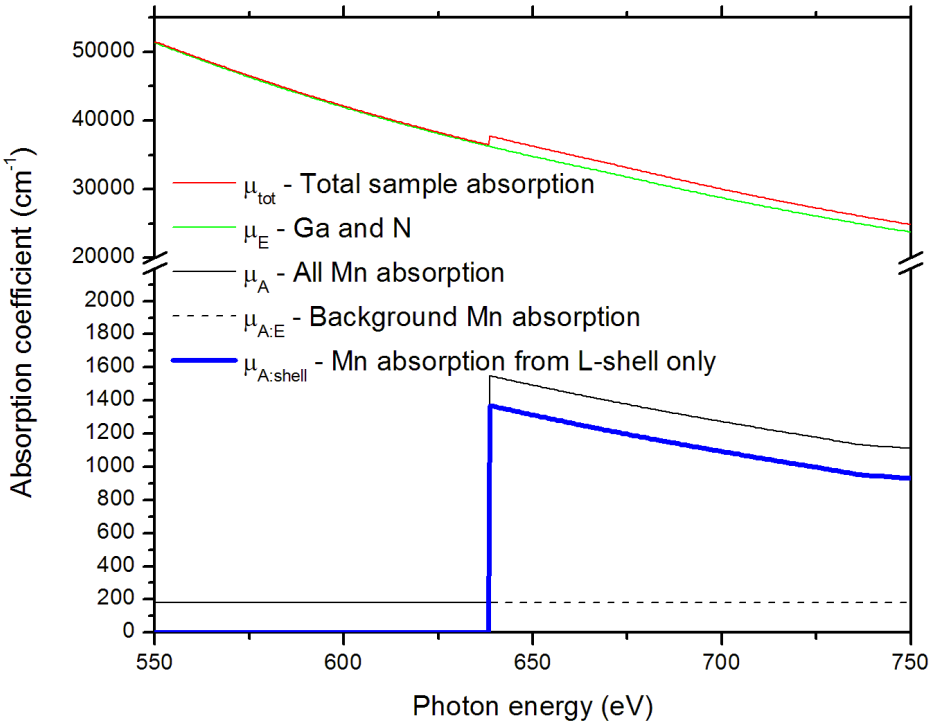

Figure 2.10: Absorption coefficients calculated for $Ga_{0.98}Mn_{0.02}N$, obtained from elemental attenuation lengths from data tables published by Henke *et al* [33].

To correct the experimental fluorescence spectra for the saturation effect, the distortion must be modelled using calculated absorption coefficients for each of the constituent atoms.

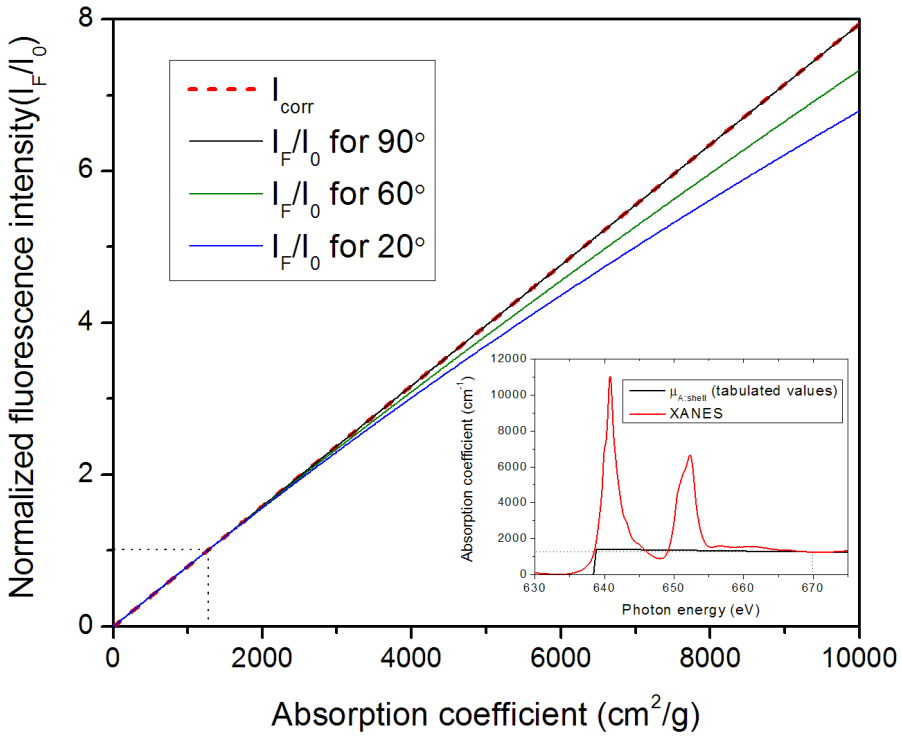

Figure 2.11: Calibration curve for correcting the saturation effect upon $Ga_{0.98}Mn_{0.02}N$. Curves calculated for angles of incidence at 90°(black line), 60°(green) and 20°(blue) to the sample surface. Inset: the experimental spectrum is scaled so the absorption coefficient matches the calculated values in the post-edge region (∼670 eV).

The absorption coefficient, μ, determines how quickly the x-ray intensity is attenuated as it passes through a material, as described by the Lambert-Beer Law:

$$I(E) = I_0 e^{-\mu(E)x} \tag{2.28}$$

where the x-ray intensity at a given energy, $I(E)$, decays exponentially with distance into the sample, x.

The total absorption coefficient of a material, μ_{tot}, is the sum of the absorption coefficients from the atom of interest A (denoted μ_{A}), and from the material *excluding* the atom of interest (denoted μ_{E}), respectively. The absorption coefficient of a material may be estimated by considering its constituent elements. The attenuation lengths of each element

can be obtained from data tables [33]* for densities of 1 g cm^{-3}; their reciprocals then give the mass absorption coefficients. Multiplying the attenuation length of each element by their individual densities in this material gives their particular absorption coefficients, which may then be summed to give the total absorption coefficient for this material, μ_{tot}. An estimate of the attenuation length of the material is given by $1/\mu_{\mathrm{tot}}$.

μ_{A} can be thought of as being composed of the absorption due to the photoionization to the shell of interest, $\mu_{\mathrm{A:shell}}$, and the absorption coefficient of element A *excluding* photoionization to the shell of interest, $\mu_{\mathrm{A:E}}$. Thus:

$$\mu_{\mathrm{tot}} = \mu_{\mathrm{E}} + \mu_{\mathrm{A}} \tag{2.29}$$

where

$$\mu_{\mathrm{A}} = \mu_{\mathrm{A:E}} + \mu_{\mathrm{A:shell}} \tag{2.30}$$

These are depicted for the example of $Ga_{0.98}Mn_{0.02}N$ in figure 2.10. Note that the As K-edge here is an abrupt discontinuity in the absorption coefficient because initial- and final-state effects are neglected. It is straightforward to subtract μ_{E} from the experimental data. Over the energy range of the absorption spectrum (typically 60 eV), $\mu_{\mathrm{A:E}}$ is almost independent of energy; therefore a constant offset is subtracted from μ_{A} before the edge-jump to obtain $\mu_{\mathrm{A:shell}}$. The saturation correction is greatly simplified with the assumption that the background is independent of photon energy.

Now the x-ray fluorescence intensity may be modelled as a function of absorption coefficient $\mu_{\mathrm{A:shell}}$:

$$I_f \propto I_0 \cdot \frac{\mu_{\mathrm{A:shell}}}{\mu_{\mathrm{tot}} + \mu_{\mathrm{tot}}(\mathrm{E_{fl}}) \sin\alpha / \sin\beta} \left(1 - \exp\left[-\frac{\mu_{\mathrm{tot}}}{\sin\alpha} - \frac{\mu_{\mathrm{tot}}(\mathrm{E_{fl}})}{\sin\beta}\right] t\right) \tag{2.31}$$

Here, t is the sample thickness, α is the angle of x-ray incidence from the sample surface, β is the angle of fluorescence emission, and $\mu_{\mathrm{tot}}(\mathrm{E_{fl}})$ is the sample's absorption coefficient at the fluorescence energy, taken to be independent of energy.

Figure 2.11 shows I_f/I_0 for three different angles of incidence, and I_{corr}, which is the

*A very useful website is associated with this publication: `http://henke.lbl.gov/optical_constants/`

'corrected' fluorescence (i.e. directly proportional to the absorption coefficient). The curves are for a hypothetical $(Ga_{0.98}Mn_{0.02})N$ sample. The experimental data are normalized to $\mu_{\text{A:shell}}$ at the post-edge region (shown in the inset to figure 2.11). I_f/I_0 and If_{corr} are then normalized to unity at this value of the absorption coefficient (indicated by the dotted line in figure 2.10).

The conditions which are likely to result in saturation include: small α, large β, high density of element A, and $t \gtrsim$ penetration depth of fluorescence photon. Under these conditions, I_f becomes nonlinear as a function of absorption coefficient. This is well demonstrated in figure 2.11, which shows I_f/I_0 becoming more curved for increasingly acute angles of photon incidence. This then serves as a calibration curve, which may be applied to the experimental spectra (normalized to match the post-edge region — see inset to figure 2.11)[†].

The calibration curve shown in Ref. [30] only covers the range of relative fluorescence intensity (I_f/I_0) up to 1; this shows that saturation causes the intensity to be augmented in most regions. As such, their correction *reduces* the intensity of the fluorescence data. In contrast, the calibration curve presented in figure 2.11 is for the L-edge of Mn, for which the intensities of the L_3 and L_2 peaks extend to many times that of the edge step. This shows saturation has caused the intensity to be diminished, most strongly in the peak regions so the correction used here *increases* the intensity of the fluorescence.

[†]The experimental data shown in this figure are L-edge Mn spectra for a $(Ga_{1-x}Mn_x)N$ sample, with $x \simeq 0.02$

References

[1] D. Attwood, Soft X-Rays and Extreme Ultraviolet Radiation, Online Lecture Series, 2007.

[2] S. Sasaki, K. Miyata, and T. Takada, *Japanese Journal of Applied Physics* **31**, L1794 (1992).

[3] S. Sasaki, *Nuclear Instruments and Methods in Physics Research: Section A* **347**, 83 (1994).

[4] G. Margaritondo, *Elements of Synchrotron Light for Biology, Chemistry, and Medical Research*, Oxford University Press, 2002.

[5] D. Attwood, *Soft X-Rays and Extreme Ultraviolet Radiation - Principles and Applications*, Cambridge University Press, 2007.

[6] A. T. Young, J. Feng, E. Arenholz, H. A. Padmore, T. Henderson, S. Marks, E. Hoyer, R. Schlueter, J. B. Kortright, V. Martynov, C. Steier, and G. Portmann, *Nuclear Instruments and Methods in Physics Research Section A: Accelerators, Spectrometers, Detectors and Associated Equipment* **467-468**, 549 (2001).

[7] E. Arenholz and S. O. Prestemon, *Review of Scientific Instruments* **76**, 083908 (2005).

[8] C. T. Chen and F. Sette, Performance of the Dragon soft x-ray beamline (invited), volume 60, pp. 1616–1621, AIP, 1989.

[9] B. H. Bransden and C. J. Joachain, *Quantum Mechanics*, Prentice Hall, 2nd edition, 2000.

[10] M. O. Krause, *J. Phys. Chem. Ref. Data* **8**, 307 (1979).

[11] B. T. Thole, P. Carra, F. Sette, and G. van der Laan, *Physical Review Letters* **68**, 1943 (1992).

[12] P. Carra, B. T. Thole, M. Altarelli, and X. Wang, *Physical Review Letters* **70**, 694 (1993).

[13] K. W. Edmonds, N. R. S. Farley, T. K. Johal, G. van der Laan, R. P. Campion, B. L. Gallagher, and C. T. Foxon, *Physical Review B* **71**, 064418 (2005).

[14] H. Ohldag, V. Solinus, F. U. Hillebrecht, J. B. Goedkoop, M. Finazzi, F. Matsukura, and H. Ohno, *Applied Physics Letters* **76**, 2928 (2000).

[15] H. A. Dürr, G. van der Laan, D. Spanke, F. U. Hillebrecht, and N. B. Brookes, *Physical Review B* **56**, 8156 (1997).

[16] C. T. Chen, Y. U. Idzerda, H. J. Lin, N. V. Smith, G. Meigs, E. Chaban, G. H. Ho, E. Pellegrin, and F. Sette, *Physical Review Letters* **75**, 152 (1995).

[17] J. Okabayashi, A. Kimura, O. Rader, T. Mizokawa, A. Fujimori, T. Hayashi, and M. Tanaka, *Phys. Rev. B* **58**, R4211 (1998).

[18] G. van der Laan, B. T. Thole, G. A. Sawatzky, J. B. Goedkoop, J. C. Fuggle, J.-M. Esteva, R. Karnatak, J. P. Remeika, and H. A. Dabkowska, *Physical Review B* **34**, 6529 (1986).

[19] D. Alders, L. H. Tjeng, F. C. Voogt, T. Hibma, G. A. Sawatzky, C. T. Chen, J. Vogel, M. Sacchi, and S. Iacobucci, *Physical Review B* **57**, 11623 (1998).

[20] M. W. Haverkort, S. I. Csiszar, Z. Hu, S. Altieri, A. Tanaka, H. H. Hsieh, H. J. Lin, C. T. Chen, T. Hibma, and L. H. Tjeng, *Physical Review B* **69**, 020408 (2004).

[21] C. Grazioli, D. Alfe, S. R. Krishnakumar, S. S. Gupta, M. Veronese, S. Turchini, N. Bonini, A. D. Corso, D. D. Sarma, S. Baroni, and C. Carbone, *Physical Review Letters* **95**, 117201 (2005).

[22] G. van der Laan, *Physical Review Letters* **82**, 640 (1999).

[23] S. S. Dhesi, G. van der Laan, E. Dudzik, and A. B. Shick, *Physical Review Letters* **87**, 067201 (2001).

[24] S. S. Dhesi, G. van der Laan, and E. Dudzik, *Applied Physics Letters* **80**, 1613 (2002).

[25] G. van der Laan, *Physical Review B* **55**, 8086 (1997).

[26] J. Kuneš and P. M. Oppeneer, *Physical Review B* **67**, 024431 (2003).

[27] F. M. F. de Groot, M. A. Arrio, P. Sainctavit, C. Cartier, and C. T. Chen, *Solid state communications* **92**, 991 (1994).

[28] R. Nakajima, J. Stöhr, and Y. U. Idzerda, *Physical Review B* **59**, 6421 (1999).

[29] S. Eisebitt, T. Böske, J.-E. Rubensson, and W. Eberhardt, *Phys. Rev. B* **47**, 14103 (1993).

[30] A. Iida and T. Noma, *Jpn. J. Appl. Phys.* **32**, 2899 (1993).

[31] P. Pfalzer, J.-P. Urbach, M. Klemm, S. Horn, M. L. denBoer, A. I. Frenkel, and J. P. Kirkland, *Phys. Rev. B* **60**, 9335 (1999).

[32] L. Tröger, D. Arvanitis, K. Baberschke, H. Michaelis, U. Grimm, and E. Zschech, *Phys. Rev. B* **46**, 3283 (1992).

[33] B. Henke, E. Gullikson, and J. Davis, *Atomic Data and Nuclear Data Tables* **54**, 181 (1993).

Chapter 3

XMLD and XMCD studies of (Ga,Mn)As

3.1 Introduction

This chapter embodies the results of several experiments, using XMLD and XMCD at the $L_{2,3}$ edge of Mn. We observe a hugely anisotropic XMLD signal from single-crystal (Ga,Mn)As. An interesting increase in the XMLD signal upon annealing indicates that, in as-grown material, there must be a significant proportion of the Mn moments which are neither ferro- nor antiferromagnetically aligned to the average magnetization axis. This leads on to the investigation into the nature of the magnetization deficit well-observed in (Ga,Mn)As, using the combined techniques of XMLD, XMCD and SQUID magnetometry.

3.1.1 Previous XMCD and XMLD studies

XMCD has proved to be an invaluable tool for studying the ferromagnetic semiconductor (Ga,Mn)As. A huge deficit in magnetization was observed in early XMCD studies [1, 2], before the importance of removing any Mn-rich oxide layers from the sample surface was known [3]. Some experimental studies have observed paramagnetic components to the XMCD spectrum [4, 5], which they ascribe to the presence of Mn_I. However, in these studies the separated XMCD para- and ferromagnetic components are shifted in energy; Mn_{Ga} and Mn_I are both in the Mn^{2+} oxidation state and are not easily distinguishable

within typical experimental resolution. It is possible that some (unoxidized) surface Mn may be responsible for this signal; paramagnetic behaviour has been observed in small amounts of Mn ($\ll 1$ ML) on semiconductor surfaces [6], and surface-etched as-grown and annealed (Ga,Mn)As show no sign of paramagnetic behaviour [7].

The technique of XMLD, discovered even before XMCD was observed [8], is now rapidly gaining in popularity, particularly for studies of spin orientation in ordered antiferromagnets [9–11], including applications such as photoelectron emission microscopy (PEEM) [12,13]. While XMCD is related to the average magnetic moment $\langle M \rangle$ along the light polarization direction and therefore only sensitive to ferromagnetic order, XMLD is related to $\langle M^2 \rangle$, so that both ferro- and antiferromagnetic moments contribute to the XMLD spectrum. XMLD also offers the possibility to directly probe the anisotropy of the spin-orbit interaction, which is proportional to the magnetocrystalline anisotropy energy [14–16]. To date, however, there have been relatively few reported studies of XMLD in ferromagnetic systems [16, 17], because both the measurement and interpretation are significantly more challenging than XMCD. This lack of exploration is unfortunate, since ferromagnets offer a key advantage over antiferromagnets for developing a quantitative understanding of XMLD: the magnetization can be rotated using an external magnetic field, allowing magnetic and non-magnetic contributions to the polarization-dependent x-ray absorption to be unambiguously distinguished [10, 14].

The dependence of XMCD on $\langle M \rangle$ means the signal vanishes for antiferromagnetic order. The ferromagnetic moment of as-grown (Ga,Mn)As is reduced from its expected value of 5 μ_B/Mn [7,18], and XMCD measurements at high magnetic field (≤ 5 T) indicate an antiferromagnetic coupling besides the ferromagnetic order. XMLD measurements are the logical next step to further illuminate the behaviour of this material.

3.1.2 Theories of magnetization suppression in (Ga,Mn)As

The 'magnetization deficit' observed in untreated (Ga,Mn)As thin films, referred to in Chapter 1, is addressed in the present Chapter. Although Mn_I accounts for the majority of the suppression in untreated (Ga,Mn)As, there has been much investigation into the intrinsic properties of DMS which inhibit the maximum magnetization. There are a number

of possibilities, most investigated by theoretical approaches. The influences contributing to this deficit may be either intrinsic or extrinsic to the system.

Intrinsic mechanisms: A significant negative contribution to the magnetization is expected from the itinerant charge carriers [19], $\sim 1\ \mu_B$ per hole from first principles. More involved approaches find the hole magnetization to be $\sim 5-10\%$ of the Mn moment [18]. The suppression is seen to increase with hole concentration in both theory [18, 20] and experiment [21]. The hole magnetization is a likely cause of the small magnetization suppression of $\sim 0.5\ \mu_B$ that exists in 'uncompensated' annealed (Ga,Mn)As. The As and Ga $4p$ orbital contribution to the hole moment is measured directly in Chapter 5.

Orientational [22] and positional [23, 24] disorder of the Mn local moments can lead to anisotropic Mn-Mn interactions; magnetic frustration arising from this could lead to non-collinearity in the ferromagnetic order and suppress the bulk magnetization. A realistic six-band model treatment [25] finds that the anisotropy effects, having been overestimated by simpler models, are too weak to account for a significant magnetization reduction by non-collinearity. Long-range spin fluctuations are also considered as an intrinsic origin of non-collinearity [24, 26] for systems with strong localization. This effect is not likely to be important though because our material is relatively delocalized, and a more realistic band model [27] finds the sign oscillations to be very small, implying that the magnetization suppression is mostly due to extrinsic effects.

Extrinsic mechanisms: The two main compensating defects occurring in (Ga,Mn)As are interstitial Mn ($\mathrm{Mn_I}$) and As antisites ($\mathrm{As_{Ga}}$). The latter can be largely avoided by using low growth temperatures and growing with As dimers [28]. $\mathrm{Mn_I}$ has been shown to be the main cause of the suppression of both magnetization and hole concentration [29–31] and is even more detrimental than $\mathrm{As_{Ga}}$ to the material's magnetic properties: not only does each $\mathrm{Mn_I}$ atom compensate two valence band holes, but it directly compensates the local magnetic moment by coupling antiferromagnetically to $\mathrm{Mn_{Ga}}$. Evidence of antiferromagnetic coupling in (Ga,Mn)As has been observed [7, 32], but the precise magnetic behaviour of the $\mathrm{Mn_{Ga}}$-$\mathrm{Mn_I}$ pairs has not yet been fully investigated.

Korzhavyi et al. [20] use density functional theory (DFT) calculations to show that a suppression of the hole concentration — in their case induced by the presence of double donor As_{Ga} antisites — promotes the formation of a disordered local moment (DLM). This means the orientation of the Mn spins are not fully collinear to the global magnetization vector, which reduces the average local moment per Mn. There have been no studies to date refuting the formation of a DLM state as a result of hole suppression, and this remains a reasonable explanation for the experimental observations.

3.2 Experimental details

3.2.1 Sample details

Single crystal (Ga,Mn)As films are prepared *ex-situ* by low-temperature MBE upon GaAs(001) substrates. Full details of the growth are given elsewhere [28]. The samples are annealed in air for $50 - 150$ hours at 190°C to optimize the electrical and magnetic properties [33]. The samples are then etched using concentrated HCl, just before mounting in the beamline experimental chamber, in order to remove surface oxides [3]. Their details are shown in Table 3.1.

Sample	Real name	Treatment	Mn content	Film thickness
A	Mn220a	Annealed	7%	25 nm
B	Mn193	As-grown	7.5%	50 nm
C	Mn228a	Annealed	3%	25 nm
D	Mn228ag	As-grown	3%	25 nm

Table 3.1: List of sample details for those measured at the ALS. There is typically a $\sim 10\%$ error associated with the nominal Mn concentration

Another study, following the same design as above, was conducted at beamline 5U.1 of the synchrotron radiation source (SRS). Here, (Ga,Mn)As and Al-doped (Ga,Mn)As samples were measured. The nominal Mn content of each sample was 6%. The samples were grown on GaAs buffer layers on GaAs(0 0 1) substrates. The details are shown in Table 3.2.

Sample	Real name	Treatment	Al content	Film thickness
E	Mn330	Annealed	0%	25 nm
F	Mn330	As-grown	0%	25 nm
G	Mn332	Annealed	10%	25 nm
H	Mn332	As-grown	10%	25 nm
I	Mn347	Annealed	20%	25 nm

Table 3.2: List of sample details for those measured at the SRS. Nominal Mn content was 6% for all these samples. Samples were grown on GaAs buffer layers on GaAs(0 0 1) substrates. Mn-doped layer thickness was 25 nm in all cases.

3.2.2 XMCD and XMLD measurements

The absorption spectra were measured in total-electron yield mode, at beamline 4.0.2 of the ALS. The measurements were performed at a range of temperatures, the lowest being 15 K. An eight-pole magnet [34] was used to magnetize the sample in any chosen direction.

For XMLD, x-ray absorption spectra were obtained by applying a magnetic field of 0.3 T along the different in-plane $\langle 1\,0\,0 \rangle$ or $\langle 1\,1\,0 \rangle$ crystalline axes, with x-rays at normal incidence to the (0 0 1) plane. This field size is sufficiently large to overcome any in-plane magnetic anisotropy barrier in the compressively strained (Ga,Mn)As films [35]. If the magnetic field is applied exactly in-plane, the emitted Auger electrons tend to be re-absorbed by the sample, giving a poor signal-to-noise ratio. Applying a small ($\sim$0.02 T) magnetic field component perpendicular to the sample plane permits the escape of the Auger electrons. This is not expected to significantly affect the magnetization direction, since the perpendicular direction — [0 0 1] — corresponds to the hard magnetic axis. The photon energy was scanned over the Mn $L_{2,3}$ absorption edges with the x-ray linear polarization **E** vertical and horizontal; the magnetization vector **M** was rotated in-plane by 90° at each point during the energy scan. This yielded two pairs of absorption spectra, with either $\mathbf{M} \parallel \mathbf{E}$ or $\mathbf{M} \perp \mathbf{E}$. Rotating either **M** or **E** resulted in identical XMLD spectra, within the experimental error: this ruled out non-magnetic contributions to the linear dichroism, such as charge anisotropy, or pinned antiferromagnetic moments with preferential orientation with respect to the crystalline axes. Therefore, the XMLD spectra obtained with horizontal and vertical polarization were averaged to improve the signal-to-noise ratio. Schematic diagrams of the experimental geometry are shown in insets to figure 3.3. From here onwards, the XMLD spectra with **E** parallel to the $\langle 1\,0\,0 \rangle$ and $\langle 1\,1\,0 \rangle$ axes are denoted as

$I_{\langle 1\,0\,0\rangle}$ and $I_{\langle 1\,1\,0\rangle}$, respectively.

For XMCD, absorption spectra are recorded with the x-ray helicity and sample magnetization parallel and antiparallel, usually normal to the sample plane. During measurements, the photon energy was scanned over the Mn L-edges with the photon helicity along the [0 0 1] axis, either parallel or antiparallel to the direction of the x-ray propagation. The magnetization **M** was flipped between parallel and antiparallel to the helicity at every point of the measurement, giving two pairs of absorption spectra with helicity parallel and antiparallel to **E**. Similar to the XMLD spectra, the XMCD difference spectra for each helicity were averaged. A larger magnetic field of 0.6 T is needed to saturate the [0 0 1] direction; in some cases measurements were taken in grazing incidence, with a magnetic field of 0.3 T applied in the sample plane.

Measurements of samples E to I (Table 3.2) at the SRS followed the same design as for the ALS experiments, with some minor differences. Here, the lowest temperature available was ∼25 K; only the $\langle 1\,1\,0\rangle$ axes were measured by XMLD. The POMS is of the same eight-pole design as that at the ALS.

3.2.3 SQUID measurements

Temperature-dependent measurements of the magnetization were made. Samples were cooled from room temperature to 2 K in an applied magnetic field of 0.3 T, and warmed back up to room temperature in remanence. For some samples, field-dependent magnetization loops were recorded at 15 K, to identify the easy and hard magnetic axes, and to determine the field required to saturate the sample.

3.2.4 Effect of etching

The effect of etching upon the magnetic moment of (Ga,Mn)As is shown in figure 3.1, using Mn339, a typical 25 nm layer of (Ga,Mn)As material with 6% Mn — note that this sample was not measured as part of the XMCD and XMLD study. The sample was annealed at 190°C for 24 hours. To etch the sample, it was placed in concentrated HCl for 10 s then rinsed in deionized water. In the figure, the root-mean-square (RMS) of the remanence along the in-plane axes ($\sqrt{{M_{[1\,1\,0]}}^2 + {M_{[1\,\bar{1}\,0]}}^2}$) are shown as a function of temperature.

Unfortunately these measurements were affected by trapped flux within the SQUID coils, which gives rise to the bumps in the magnetization curves at $T \approx 110$ and 125 K. There is a noise spike at $T \approx 40$, which was sometimes observed in the SQUID measurements. It is emphasized that these features are artefacts of the measurement, unrelated to the effect of etching, and affecting only the curve at these certain temperatures. The important regions of the curves to compare are towards zero temperature. There is a very small reduction in the magnetization upon etching, $\sim 3\%$ for as-grown and $\sim 2\%$ for annealed material. This corresponds to the removal of about 0.5 nm, roughly one monolayer.

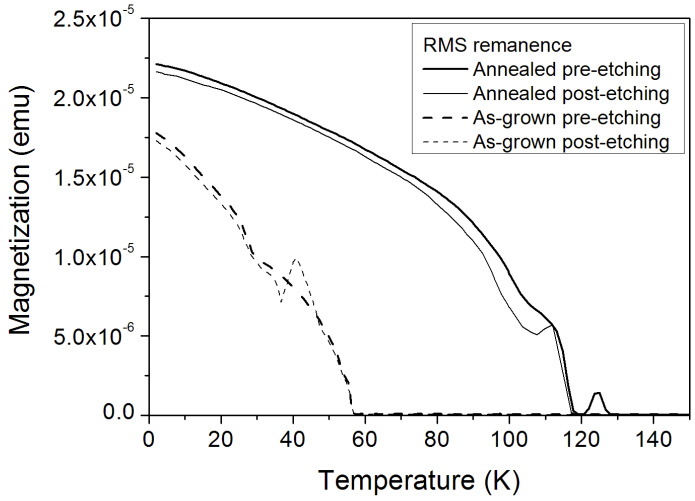

Figure 3.1: RMS remanent magnetization before (thick lines) and after etching (thin lines) for an annealed and an as-grown (Ga,Mn)As sample with 6% Mn, Mn339. The magnetization is not normalized to the amount of Mn within the samples.

The x-ray absorption spectrum demonstrates how the character of the Mn at the surface changes with etching (figure 3.2). Before the etch, the shape of the spectrum looks like atomic Mn d^5: the clear multiplet character at the L_3 region indicates a localized Mn d shell. This occurs because the Mn_I that has annealed out of the bulk oxidizes at the surface, forming a layer that is not commensurate with the rest of the semiconductor crystal lattice. Lacking itinerant carriers in this layer, the Mn d states become localized. Etching in HCl removes the surface oxide layer. The multiplet splitting becomes much weaker, and the spectrum is shifted ~ 0.5 eV lower in energy (the shift in the maximum peak is slightly

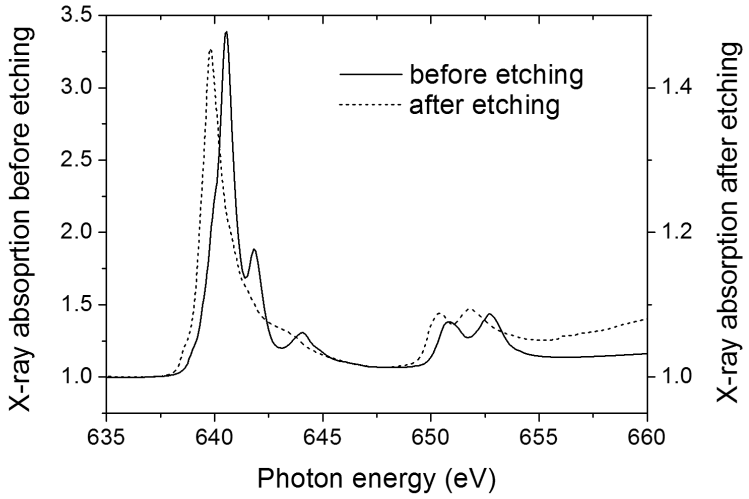

Figure 3.2: X-ray absorption spectra of the annealed (Ga,Mn)As sample Mn307 before (solid line) and after etching (dotted line).

larger, ~ 0.7 eV, due to a change in the weighting of the peaks making up the L_3 region). Both of these effects imply an increase in the screening by itinerant charge carriers. There is also a much larger absorption intensity before etching, because the surface is essentially coated in an Mn-rich layer. Note that the absorption intensity rises above the L_2 edge of the etched sample's spectrum because of a nonlinear background.

3.3 Anisotropic XMLD signal

3.3.1 Introduction

A significant XMLD signal may be expected from (Ga,Mn)As, because the local exchange interaction mediating with the GaAs valence band holes [19, 36] implies a somewhat localized Mn moment. In addition, epitaxial films of (Ga,Mn)As/GaAs(001) have a high degree of crystalline order, which results in large magnetocrystalline effects in magnetic and tunnelling properties [37, 38]. Here, it is shown that a large anisotropy is also observed in the XMLD spectra, which displays an entirely different lineshape for measurements along the $\langle 1\,0\,0\rangle$ and $\langle 1\,1\,0\rangle$ crystalline axes, revealing a rich structure that cannot be associated with the electronic band structure, but that can be explained by atomic multiplet calculations.

It is shown that the XMLD anisotropy can be regarded as a general feature arising from the restrictive dipole selection rules. The results of this section have been published [39].

3.3.2 Experimental results

Figure 3.3(a) shows the Mn $L_{2,3}$ absorption spectra for sample A. The insets depict the orientation of x-ray polarization (**E**) used, along the $\langle 1\,0\,0\rangle$ and $\langle 1\,1\,0\rangle$ axes. The black and red spectra are for parallel and perpendicular orientations of **E** and **M**, respectively. Along the $\langle 1\,0\,0\rangle$ axes, the largest L_3 absorption occurs for $\mathbf{M}\|\mathbf{E}$, while along the $\langle 1\,1\,0\rangle$ axes it is largest for $\mathbf{M}\perp\mathbf{E}$. The difference in absorption peak intensity between $\mathbf{M}\|\mathbf{E}$ and $\mathbf{M}\perp\mathbf{E}$ is ∼12%. This is much larger than normally found for metallic ferromagnets, which typically show a ∼2% change in the Fe or Co L_3 absorption, and ∼1% change in the Cr L_3 absorption peak intensity [15–17]. The XMLD signal is thought to scale roughly with the ground-state spin moment, multiplied by the final-state exchange interaction [40, 41]. The local magnetic moment of a Mn^{2+} ion is around twice that of metallic Fe, so an XMLD signal four times as large would be expected from considering the magnitude of the local moment alone. Additionally, the localization of the moment plays a part in the size of the XMLD, because the presence of free carriers screens the final-state exchange interaction. Indeed, the XMLD is very large (>10%) in localized antiferromagnetic systems with a strong 2*p*-3*d* exchange interaction, such as Fe_2O_3 [9], $LaFeO_3$ [11, 13] and NiO [10]. Therefore, the large XMLD signal measured for ferromagnetic (Ga,Mn)As suggests that the Mn moment is both large and significantly localized.

The XMLD spectrum exhibits a very large anisotropy with rotation of the x-ray polarization from $\langle 1\,0\,0\rangle$ to $\langle 1\,1\,0\rangle$, as shown in figure 3.3(b). The strongest peak is opposite in sign for the two axes, though the two spectra are not simply a reversal of one another. As can be seen from figure 3.3(b), the structure is substantially different for the two orientations. At the L_3 edge, the size of the XMLD is larger along $\langle 1\,1\,0\rangle$ than $\langle 1\,0\,0\rangle$; this is most likely because of the additional peaks for $\langle 1\,0\,0\rangle$, which may curb the principal peak by broadening and overlapping of intensity. The XMLD at the L_2 edge lacks such complexity, and consequently its intensity is about the same for $\langle 1\,1\,0\rangle$ and $\langle 1\,0\,0\rangle$.

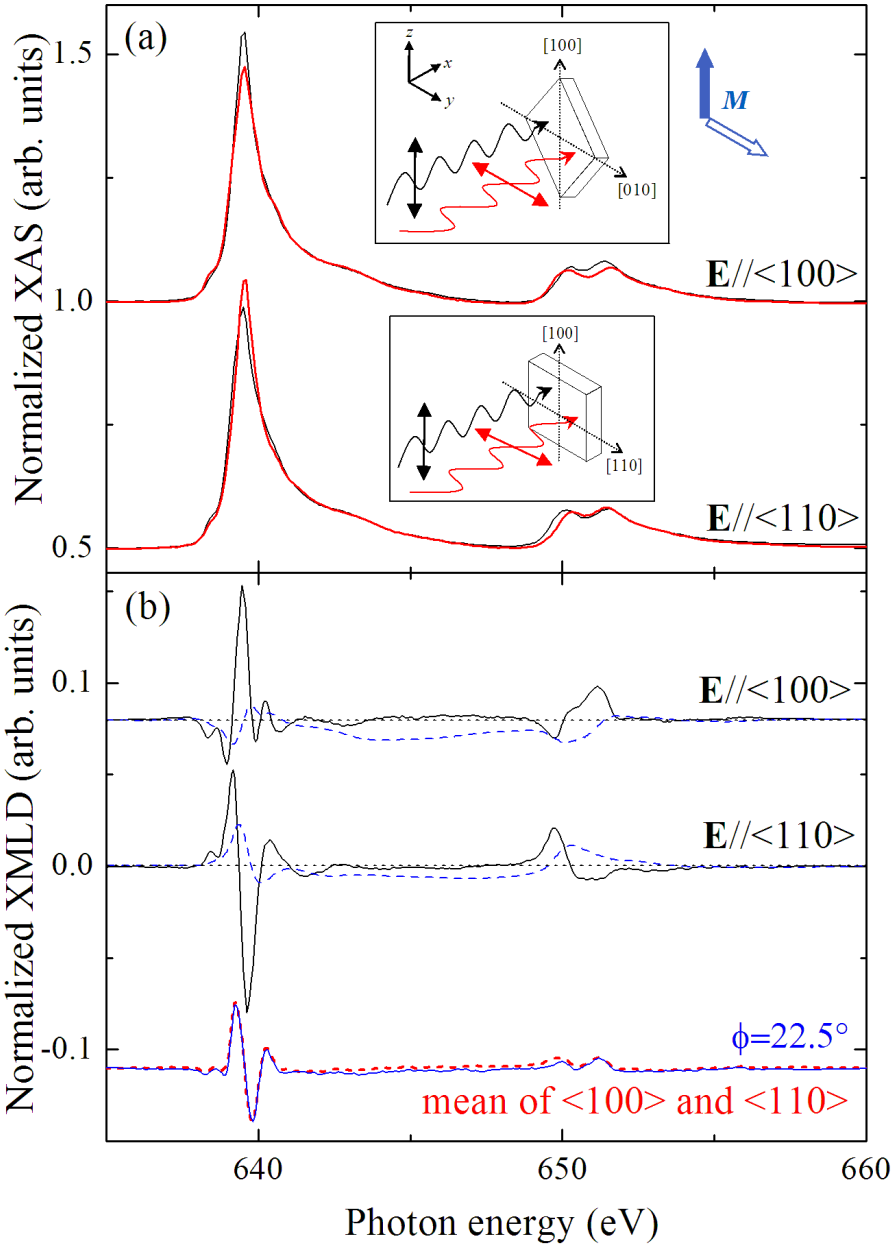

Figure 3.3: Mn $L_{2,3}$ absorption and XMLD spectra from sample A, at $T = 15$ K. (a) XAS for $\mathbf{E} \parallel \mathbf{M}$ (thin black line) and $\mathbf{M} \perp \mathbf{E}$ (thick red line), for $\mathbf{E}$ along $\langle 1\,0\,0 \rangle$ and $\langle 1\,1\,0 \rangle$. Experimental geometry is depicted next to the relevant spectra. (b) The resulting XMLD spectra (black solid) and integrated spectra (blue dotted), $(\mathbf{M} \parallel \mathbf{E}) - (\mathbf{M} \perp \mathbf{E})$, for $\mathbf{E}$ along $\langle 1\,0\,0 \rangle$ and $\langle 1\,1\,0 \rangle$ with their integrated spectra. The XMLD for $\mathbf{E}$ at $\phi = 22.5°$ from the $[1\,0\,0]$ axis in the $(0\,0\,1)$ plane (blue solid) is overlaid with the mean of the XMLD spectra along $\langle 1\,1\,0 \rangle$ and $\langle 1\,0\,0 \rangle$ (red dotted). Vertical offsets are for clarity.

3.3.3 Comparison with calculation

The large anisotropy was theoretically predicted by Kuneš and Oppeneer [41] for cubic Fe, Co, and Ni metal. The authors used two approaches: *ab initio* band structure calculations, and single-particle model calculations in which the $3d$ spin-orbit interaction is neglected, and the $2p$ exchange splitting is used as an input parameter. The model matches the full calculations well (except in the case of Ni, where the effect of the final-state spin-orbit coupling is shown to have a significant contribution to the XMLD); both approaches give an XMLD spectrum showing smooth features consisting of a positive and negative lobe for each absorption edge. However, the Mn $L_{2,3}$ XMLD spectra of (Ga,Mn)As show a much more complicated structure, owing to an exchange interaction that is less screened by free carriers. Consequently its simulation requires a many-electron approach, *e.g.* a multiplet calculation, in which the role of the effective exchange splitting is replaced by the $2p$-$3d$ Coulomb and exchange interactions [42]. The anisotropy arises from the rotation of the spin direction with respect to the crystal field axes, which breaks the spherical symmetry.

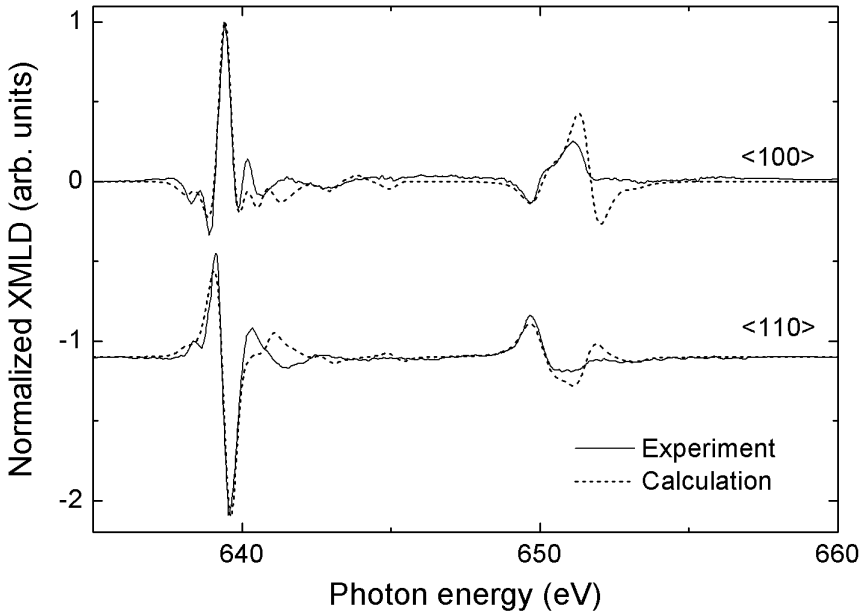

Figure 3.4: The Mn $L_{2,3}$ XMLD spectra $I_{\langle 1\,0\,0\rangle}$ and $I_{\langle 1\,1\,0\rangle}$, where the experimental spectra (solid line) are compared to multiplet calculations (dashes) for a d^5 configuration in a cubic crystal field. The spectra are normalized at the peak maximum.

Figure 3.4 shows the calculated XMLD for a Mn d^5 configuration in a tetrahedral crystal field (where the splitting between the t_2 and e states is $10Dq = -0.5$ eV). The calculated spectra were provided by G. van der Laan [43]. The same crystal field splitting has been used to give an excellent agreement with XMCD spectra [44]. The calculation reproduces the main features of the XMLD spectra for the $\langle 1\,0\,0\rangle$ and $\langle 1\,1\,0\rangle$ axes. The main difference with the experimental spectra is found in the region just above the main structures of the L_3 and L_2 edges. This is ascribed to the influence of other configurations in the mixed ground state, containing configurations other than d^5. The value of the crystal field parameter used for the calculation means that the e states have a lower energy than the t_2 states, as expected for tetrahedral symmetry. The t_2 orbitals are directed toward the As neighbours, giving them a higher electrostatic repulsion energy than the non-bonding e orbitals. The sign and magnitude of the splitting is consistent with *ab initio* calculations of the unfilled Mn $3d$ states in (Ga,Mn)As [45].

3.3.4 Interpretation

The integrated XMLD spectra* are shown in figure 3.3(b), and allow the determination of the anisotropic spin-orbit interaction (see Chapter 2). Recall that the anisotropic spin-orbit interaction is directly related to the MAE [14]. Since the integrated XMLD over each edge is close to zero, the large anisotropy of the XMLD, observed when the sample is rotated with respect to **M** and **E**, does not imply a large MAE of the Mn d states. Rather, the anisotropic XMLD is due to the restriction (by electric-dipole selection rules) of the set of final states that can be reached from the ground state.

While the absorption spectrum with **M** and **E** along the crystal field axis is given by the selection rule $\Delta m = 0$, for other directions the $\Delta m = \pm 1$ transitions become allowed, where m is the magnetic quantum number. This leads to a strong angular dependence in the case that the d states are split by a non-spherical interaction, *i.e.* a crystal field. This occurs even for a half-filled d shell with a fully symmetrical charge distribution when the degeneracy of the e and t_2 states is lifted, as is clearly demonstrated by the calcula-

*The integrated XMLD spectra are obtained by careful adjustment of the absorption spectra for $\mathbf{M} \parallel \mathbf{E}$ and $\mathbf{M} \perp \mathbf{E}$, so that their respective integrated absorption spectra are equal after the L_2 edge, before taking their difference. This ensures that the XMLD after the L_2 edge is zero and flat.

tions for Mn d^5. The strong angular dependence in the XMLD is therefore a property of the wavefunctions for the d states and not caused by the charge quadrupole moment or magnetocrystalline anisotropy.

Further evidence is provided by the measured azimuthal angular dependence. For **M** and **E** at an angle ϕ with respect to the [1 0 0] axis in the (0 0 1) plane, the calculated XMLD spectrum can be written as a linear combination of two independent XMLD spectra,

$$I(\phi) = \frac{1}{2}\left[I_{\langle 1\,0\,0\rangle} + I_{\langle 1\,1\,0\rangle} + (I_{\langle 1\,0\,0\rangle} - I_{\langle 1\,1\,0\rangle})\cos 4\phi\right]. \tag{3.1}$$

Thus the dependence is given by an isotropic term together with a $\cos 4\phi$ term arising from the 4-fold symmetry of the (0 0 1) plane. To corroborate the angle-dependence, figure 3.3 shows the measured XMLD spectrum obtained at $\phi = 22.5°$, *i.e.* halfway between both symmetry axes. The XMLD spectrum obtained along this direction is indistinguishable from the mean of the measured spectra $I_{\langle 1\,0\,0\rangle}$ and $I_{\langle 1\,1\,0\rangle}$, also shown in figure 3.3(b). The angular dependent part in Equation 3.1 vanishes in the absence of a crystal field, since $I_{\langle 1\,0\,0\rangle} = I_{\langle 1\,1\,0\rangle}$ for $10Dq = 0$. Furthermore, when the $3d$ spin-orbit parameter is set to zero in the calculation, the angular dependence due to the crystal field remains, which demonstrates that the origin of this dependence is not due to the MAE.

In summary, for the ferromagnetic semiconductor (Ga,Mn)As, a Mn $L_{2,3}$ XMLD was observed that is much larger than typically found in metallic ferromagnets. This can be seen as experimental evidence for a localized Mn moment. Furthermore, a strong anisotropy of the XMLD was demonstrated on rotation of the magnetization and polarization vectors with respect to the crystalline axes. This result is reproduced by Mn d^5 atomic multiplet calculations. Since these calculations take no account of the detailed local density of states of Mn in GaAs, the XMLD anisotropy should be generic for localized moment systems, and should be considered in future studies of crystalline ferro- or antiferromagnetic materials using polarization-dependent x-ray absorption.

The anisotropic XMLD of antiferromagnetic transition-metal systems has been investigated in more recent studies than this one. The Fe L-edges in Fe_3O_4 [46] and the L-edges of Ni^2+ in cubic lattices [47] have been studied in various geometries, and similarly the

findings are that the XMLD is composed of two fundamental spectra. The theoretical treatment for cubic symmetry therein is expanded to the more general case of tetragonal symmetry [48].

3.4 Magnetization deficit in as-grown (Ga,Mn)As

The apparent 'magnetization deficit' observed in as-grown (Ga,Mn)As material has previously been studied by SQUID magnetometry [31] and XMCD [1, 7], but not yet using XMLD. This investigation now makes use of all three of these techniques, to make some interpretations about the magnetization deficit, specifically in terms of the behaviour of Mn_I.

3.4.1 Estimation of Mn_I content by comparing XMCD and SQUID data

Figure 3.5 (a) and (b) compares data for as-grown and annealed samples from two separate experiments (see Table 3.1 for details), measured by SQUID and XMCD. The temperature-dependant magnetization curves, $M(T)$, are plotted along with the magnetic moment per Mn calculated by XMCD sum rules. The sample substrates contribute a negative diamagnetic signal, which has been subtracted as a constant offset to give the magnetization curves in the figure. $M(T)$ for the annealed samples follows the shape of a Brillouin function, with a small increase continuing at very low temperatures. The shape of $M(T)$ curve of as-grown films strongly deviates from the shape expected by mean field theory [49], exhibiting a roughly linear increase below T_C. The small kink feature visible at $T \sim 50\ K$ for samples C and D in figure 3.5 (b) is unlikely to be intrinsic to the sample, and could correspond to an antiferromagnetic transition of some Mn_xO_y remaining on the surface. Sample C was measured with an applied field of 1 kOe, rather than 3 kOe used for the other magnetization curves; this was done because of problems with using the SQUID for higher applied magnetic fields. The hysteresis loop for this sample at 15 K is shown in the inset to figure 3.5(b): although the measurement does not go up to 3 kOe, it is clear that the sample is very close to saturation by 1 kOe. The magnetization curves in remanence (not shown) show that there is negligible second phase in the material, exhibiting a single

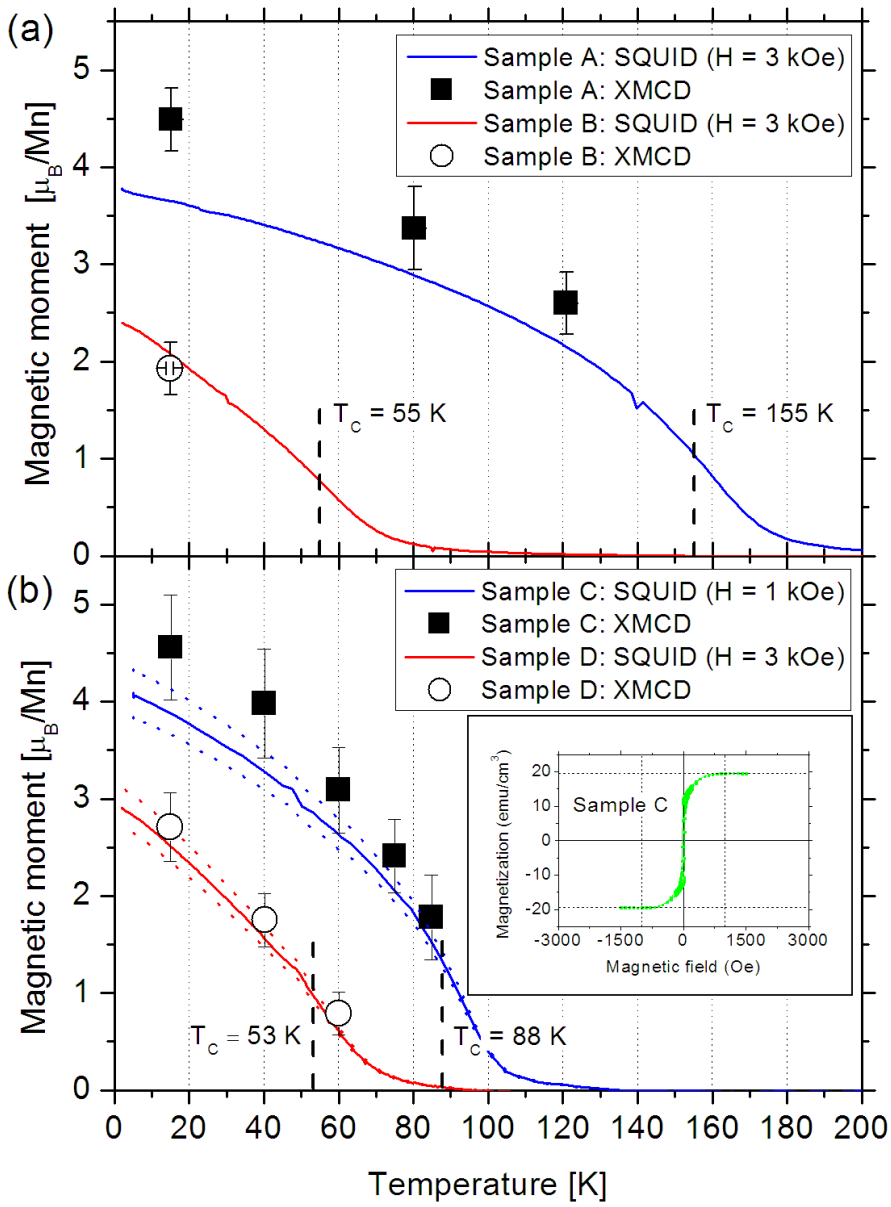

Figure 3.5: $M(T)$ of (Ga,Mn)As samples measured by SQUID and magnetic moment per Mn calculated by XMCD sum rules. (a) annealed sample A ($x = 0.07$) and as-grown sample B ($x = 0.075$); (b) annealed sample C and as-grown sample D (both $x = 0.03$). Dotted curves represent the bounds of the error in this measurement, estimated from the errors in volume of the sample and the nominal Mn content. Inset: Hysteresis curve for sample C.

clear ferromagnetic transition temperature.

For the as-grown material, the moments per Mn measured by SQUID are in agreement with those measured by XMCD sum rules. In the annealed samples, however, there is a clear difference in moment per Mn, corresponding to the amount of Mn lost during annealing. It is possible to estimate the amount of Mn lost during annealing, f_{lost}, using the moments measured at 15 K by XMCD sum rules (denoted M_{XMCD}) and SQUID (M_{SQUID}) shown on figure 3.5. The magnetic moments calculated from SQUID measurements are underestimates, because they do not take into account the quantity of Mn lost during annealing, and are normalized to the nominal Mn concentration at growth. The XMCD, on the other hand, is automatically normalized to the actual Mn content (provided that the saturation effect is negligible for the measurement). It can be said that: $M_{\text{SQUID}} = M_{\text{XMCD}}(1 - f_{\text{lost}})$. The calculated proportion of Mn_I lost during the annealing of samples A and C are displayed in Table 3.3. Although the errors are indeed large, the values agree quite well with previous estimations of partial concentration of Mn_I [29, 31], and implies the interstitial concentration is greater in as-grown samples with a high Mn content.

Sample	M_{XMCD} (μ_B/Mn)	M_{SQUID}(μ_B/Mn)	f_{lost}
A	4.46 ± 0.3	3.65 ± 0.2	0.18 ± 0.07
C	4.56 ± 0.54	3.88 ± 0.23	0.15 ± 0.11

Table 3.3: Table of measured magnetic moments and the calculated fraction of Mn lost by annealing. Measurements taken at $T = 15$ K.

3.4.2 Effect of annealing upon XMLD intensity

The effect of annealing and etching (Ga,Mn)As samples prior to measurement has been shown to lead to dramatic increases of T_C [33, 50], hole concentration [31, 50] and magnetic moment per Mn [7]. It is thought that these enhancements come about when antiferromagnetically coupled Mn_Ga-Mn_I pairs are broken and the Mn_I diffuse to the surface where they oxidize and are removed from the sample by the etching process. The effect of etching alone is to remove the Mn oxide-rich surface layer, which is the reason that the x-ray absorption spectra exhibit a change in the Mn ground state from a localized d^5 to a hybridized ground-state after annealing [3]. Changes in the fine structure of the XMCD spectrum

have also been identified on annealing, which show a systematic dependence on the carrier concentration [44], with a uniaxial anisotropy determined by the epitaxial strain [51]; this indicates that these Mn $3d$ states take on the character of the hybridized holes. The effect of annealing on the XMLD signal, which measures both ferro- and antiferromagnetic order, has not yet been investigated. This section includes XMCD and XMLD results from more than one synchrotron experiment.

As mentioned in section 3.3, the XMLD intensity scales roughly with the product of the ground-state spin moment and the final-state exchange interaction [40, 41]. It is not immediately clear which of these contributes the majority of the XMLD magnitude. The effect of annealing on the lineshapes and intensity are compared in the following figures.

To compare the lineshapes (ignoring the effect of the size of the magnetic moment upon the XMLD intensity), the XMLD spectra of samples A to D along $\langle 1\,0\,0\rangle$ and $\langle 1\,1\,0\rangle$ were scaled so that their strongest peaks are unity, shown in figure 3.6. Linear backgrounds were subtracted from the spectra to overlay the $L_{2,3}$ regions as best as possible, though at the extrema they tend to diverge because of the small signal of the low Mn content samples. For $\mathbf{E} \parallel \langle 1\,1\,0\rangle$, the spectra match reasonably well; the differences are not well-pronounced, and barely above the noise level. For $\mathbf{E} \parallel \langle 1\,0\,0\rangle$, where the L_3 XMLD contains more and narrower features, the negative peaks at ~ 638.9 and 639.8 eV seem to become stronger and sharper in the lower Mn content and as-grown material. Annealing and a high Mn concentration evidently suppresses these features, probably because a higher hole concentration screens the final-state exchange interaction, broadening the spectra. Accordingly, this suggests a slightly more localized moment in the low Mn content and as-grown samples because of a lower hole concentration.

To compare the XMLD intensity, the normalized XMLD spectra of three as-grown and three annealed samples are shown in figure 3.7, measured along the $\langle 1\,0\,0\rangle$ and $\langle 1\,1\,0\rangle$ axes (the results in this figure are only used for qualitative comparison, because they were obtained in different experiments). There is a striking increase in the intensity of the XMLD after annealing. The corresponding XMCD intensity increases on annealing as expected, shown in figure 3.8. If the as-grown samples had long-range antiferromagnetic order (as depicted by 'Scenario III' in figure 3.11), their XMLD would be of similar intensity to

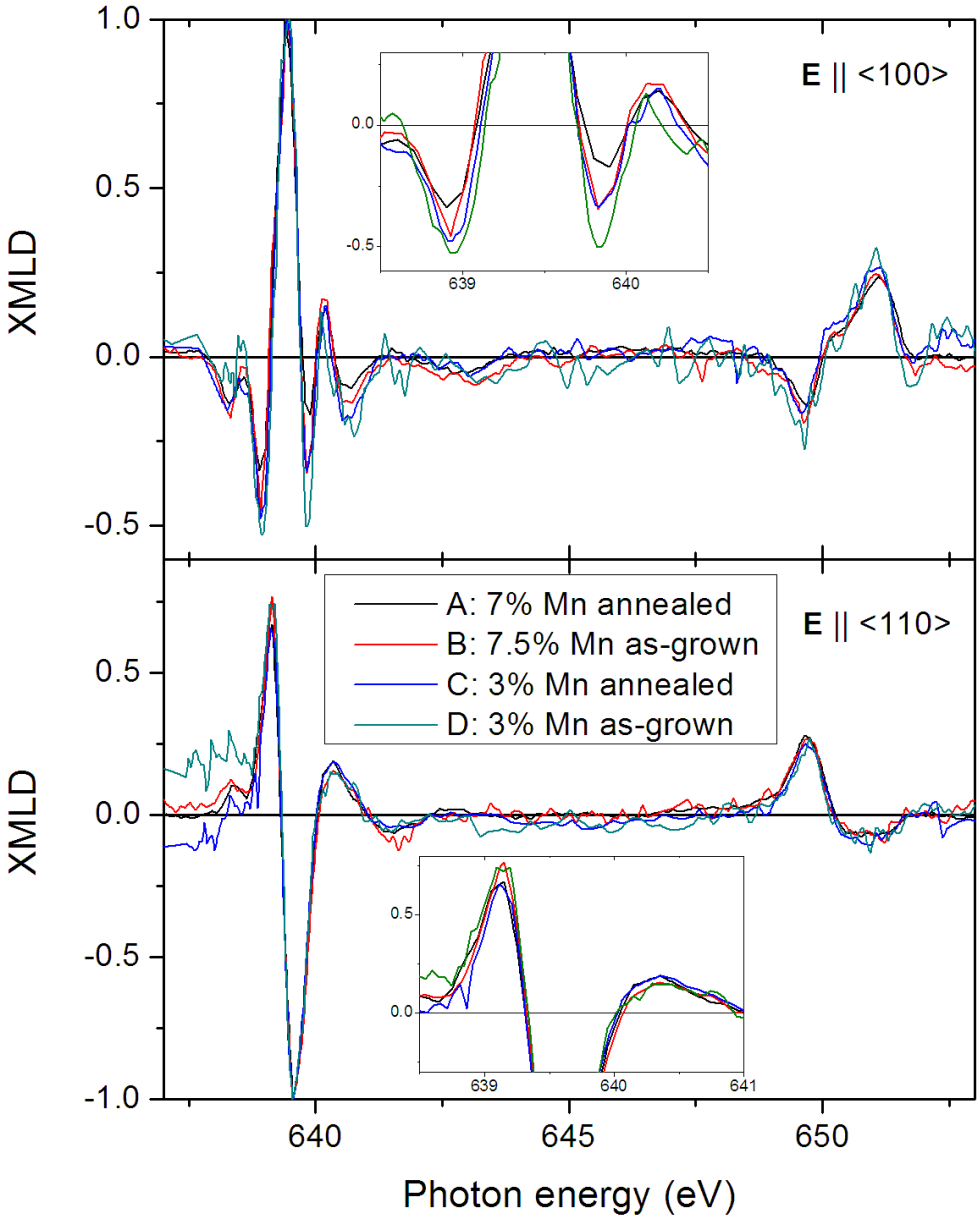

Figure 3.6: XMLD spectra with the strongest peak normalized to unity, for annealed samples with $x = 0.07$ and 0.03 (A and C) and as-grown samples with 0.075 and 0.03 (B and D). Top: $\mathbf{E} \parallel \langle 1\,0\,0 \rangle$; bottom: $\mathbf{E} \parallel \langle 1\,0\,0 \rangle$. Insets expand the L_3 region to clarify the differences in the spectra.

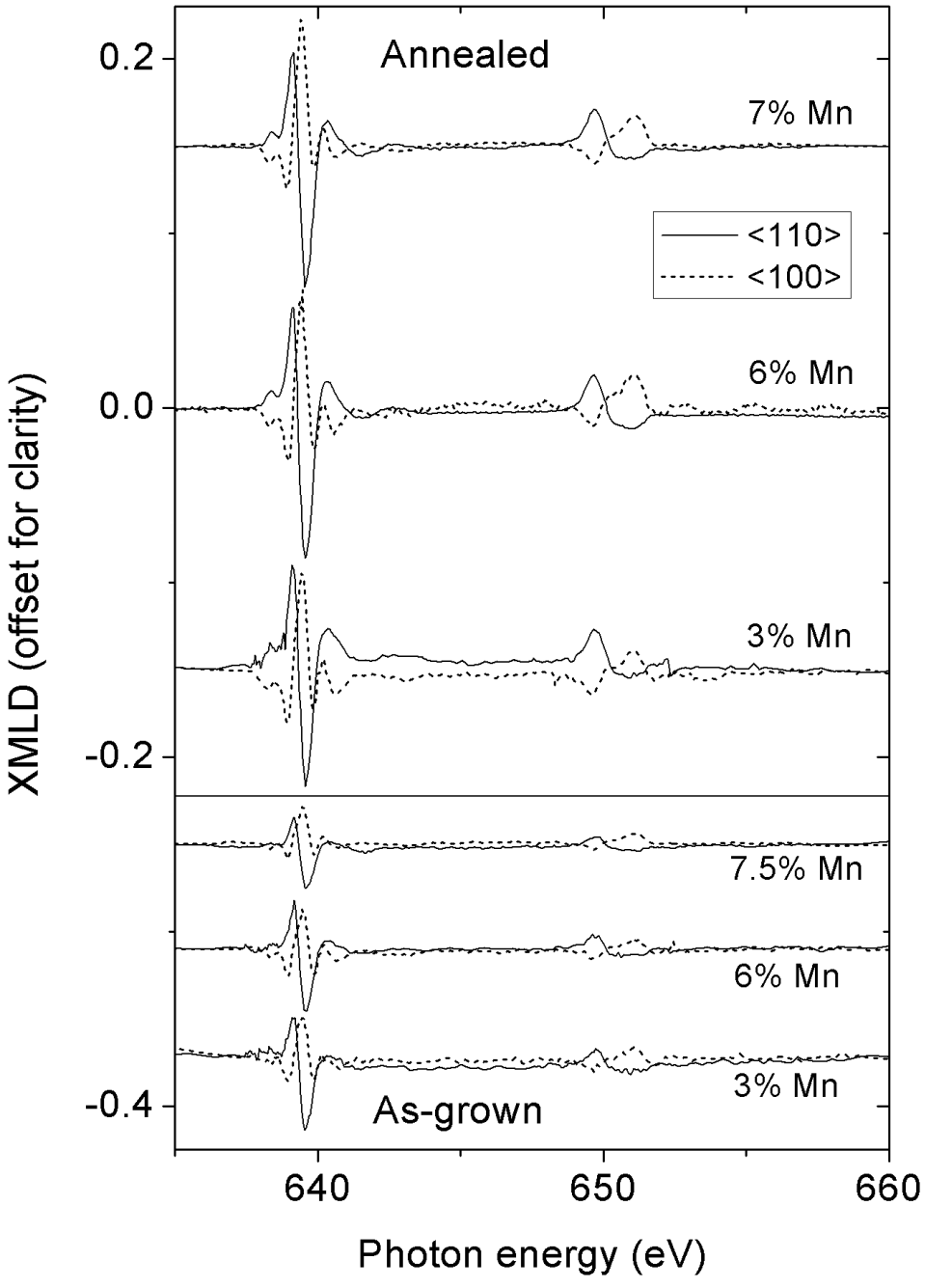

Figure 3.7: From top to bottom: XMLD along $\langle 1\,1\,0 \rangle$ (solid lines) and $\langle 1\,0\,0 \rangle$ (dotted lines) of annealed samples with $x = 0.07$, 0.06, 0.03, and as-grown samples with $x = 0.075$, 0.06, 0.03. The measurements were made at 15 K. The spectra were normalized to the L_3 x-ray absorption peak.

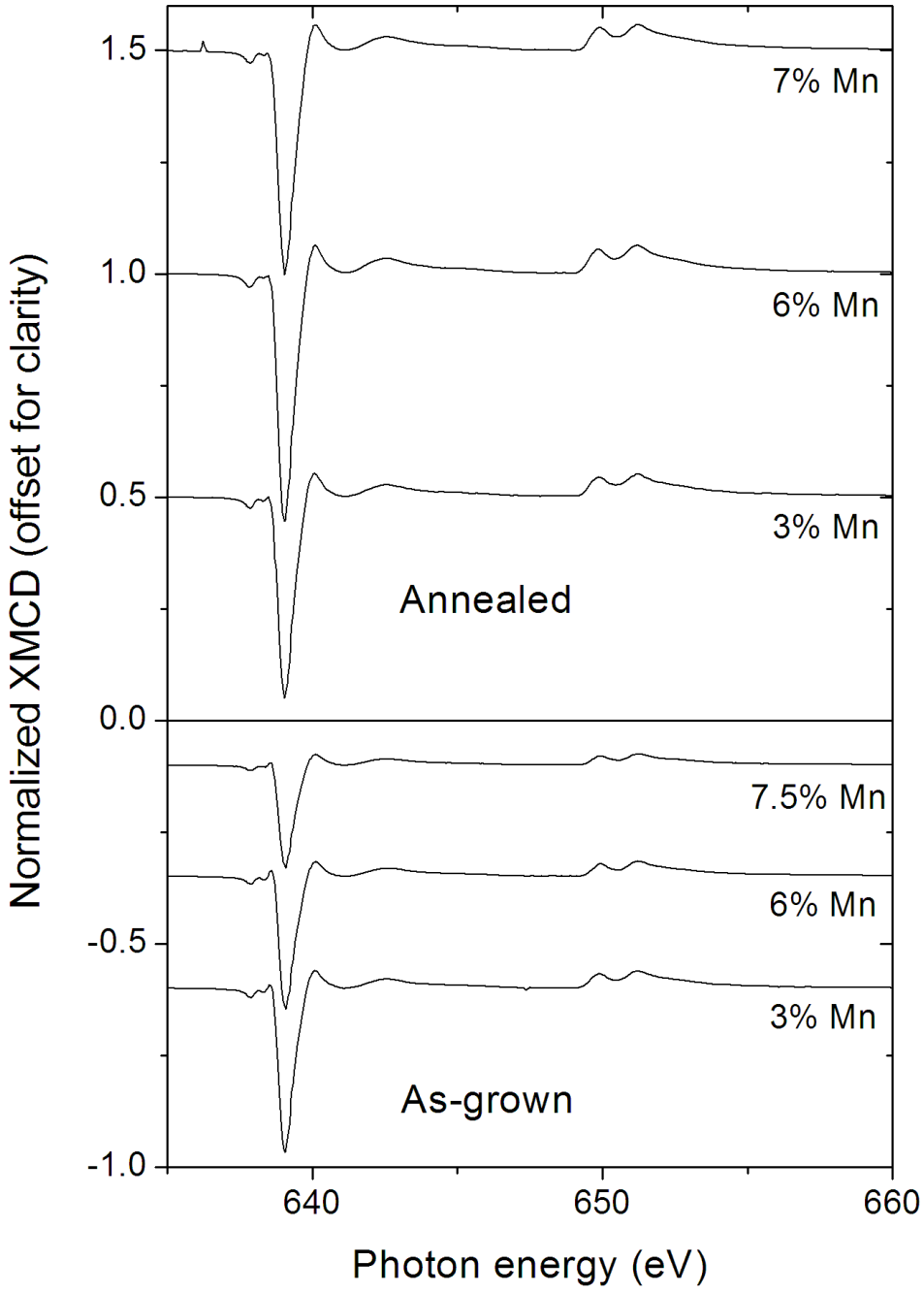

Figure 3.8: From top to bottom: XMCD of annealed samples at normal incidence with x = 0.07, 0.06, 0.03, and as-grown samples with x = 0.075, 0.06, 0.03. The measurements were made at 15 K. The spectra were normalized to the L_3 x-ray absorption peak.

the annealed samples, with a smaller XMCD. Instead, the reduced XMLD signal observed in as-grown material indicates that some of the Mn is not behaving magnetically. Two possible explanations for why some Mn spins are not aligned to the global magnetization axis are (i) either the Mn_I atoms themselves are magnetically disordered and effectively have a local magnetic moment of zero, or (ii) the interstitial and substitutional Mn form antiferromagnetically-coupled pairs with a disordered spin axis. These are depicted in Scenarios I and II of figure 3.11, respectively.

We can investigate the possibilities now by comparing the XMLD and XMCD intensities of each sample. Recall that the XMCD scales with the average local magnetic moment $\langle \mathbf{M} \rangle$, while the XMLD is proportional to $\langle \mathbf{M}^2 \rangle$, and that both measurements are normalized to the total Mn content. If the size of the local moment is reduced, then the intensity of the XMLD should scale with the square of the XMCD; a reduction in the *number* of ferromagnetically active moments would cause the two measurements to follow a linear, rather than quadratic relationship. In the following figures, the intensity of the XMCD is measured from peak-to-peak of the L_3 region, and denoted I_{XMCD}. The L_3 region of the XMLD consists of a sharp positive and negative peak in close proximity, making it prone to overlapping of intensity which could significantly curb the peak-to-peak signal. The L_2 region is intrinsically broader and therefore less susceptible to such a problem. Henceforth the peak-to-peak XMLD intensity of the L_2 region is denoted I_{XMLD}.

In figure 3.9, I_{XMLD} is plotted against ${I_{XMCD}}^2$ for as-grown and annealed samples at (a) high and (b) lower Mn concentration[†]. XMLD data from the $\langle 1\,1\,0 \rangle$ and $\langle 1\,0\,0 \rangle$ axes are shown. The linear fits are extrapolated to zero. There is strong temperature dependence, which arises from a reduction of the local moment due to increasing thermal disorder and fits the predicted relationship well. The XMCD in figure 3.9(a) was taken at normal incidence, while figure 3.9(b) contains data recorded in both normal and grazing incidence. The helicity of the x-rays was accounted for in the XMCD data: 96% for the former experiment; 81% in the latter. The gradient of the linear fit is steeper in figure 3.9(a) than for 3.9(b).

[†]The high and low concentration samples were measured in two different experiments. It is not appropriate to compare them on the same axes because of the different experimental conditions, evidenced by the different gradients.

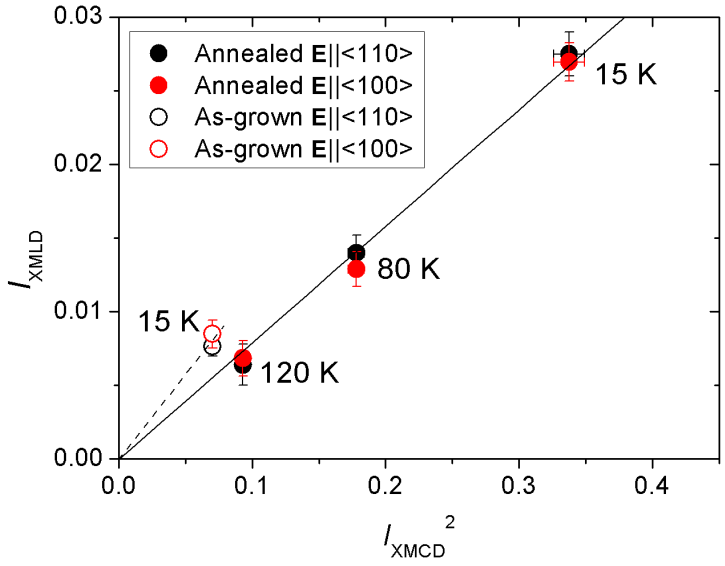

(a) 7.5% Mn as-grown sample measured at 15 K, and a 7% Mn annealed sample at 15, 80 and 120 K. Measured in at the ALS in October 2004.

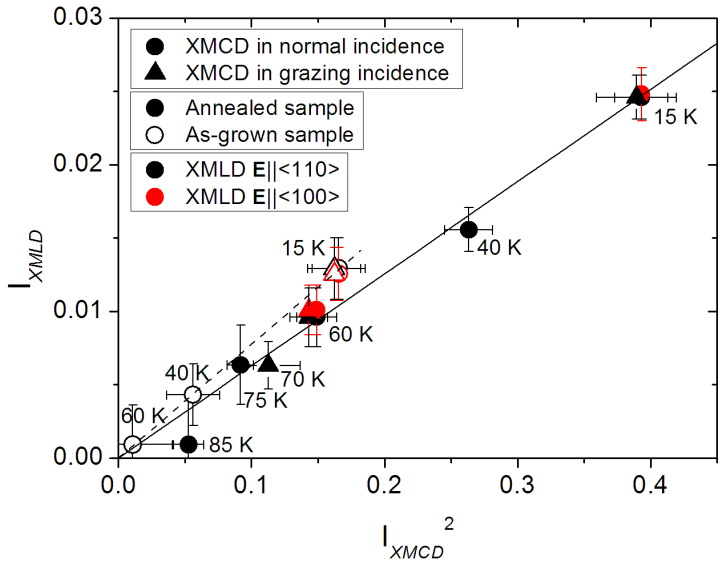

(b) 6% Mn as-grown sample measured at 15 K, and a 3% Mn as-grown and annealed samples measured at a range of temperatures. From the ALS in March 2005.

Figure 3.9: Peak-to-peak intensity of XMLD against that of the XMCD squared, measured at the L_2 and L_3 edges, respectively. The symbols indicate: XMLD data measured along $\langle 1\,1\,0 \rangle$ (black) and $\langle 1\,0\,0 \rangle$ (red); XMCD data measured in normal (circles) or grazing incidence (triangles); annealed (closed) and as-grown samples (open).

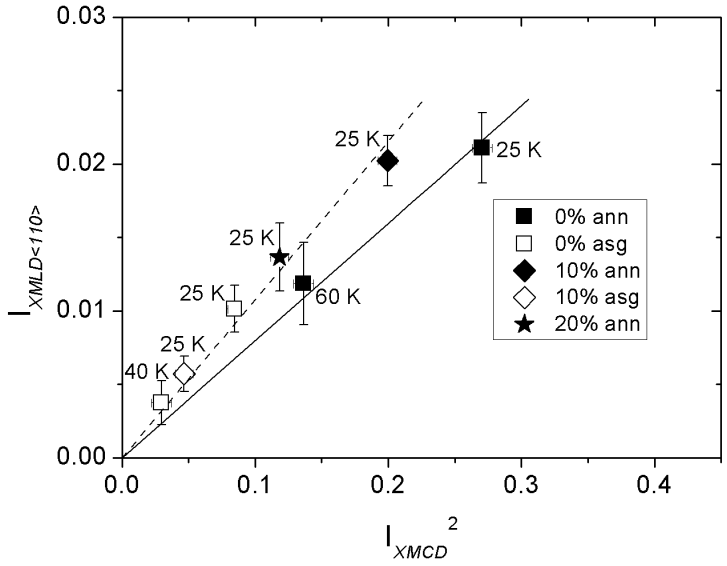

Figure 3.10: Peak-to-peak XMLD against that of XMCD squared, for the L_2 and L_3 edges respectively. XMLD data measured only along the $\langle 1\,1\,0 \rangle$ axes. The samples were as-grown and annealed (Ga,Mn)As and (Al,Ga,Mn)As samples, all with 5% Mn and 10% or 20% Al (nominal concentrations). Full line is fitted to annealed 0% Al sample at 25 and 60 K; dotted line is fitted to all other points. From the SRS in September 2006.

The as-grown data follow a quadratic dependence of XMCD and XMLD on increasing temperature. However, the steeper gradient of the linear fit to the as-grown data suggests that the effect of annealing is to increase the XMCD and XMLD in something closer to a linear relationship, suggesting that they may harbour some magnetically inactive Mn. The presence of non-magnetic (or *magnetically disordered*) Mn would contribute to the total absorption, but not to the XMCD or XMLD intensity, thus reducing I_{XMLD} and I_{XMCD} in linear proportion.

Figure 3.10 shows similar data measured in a third experiment, at the SRS. The samples here were as-grown and annealed (Ga,Mn)As and (Al,Ga,Mn)As samples with 5% Mn, and 10% or 20% Al nominal content. Fits are made to the annealed (Ga,Mn)As sample data at 25 K and 60 K (presuming no compensation), and to the data from all the other samples (which suffer a magnetization deficit). In both cases the fits are extrapolated to zero. In the 'compensated' samples — the as-grown samples and those containing Al — the magnetization deficit is not due to a suppression in $\langle M \rangle$, but rather a reduction

in the number of ferromagnetic Mn, which is brought about by the presence of Mn_I and formation of Mn_{Ga}-Mn_I pairs. This is interesting because it suggests that the presence of Al inhibits the out-diffusion of the Mn interstitials. The fractions of Mn in substitutional, interstitial and random sites are estimated from channelling particle-induced x-ray emission (c-PIXE) measurements of as-grown and annealed (Al,Ga,Mn)As in Ref. [52]. The results support the picture that the presence of Al increases the stability of the Mn_I atoms. Above concentrations of 50% Al, annealing is ineffective at removing Mn_I. For lower Al concentrations, a substantial amount of Mn_I is removed by annealing. However, differences in samples, annealing conditions and the error associated with c-PIXE measurements mean that a quantitative comparison with those of the present study is not reliable.

I_{XMLD} is the same for the different crystalline axes, within experimental error. This indicates that the applied magnetic field produces negligible torque on the spin axis of the Mn_{Ga}-Mn_I pairs, implying they can be considered as disordered, 'spin-zero' entities. This establishes the case for non-magnetic Mn being the source of the magnetization deficit in as-grown material. This idea will now be developed in the discussion, using a quantitative analysis to ascertain the quantity of non-magnetic Mn, and whether this is the sole source of magnetization suppression in as-grown (Ga,Mn)As.

3.5 Discussion: Does the local magnetic moment vary?

The presence of 'non-magnetic' Mn may not be the only cause of magnetization suppression in (Ga,Mn)As. Alternative mechanisms were mentioned in the introduction, and the magnetization of holes is thought to play a small part. A reduction in the size of the Mn average local magnetic moment itself may be brought about by mechanisms inducing non-collinearity. It is possible that both Mn_{Ga}-Mn_I pairs *and* a non-collinear local moment contribute to the deficit, a situation which is not easily identifiable from plotting I_{XMLD} against ${I_{XMCD}}^2$. In this discussion, a quantitative analysis of our combined SQUID, XMCD and XMLD data is used in an attempt to separate the signals from ferromagnetic and magnetically inactive Mn. Their relative proportions in as-grown (Ga,Mn)As are estimated, and compared with the proportion of Mn_I lost by annealing, found earlier

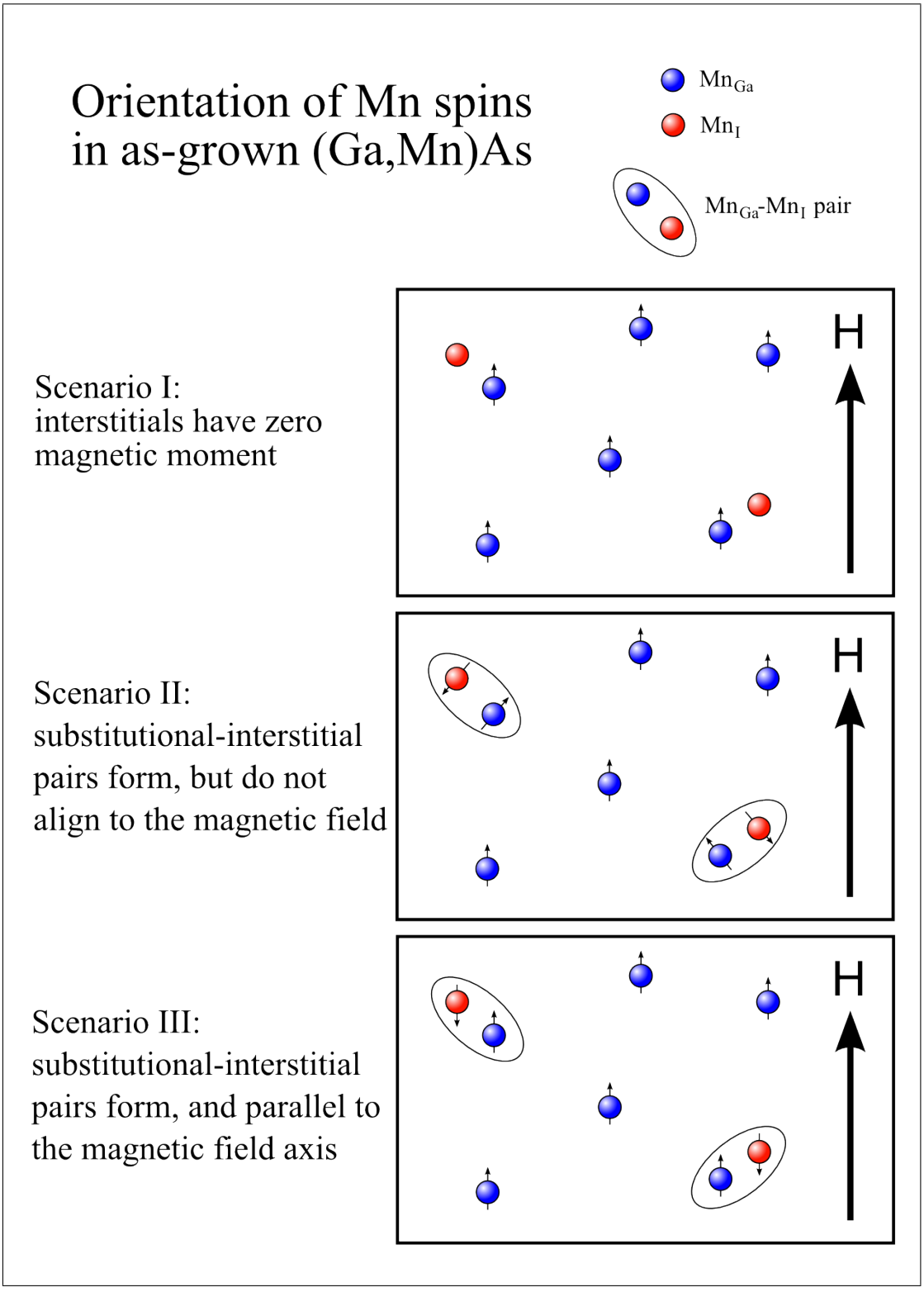

Figure 3.11: Three possible scenarios describing the behaviour of Mn_{Ga} and Mn_I. In Scenario I, Mn_{Ga} are ferromagnetic and Mn_I are non-magnetic; in Scenario II, Mn_{Ga}-Mn_I pairs form but have preferential ordering axis and are effectively non-magnetic; in Scenario III, the axis of the pairs aligns parallel to the external magnetic field.

in Section 3.4.1.

The XMCD peak-to-peak L_3 asymmetry, I_{XMCD}, can be thought of as proportional to the average magnetic moment μ. Similarly, $I_{XMLD} \propto \mu^2$. The XMCD also scales with the concentration of Mn moments aligned parallel to the global magnetization, x_p, but is reduced by those aligned antiparallel, x_a. Both x_p and x_a add to the intensity of the XMLD signal. The signal intensity of both techniques is normalized to the total Mn concentration in the sample: $x_T = x_S + x_I$ for as-grown samples, and $x_T = x_S$ for annealed samples.

Henceforth, I_{XMCD} and I_{XMLD} are called C and L for brevity, and for as-grown material may be expressed as:

$$C_U = \alpha \frac{(x_p - x_a)}{x_S + x_I} \mu_U(T) \tag{3.2}$$

$$L_U = \beta \frac{(x_p + x_a)}{x_S + x_I} {\mu_U}^2(T) \tag{3.3}$$

where the subscript 'U' indicates values relating to the as-grown [Untreated] material, and α and β are constants of proportionality, assumed to be the same for all the (Ga,Mn)As samples studied under the same experimental conditions.

It has been shown that $\mathrm{Mn_I}$ are removed by annealing [50], and that the remaining Mn are ferromagnetically aligned [7]. Hence, in annealed material $x_I = 0$, $x_a = 0$ and $x_p = x_S$, so:

$$C_A = \alpha \mu_A(T) \tag{3.4}$$

$$L_A = \beta {\mu_A}^2(T) \tag{3.5}$$

where the subscript 'A' denotes parameters of the annealed material. Combining equations 3.4 and 3.5 gives

$$\frac{\beta}{\alpha^2} = \frac{L_A}{{C_A}^2} \tag{3.6}$$

which can be obtained from the gradients of the linear fits to the annealed sample data in figure 3.9. Similarly, equations 3.2 and 3.3 can combine to give

$$\frac{L_U}{{C_U}^2} = \frac{\beta}{\alpha^2} \frac{(x_p + x_a)(x_S + x_I)}{(x_p - x_a)^2} \tag{3.7}$$

Substituting equation 3.6 gives

$$\frac{L_U}{{C_U}^2}\frac{{C_A}^2}{L_A} = \frac{(x_p + x_a)(x_S + x_I)}{(x_p - x_a)^2} \tag{3.8}$$

which may be solved for different assumptions of the Mn_I behaviour to give an estimate of the proportion of Mn_I present in as-grown (Ga,Mn)As, x_I/x_T.

The three assumptions considered are depicted in figure 3.11. In the first, all the Mn_{Ga} are ferromagnetically aligned, and the Mn_I are non-magnetic; in the second, the Mn_I directly passivate an equal number of Mn_{Ga}, becoming disordered while the remaining Mn_{Ga} are ferromagnetic, with no antiferromagnetic alignment to the applied field direction; in the third, the Mn_I align antiparallel to the applied field direction. In terms of the partial Mn concentrations, these assumptions may be described by: (i) $x_p = x_S$ and $x_a = 0$, (ii) $x_p = x_S - x_I$ and $x_a = 0$, (iii) $x_p = x_S$ and $x_a = x_I$.

Let $\eta = \frac{L_U}{{C_U}^2}\frac{{C_A}^2}{L_A}$, the ratio of the gradients of the linear fits in figure 3.9; then equation 3.8 can be manipulated for each scenario:

I

$$\eta = \frac{(x_S + x_I)}{x_S} \tag{3.9}$$

$$x_I = (\eta - 1)x_S$$

$$x_I = \left(\frac{\eta - 1}{\eta}\right) x_T \tag{3.10}$$

II

$$\eta = \frac{(x_S - x_I)(x_S + x_I)}{(x_S - x_I)^2} \tag{3.11}$$

$$x_I = \left(\frac{\eta - 1}{\eta + 1}\right) x_S$$

$$x_I = \left(\frac{\eta - 1}{2\eta}\right) x_T \tag{3.12}$$

III

$$\eta = \frac{(x_s + x_I)^2}{(x_s - x_I)^2} \tag{3.13}$$

$$x_I = \left(\frac{\sqrt{\eta} - 1}{\sqrt{\eta} + 1}\right) x_S$$

$$x_I = \left(\frac{\sqrt{\eta} - 1}{2\sqrt{\eta}}\right) x_T \tag{3.14}$$

Then, to evaluate the local magnetic moment in the as-grown material, $\mu_U(T)$, equations 3.2 and 3.4 are combined to give:

$$\mu_U(T) = C_U(T)\frac{\mu_A(T)}{C_A(T)}\left(\frac{x_S + x_I}{x_p - x_a}\right) \tag{3.15}$$

where the calculated magnetic moment M_{XMCD} at 15 K in table 3.3 can be used for $\mu_A(15\ \mathrm{K})$. The corresponding XMCD intensities $C_A(15\ \mathrm{K})$ and $C_U(15\ \mathrm{K})$ may both be taken from the values plotted in figure 3.9. Using equations 3.9, 3.11 and 3.13, $\mu(15\ \mathrm{K})$ can be evaluated for each scenario:

I

$$\mu_U = \frac{\mu_A C_U}{C_A}\left(\frac{x_S + x_I}{x_S}\right)$$

$$\mu_U = \frac{\mu_A C_U}{C_A}\eta \tag{3.16}$$

II

$$\mu_U = \frac{\mu_A C_U}{C_A}\left(\frac{x_S + x_I}{x_S - x_I}\right)$$

$$\mu_U = \frac{\mu_A C_U}{C_A}\eta \tag{3.17}$$

III

$$\mu_U = \frac{\mu_A C_U}{C_A}\left(\frac{x_S + x_I}{x_S - x_I}\right)$$
$$\mu_U = \frac{\mu_A C_U}{C_A}\sqrt{\eta} \tag{3.18}$$

The local moment is therefore the same for scenarios I and II, but smaller for III. Once $\mu_U(15\text{ K})$ is calculated, it is scaled by $M_{\text{SQUID}}(0\text{ K})/M_{\text{SQUID}}(15\text{ K})$ (see figure 3.5) to give an estimate of $\mu_U(0\text{ K})$, the maximum local moment in the absence of suppression by thermal effects. The values of x_I/x_T and $\mu_U(0\text{ K})$ calculated for the as-grown samples B and D are shown in table 3.4. Corresponding values from the literature are displayed in Table 3.5.

Sample	Scenario	x_I/x_T	$\mu_U(0\text{ K})$ [(μ_B/Mn)]
B (∼7.5% Mn)	I	0.31 ± 0.04	3.5 ± 0.4
	II	0.16 ± 0.02	3.5 ± 0.4
	III	0.09 ± 0.01	2.9 ± 0.2
D (∼3% Mn)	I	0.19 ± 0.07	4.3 ± 0.6
	II	0.10 ± 0.03	4.3 ± 0.6
	III	0.05 ± 0.02	3.8 ± 0.3

Table 3.4: Calculated fractions of Mn in interstitial positions, and the corresponding local moment of ferromagnetic Mn. The values are shown for as-grown samples with high (∼ 7.5%) and low Mn content (∼ 3%), for the three scenarios depicted in figure 3.11.

The first scenario clearly overestimates x_I/x_T in sample B: at one third of the total Mn concentration, the double donor Mn_I would result in total compensation of the holes provided by Mn_Ga, effectively precluding this scenario in this ferromagnetic sample. The fraction of Mn_I given in Scenario III is slightly lower than expected; since it has already been established that the XMLD signal is reduced in as-grown material (figure 3.7), Scenario III is also unlikely. The Mn_I fractions estimated in Scenario II seems to give the most realistic values, matching well with estimations based on c-PIXE measurements [29, 52], and reasonably well with estimations based on magnetotransport data [31] and with estimation of 'f_{lost}' from comparison of SQUID and XMCD data in Section 3.4.1. The Mn_I concentration is shown to increase with total Mn concentration, in agreement with Ref. [31] and Section 3.4.1 of this chapter.

Nominal Mn content	x_I/x_T	Source	Technique
∼6% Mn	0.10	[52]	c-PIXE
∼8% Mn	0.17	[29]	c-PIXE
3.3% Mn	∼0.15	[31]	Magnetotransport
6.4% Mn	∼0.23	[31]	Magnetotransport

Table 3.5: Fraction of Mn_I for different amounts of total Mn concentration, published in the literature.

With the assumption that Scenario II is the most plausible one, the corresponding local magnetic moment μ_U of sample B appears to be substantially less than that of annealed sample A. Interestingly, this is not the case for the low Mn content samples: μ_U of sample D is about the same as for sample C, remaining well within the error bars. This suggests that in as-grown (Ga,Mn)As with low Mn content, the magnetization suppression is caused only by the formation of magnetically inactive Mn_{Ga}-Mn_I pairs, while material with high Mn content may have the additional compensating mechanism of non-collinear ferromagnetic order. The most likely possibility is a disordered local Mn moment [20] brought about by the greater hole suppression seen in high Mn content samples.

3.6 Summary

The large XMLD signal measured in (Ga,Mn)As indicates a large, partially localized Mn moment. Samples with lower carrier concentration are more localized, suggested by small changes in the structure of the XMLD. A very large anisotropy in the XMLD spectrum is observed on rotation of the polarization and magnetization vectors with respect to the crystalline axes. Atomic multiplet calculations show that this is a single-ion effect induced by the crystal field.

The XMCD and XMLD signals are both suppressed in as-grown material, because they are seen to increase upon annealing. This indicates a lack of long-range antiferromagnetic ordering. In more heavily Mn-doped material, the magnetic moment 'per ferromagnetic Mn atom' is suppressed, even after accounting for the interstitial Mn. Conversely, in lightly-doped material, the moment of the ferromagnetic Mn does not seem to be suppressed; the magnetization suppression seems to come only from the formation of 'spin-zero' Mn_{Ga}-Mn_I pairs.

References

[1] H. Ohldag, V. Solinus, F. U. Hillebrecht, J. B. Goedkoop, M. Finazzi, F. Matsukura, and H. Ohno, *Applied Physics Letters* **76**, 2928 (2000).

[2] S. Ueda, S. Imada, T. Muro, Y. Saitoh, S. Suga, F. Matsukura, and H. Ohno, *Physica E* **10**, 210 (2001).

[3] K. W. Edmonds, N. R. S. Farley, R. P. Campion, C. T. Foxon, B. L. Gallagher, T. K. Johal, G. van der Laan, M. MacKenzie, J. N. Chapman, and E. Arenholz, *Applied Physics Letters* **84**, 4065 (2004).

[4] O. Rader, K. Fauth, C. Gould, C. Ruster, G. M. Schott, G. Schmidt, K. Brunner, L. W. Molenkamp, G. Schutz, and F. Kronast, *Journal of Electron Spectroscopy and Related Phenomena* **144-147**, 789 (2005).

[5] A. Fujimori, J. Okabayashi, Y. Takeda, T. Mizokawa, J. Okamoto, K. Mamiya, Y. Saitoh, Y. Muramatsu, M. Oshima, S. Ohya, and M. Tanaka, *Journal of Electron Spectroscopy and Related Phenomena* **144-147**, 701 (2005).

[6] P. Gambardella, H. Brune, S. S. Dhesi, P. Bencok, S. R. Krishnakumar, S. Gardonio, M. Veronese, C. Grazioli, and C. Carbone, *Physical Review B* **72**, 045337 (2005).

[7] K. W. Edmonds, N. R. S. Farley, T. K. Johal, G. van der Laan, R. P. Campion, B. L. Gallagher, and C. T. Foxon, *Physical Review B* **71**, 064418 (2005).

[8] G. van der Laan, B. T. Thole, G. A. Sawatzky, J. B. Goedkoop, J. C. Fuggle, J.-M. Esteva, R. Karnatak, J. P. Remeika, and H. A. Dabkowska, *Physical Review B* **34**, 6529 (1986).

[9] P. Kuiper, B. G. Searle, P. Rudolf, L. H. Tjeng, and C. T. Chen, *Phys. Rev. Lett.* **70**, 1549 (1993).

[10] M. W. Haverkort, S. I. Csiszar, Z. Hu, S. Altieri, A. Tanaka, H. H. Hsieh, H. J. Lin, C. T. Chen, T. Hibma, and L. H. Tjeng, *Physical Review B* **69**, 020408 (2004).

[11] A. Scholl, M. Liberati, E. Arenholz, H. Ohldag, and J. Stöhr, *Phys. Rev. Lett.* **92**, 247201 (2004).

[12] F. Nolting, A. Scholl, J. Stohr, J. Seo, J. Fompeyrine, H. Siegwart, J. Locquet, S. Anders, J. Luning, E. Fullerton, M. Toney, M. Scheinfein, and H. Padmore, *Nature* **405**, 767 (2000).

[13] S. Czekaj, F. Nolting, L. J. Heyderman, P. R. Willmott, and G. van der Laan, *Physical Review B(Condensed Matter and Materials Physics)* **73**, 020401 (2006).

[14] G. van der Laan, *Physical Review Letters* **82**, 640 (1999).

[15] S. S. Dhesi, G. van der Laan, E. Dudzik, and A. B. Shick, *Physical Review Letters* **87**, 067201 (2001).

[16] S. S. Dhesi, G. van der Laan, and E. Dudzik, *Applied Physics Letters* **80**, 1613 (2002).

[17] M. M. Schwickert, G. Y. Guo, M. A. Tomaz, W. L. O'Brien, and G. R. Harp, *Phys. Rev. B* **58**, R4289 (1998).

[18] T. Jungwirth, J. Mašek, K. Y. Wang, K. W. Edmonds, M. Sawicki, M. Polini, J. Sinova, A. H. MacDonald, R. P. Campion, L. X. Zhao, N. R. S. Farley, T. K. Johal, G. van der Laan, C. T. Foxon, and B. L. Gallagher, *Physical Review B* **73**, 165205 (2006).

[19] T. Dietl, H. Ohno, and F. Matsukura, *Physical Review B* **63**, 195205 (2001).

[20] P. A. Korzhavyi, I. A. Abrikosov, E. A. Smirnova, L. Bergqvist, P. Mohn, R. Mathieu, P. Svedlindh, J. Sadowski, E. I. Isaev, Y. K. Vekilov, and O. Eriksson, *Physical Review Letters* **88**, 187202 (2002).

[21] X. Liu, W. L. Lim, M. Dobrowolska, J. K. Furdyna, and T. Wojtowicz, *Physical Review B* **71**, 035307 (2005).

[22] G. Zaránd and B. Jankó, *Physical Review Letters* **89**, 047201 (2002).

[23] M. Berciu and R. N. Bhatt, *Physical Review Letters* **87**, 107203 (2001).

[24] J. Schliemann, *Physical Review B* **67**, 045202 (2003).

[25] G. A. Fiete, G. Zarand, B. Janko, P. Redlinski, and C. P. Moca, *Physical Review B* **71**, 115202 (2005).

[26] J. Schliemann and A. H. MacDonald, *Physical Review Letters* **88**, 137201 (2002).

[27] L. Brey and G. Gómez-Santos, *Physical Review B* **68**, 115206 (2003).

[28] R. P. Campion, K. W. Edmonds, L. X. Zhao, K. Y. Wang, C. T. Foxon, B. L. Gallagher, and C. R. Staddon, *Journal of Crystal Growth* **247**, 42 (2003).

[29] K. M. Yu, W. Walukiewicz, T. Wojtowicz, I. Kuryliszyn, X. Liu, Y. Sasaki, and J. K. Furdyna, *Physical Review B* **65**, 201303 (2002).

[30] J. Blinowski and P. Kacman, *Physical Review B* **67**, 121204 (2003).

[31] K. Y. Wang, K. W. Edmonds, R. P. Campion, B. L. Gallagher, N. R. S. Farley, C. T. Foxon, M. Sawicki, P. Boguslawski, and T. Dietl, *Jounal of Applied Physics* **95**, 6512 (2004).

[32] A. Oiwa, S. Katsumoto, A. Endo, M. Hirasawa, Y. Iye, H. Ohno, F. Matsukura, A. Shen, and Y. Sugawara, *Solid State Communications* **103**, 209 (1997).

[33] K. W. Edmonds, P. Bogusławski, K. Y. Wang, R. P. Campion, S. N. Novikov, N. R. S. Farley, B. L. Gallagher, C. T. Foxon, M. Sawicki, T. Dietl, M. B. Nardelli, and J. Bernholc, *Physical Review Letters* **92**, 037201 (2004).

[34] E. Arenholz and S. O. Prestemon, *Review of Scientific Instruments* **76**, 083908 (2005).

[35] K. Y. Wang, M. Sawicki, K. W. Edmonds, R. P. Campion, S. Maat, C. T. Foxon, B. L. Gallagher, and T. Dietl, *Physical Review Letters* **95**, 217204 (2005).

[36] M. Abolfath, T. Jungwirth, J. Brum, and A. H. MacDonald, *Phys. Rev. B* **63**, 054418 (2001).

[37] X. Liu, Y. Sasaki, and J. K. Furdyna, *Physical Review B* **67**, 205204 (2003).

[38] C. Gould, C. Ruster, T. Jungwirth, E. Girgis, G. M. Schott, R. Giraud, K. Brunner, G. Schmidt, and L. W. Molenkamp, *Physical Review Letters* **93**, 117203 (2004).

[39] A. A. Freeman, K. W. Edmonds, G. van der Laan, N. R. S. Farley, T. K. Johal, E. Arenholz, R. P. Campion, C. T. Foxon, and B. L. Gallagher, *Physical Review B* **73**, 233303 (2006).

[40] G. van der Laan, *Physical Review B* **55**, 8086 (1997).

[41] J. Kuneš and P. M. Oppeneer, *Physical Review B* **67**, 024431 (2003).

[42] G. van der Laan and B. T. Thole, *Physical Review B* **43**, 13401 (1991).

[43] G. van der Laan, Single atom multiplet calculations for XMLD spectra, private communication, 2005.

[44] K. W. Edmonds, G. van der Laan, A. A. Freeman, N. R. S. Farley, T. K. Johal, R. P. Campion, C. T. Foxon, B. L. Gallagher, and E. Arenholz, *Physical Review Letters* **96**, 117207 (2006).

[45] P. Mahadevan and A. Zunger, *Physical Review B* **69**, 115211 (2004).

[46] E. Arenholz, G. van der Laan, R. V. Chopdekar, and Y. Suzuki, *Physical Review B* **74**, 094407 (2006).

[47] E. Arenholz, G. van der Laan, R. V. Chopdekar, and Y. Suzuki, *Physical Review Letters* **98**, 197201 (2007).

[48] G. van der Laan, E. Arenholz, R. V. Chopdekar, and Y. Suzuki, *Physical Review B* **77**, 064407 (2008).

[49] A. Van Esch, L. Van Bockstal, J. De Boeck, G. Verbanck, A. S. van Steenbergen, P. J. Wellmann, B. Grietens, R. Bogaerts, F. Herlach, and G. Borghs, *Physical Review B* **56**, 13103 (1997).

[50] K. C. Ku, S. J. Potashnik, R. F. Wang, S. H. Chun, P. Schiffer, N. Samarth, M. J. Seong, A. Mascarenhas, E. Johnston-Halperin, R. C. Myers, A. C. Gossard, and D. D. Awschalom, *Applied Physics Letters* **82**, 2302 (2003).

[51] K. W. Edmonds, G. van der Laan, N. R. S. Farley, E. Arenholz, R. P. Campion, C. T. Foxon, and B. L. Gallagher, *Physical Review B* **77**, 113205 (2008).

[52] A. W. Rushforth, N. R. S. Farley, R. P. Campion, K. W. Edmonds, C. R. Staddon, C. T. Foxon, B. L. Gallagher, and K. M. Yu, *Physical Review B (Condensed Matter and Materials Physics)* **78**, 085209 (2008).

Chapter 4

XMCD of (Ga,Mn)N at the Mn L-edge

4.1 Introduction

As mentioned in Chapter 1, the question of ferromagnetism in (Ga,Mn)N is one of some controversy. Reports of room-temperature ferromagnetism are usually for n-type material, in contradiction with the p-type criterion stipulated by mean-field predictions [1]. In fact, the Zener mean-field model of ferromagnetism in DMS is incompatible with (Ga,Mn)N: substitutional Mn_{Ga} in GaN forms an acceptor level deep within the band-gap [2]. In GaAs, the impurity level forms ∼100 meV above the top of the valence band and broadens to merge with it at higher Mn concentrations, providing holes. As shown by Gosk *et al.* [3], it is possible to make (Ga,Mn)N p-type by co-doping with acceptors, but this forces the Mn into a d^4 state. Itinerant hole-mediated ferromagnetism is therefore not possible in (Ga,Mn)N; the numerous claims of room-temperature ferromagnetism in (Ga,Mn)N are generally attributable to precipitate phases.

For (Ga,Mn)N material that is free of precipitates, a weak ferromagnetic behaviour is sometimes observed; this may be explained by mechanisms other than itinerant exchange. One such example is *double exchange*, which requires the compound to have magnetic ions of mixed valency. In this situation, the spin-alignment of the ions is mediated by carriers hopping from ions of one valency to those of the other. This leads to the question of

the valency of Mn in (Ga,Mn)N. In (Ga,Mn)As, the impurity band intersects the valence band [4], so the Mn valency is nearly pure d^5. In contrast, the impurity band in (Ga,Mn)N lies deep within the band-gap. The position of the Fermi level with respect to the impurity band determines the carrier type and Mn valency.

Measurements by x-ray absorption of n-type wurtzite (Ga,Mn)N have indicated that the Mn is in a d^5 state (Mn^{2+}) [5,6]. However, a more bulk-sensitive XMCD study has indicated a predominance of a d^4 state (Mn^{3+}) with an accompanying low T_C [7]. From study of the magnetization, there is evidence that both Mn^{2+} and Mn^{3+} states may coexist [3]. This situation could allow ferromagnetic ordering, mediated by the double-exchange of holes in the mid-gap impurity band.

There are two distinct components often observed in the Mn L_3-edge absorption and XMCD spectra. These have been interpreted as two d^5 configurations, with different local environments due to the presence of structural defects [8]. Elsewhere, a recent study [9] the field-dependence of the $L_{2,3}$-edge XMCD has revealed coexisting para- and ferromagnetic behaviour for the respective lower and higher energy components of the L_3 peak, attributed to Mn^{2+} with different electronic environments.

The present study expands on our published work [10]: we investigate the field-dependent behaviour of the two components identified in Refs. [8] and [9] for (Ga,Mn)N films of both wurtzite and zinc-blende structure, and deduce that their concentrations are depth-dependent.

4.2 Experimental details

4.2.1 Sample details

Two zinc-blende and two wurtzite (Ga,Mn)N samples were measured, grown by plasma-assisted MBE. The wurtzite samples were grown on 1 mm thick AlN-on-sapphire templates provided by the company NGK. The zinc-blende samples were grown on a SiC thick layer deposited by chemical vapor deposition on a Si substrate. The substrates and buffer layers were prepared by the group of E. Sarigiannidou, H. Mariette, et al. in Grenoble, France. Prior to the (Ga,Mn)N growth, a 300 nm GaN buffer layer was deposited by MBE. All

the (Ga,Mn)N layers were grown at the University of Nottingham, to a thickness of 0.5 µm at a substrate temperature of 700°C under N-rich conditions, at a background pressure of 10^{-8} mbar, growth pressure of 2×10^{-5} mbar, and deposition rate of 0.25 μm/hr. The Mn flux used during growth corresponds to a ∼2-3% Mn content, and was the same for all samples. However, the Mn incorporation may not be the same for the different host structure types; for example, the absorption spectra for the wurtzite samples have a higher integrated intensity than the zinc-blende samples (up to twice as large), indicating a greater amount of incorporated Mn.

Some samples were grown in the presence of an As_2 flux. This was done in an attempt to incorporate As into the (Ga,Mn)N film during growth, with the hope that it could affect the band structure by bringing the impurity band closer to the valence band, potentially making the material *p*-type. Such an enhancement of the low-temperature conductivity might allow the onset of the keenly sought-after itinerant hole-mediated ferromagnetism predicted in (Ga,Mn)N [1]. Unfortunately, this did not have any observable effect on the carrier type: the zinc-blende samples remained *n*-type and the wurtzite were insulating. The sample details are summarized in table 4.1.

The samples were initially characterized by x-ray diffraction and secondary ion mass spectroscopy (SIMS). The two zinc-blende samples Ms758 and Ms759 show diffraction peaks at 2θ=40°, and an absence of a peak at 2θ=35°, indicating the samples are zinc-blende and free of any hexagonal inclusions. Similarly, the data for the wurtzite samples Ms760 and Ms761 describe a purely hexagonal structure.

Depth-dependent concentrations of each element within the material may be estimated from SIMS data. For sample Ms761 (grown in the presence of an As_2 flux), the measurements unsurprisingly report a concentration of incorporated As an order of magnitude greater than that of Ms760 (10^{19} and 10^{18} As cm^{-3}, respectively). The As depth profile is reasonably uniform (though Ms760 has a narrow surface region of ∼20 nm where the As concentration shoots up by an order of magnitude). Strangely, the data for Ms758 (supposedly grown in the absence of an As_2 flux) imply that it had *more* As incorporated than sample Ms759. The data for Ms758 exhibit a very non-uniform As concentration in the bulk, again with a ∼20 nm region where the concentration reaches 10^{19} As cm^{-3}. In the

case of Ms759, the bulk As concentration is a fairly uniform $\sim 3 \times 10^{17}$, but rises as high as $\sim 10^{19}$ in a ∼100 nm region below the surface. If the data are to be trusted, they would imply that very little of the As is incorporated into the bulk of Ms759, instead forming an As-rich layer at the top 1/5 of the film.

Sample	Structure	Substrate	As_2 flux?	Growth temp.	Carrier conc.
Ms758	Zinc-blende	GaN/SiC/Si	No	∼700°C	$n \sim 10^{18}$ cm^{-3}
Ms759	Zinc-blende	GaN/SiC/Si	Yes	∼700°C	$n \sim 10^{18}$ cm^{-3}
Ms760	Wurtzite	AlN/Sapphire	No	∼700°C	insulating
Ms761	Wurtzite	AlN/Sapphire	Yes	∼700°C	insulating

Table 4.1: Sample details

The SIMS data may be used as a rough estimate of the concentration of elements within the material: the results indicate that the incorporated Mn content is around 2% for the wurtzite samples, but only 0.2% for the zinc-blende samples. While the Mn concentration determined by SIMS in (Ga,Mn)As has been shown to be in fairly good agreement with the nominal Mn concentration [11], the technique can have some problems (for example, the hole bored into the sample tends to be conical rather than cylindrical, so the information comes from a range of depths rather than a single depth). Moreover, a comparison of the integrated absorption spectra indicates that the Mn concentration in the wurtzite samples is only as much as a factor of 2 more than that of the zinc-blende; the integrated absorption spectra are more of a reliable gauge of relative Mn concentrations than the SIMS.

4.2.2 Experimental procedure

The x-ray absorption and XMCD measurements were obtained on beamline ID08 at the European Synchrotron Radiation Facility (ESRF) in Grenoble. The sample temperature was 10 K throughout. To measure the XMCD, four absorption spectra were taken for different configurations of photon helicity and applied magnetic field direction (ranging from −5 T to +5 T), and the difference spectrum was obtained by subtracting the antiparallel from parallel configurations. Etching in aqua regia and HF prior to the measurement did not make a significant difference to the spectra, suggesting that surface contamination is not important in these samples.

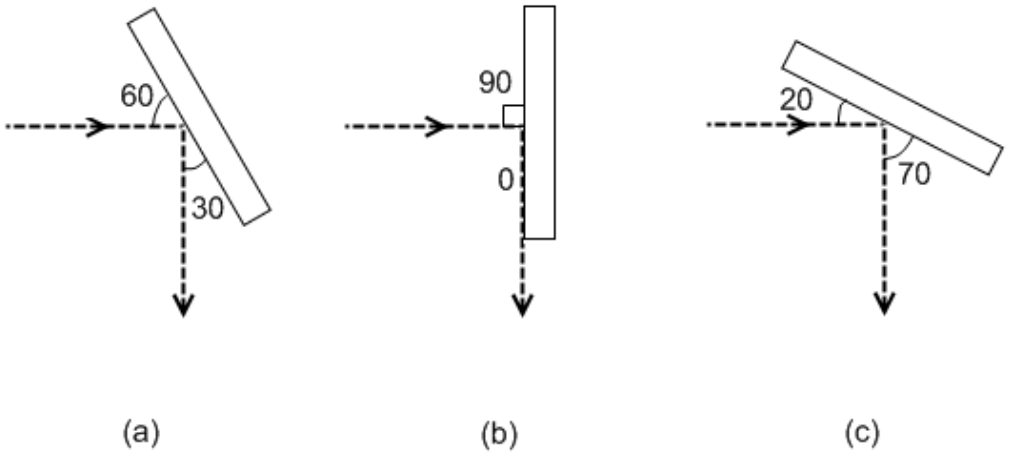

Figure 4.1: Experimental geometries used in this study: (a) all samples were measured with x-rays incident at 60° from the sample surface. Sample Ms761 was also measured at (b) normal incidence, and (c) with photons incident at 20° to the sample surface. The fluorescence detector was always positioned at 90° from the incident beam.

X-ray absorption measurements in FY and TEY detection modes were collected simultaneously, with photon incidence at 60° to the sample surface, and with the fluorescence detector always at 90° to the incident beam (shown in figure 4.1 (a)). One of the samples (Ms761) was additionally measured with photons incident at 90° and 20° to the sample surface (4.1 (b) and (c), respectively).

4.2.3 Technique Limitations and Difficulties

Detection modes

In this study x-ray spectroscopy data were collected synchronously by FY and TEY. In the former mode of detection, the core hole created by the incoming photon decays by radiative emission of a photon, i.e. the inverse of the x-ray absorption process. It has been shown that FY detection does not exactly measure the absorption cross-section [12]. The alternative mode of core hole decay occurs by the emission of a secondary Auger electron from the excited atom's conduction band. This is the dominating mode of decay, typically $\sim 99\%$ for a Mn $2p$ core hole [13]. This mode of detection is found to be a correct measure of the x-ray absorption cross section and as such would be the favourable mode of detection

for this experiment. However, (Ga,Mn)N is a wide band-gap material whose conductivity increases with temperature, so at low temperatures TEY spectra measured by reading the drain current are prone to a poor signal-to-noise ratio.

FY is more sensitive to the bulk of the layers, but is prone to *saturation effects* due to the comparable mean free paths of incoming and outgoing photons (see Section 2.7 of Chapter 2). This can lead to distortion of the spectra by suppression of the most intense peaks, and is addressed in detail in Section 4.4.1 of the present Chapter, including an attempt to correct for this effect. Generally, the TEY spectra are more useful for quantitative analysis in this study, for which the saturation effect would be negligible under the present measurement conditions [14].

Experimental problems; manipulation during analysis

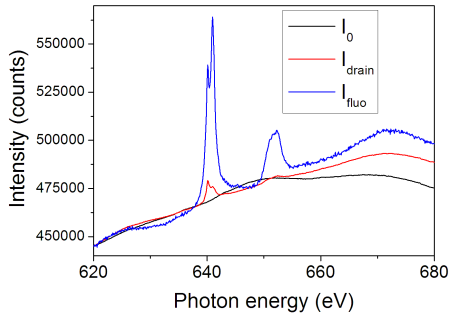

(a) I_{drain} and I_{fluo} scaled to compare with I_0.

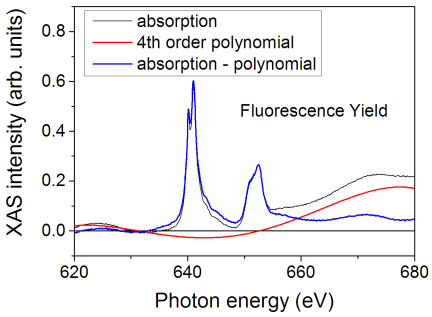

(b) Fluorescence yield absorption spectrum.

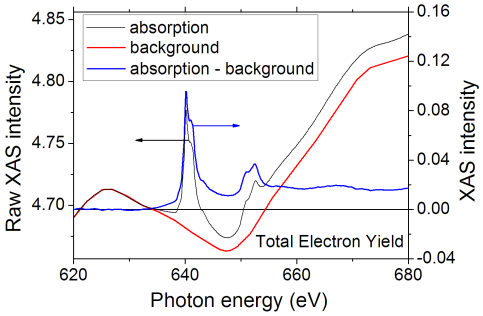

(c) Total electron yield absorption spectrum.

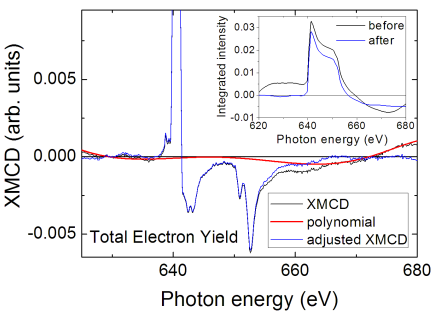

(d) Total electron yield XMCD spectrum.

Figure 4.2: Sample Ms758. (a) I_0, drain current, and fluorescence signals compared. (b)-(d) x-ray absorption and XMCD spectra with background signals fitted and removed.

It should be noted that many of the spectra presented in this study suffered from nonlinear background signals, as shown in figure 4.2. In figure 4.2(a), the raw signals from drain current (I_{drain}) and fluorescence (I_{fluo}) are scaled to compare to the x-ray intensity before encountering the sample, I_0. The nonlinear backgrounds of I_{drain} and I_{fluo} are not well-matched by I_0. The signal-to-background ratio of the drain current is much smaller than that in fluorescence, so the TEY absorption spectrum given by I_{drain}/I_0 has a more distorted background than I_{fluo}/I_0. This is clear from figures 4.2(b) and 4.2(c). The nonlinear backgrounds are unlikely to be caused by charging of the sample, because there would be sharp discontinuities caused by the sample discharging, rather than the smooth background observed here. The undulations are probably due to the EXAFS region of the oxygen K-edge, resulting from oxygen at the surface of the sample.

It was necessary to fit and remove a background signal from most of the spectra before it was possible to perform integration, and thereby use sum rules or determine the branching ratios. The background removal was done with the greatest possible care, yet it should be noted that doing this can easily and drastically change the calculated spin and orbital magnetic moments. In figure 4.2(b), a reasonable fit is made to the background using a 4th-order polynomial function. Figure 4.2(c) shows a more severe background distortion of the absorption spectrum. Polynomial fitting to the background was not sufficient for these; instead the background must be described by a hand-drawn function. Though great care was taken over this, ultimately it must be conceded that removing a background this way subjects the resulting branching ratio to a large uncertainty. In figure 4.2(d), a fifth-order polynomial function is fitted to the background of the XMCD spectrum; the improvement to its integrated spectrum is shown in the inset to this figure.

4.3 X-ray absorption results

4.3.1 Splitting of L_3 peak

Figure 4.3 shows experimental Mn $L_{2,3}$ x-ray absorption and XMCD spectra for the zinc-blende and wurtzite samples measured in FY mode, along with spectra from atomic multiplet calculations [15] for Mn d^4 and Mn d^5. Figure 4.4 shows the same complement of

results but measured by TEY, along with the same calculated spectra for comparison.

For all samples studied, the L_3 peak is found to be split into two components. The peaks are separated by 0.85 ± 0.05 eV for all samples. Other studies [8, 9] report smaller peak separations, which may indicate the states in the Mn^{2+}/Mn^{3+} impurity level are weighted closer to Mn^{2+}. The relative intensities of each peak vary from sample to sample (they also depend on detection mode used, addressed next). The intensity ratio of the lower-energy peak (denoted A) to the higher-energy peak (denoted B) is larger for zinc-blende than for wurtzite samples. The variation in the relative intensities of the two components between samples indicates that each corresponds to a distinct ionic state or local environment.

Peak B occurs at a lower energy than the major peak of calculated d^4 absorption spectra [16], so is unlikely to be from pure Mn^{3+}. The measurements in TEY mode (figure 4.4) show the low-energy peak is dominant for all samples; in FY mode, the wurtzite samples show a much stronger high energy peak than observed from the zinc-blende.

Effect of As_2 flux during growth

Attention is now turned to the differences in the absorption spectra when the material is grown with or without an As_2 flux. These are overlaid in figures 4.3 and 4.4 for each structure type to aid comparison. What is immediately obvious is that for the wurtzite samples, the inclusion of an As_2 flux during growth seems to have very little effect upon the lineshape of the absorption spectrum from either detection mode; on the other hand in the zinc-blende there is a pronounced change in the relative intensity of the two L_3 peaks.

If some As atoms were to become incorporated into the (Ga,Mn)N material, it might lead to some change in the strain in the thin film layer, which would modify the magnetic anisotropy (possibly changing from simple cubic to a uniaxial behaviour). The angular dependence of the magnetic moments measured by FY in Section 4.4.1, and for the TEY XMCD of sample Ms761 is investigated in Section 4.4.2.

The discussion will further speculate on the possible effects of the As_2 flux upon the results.

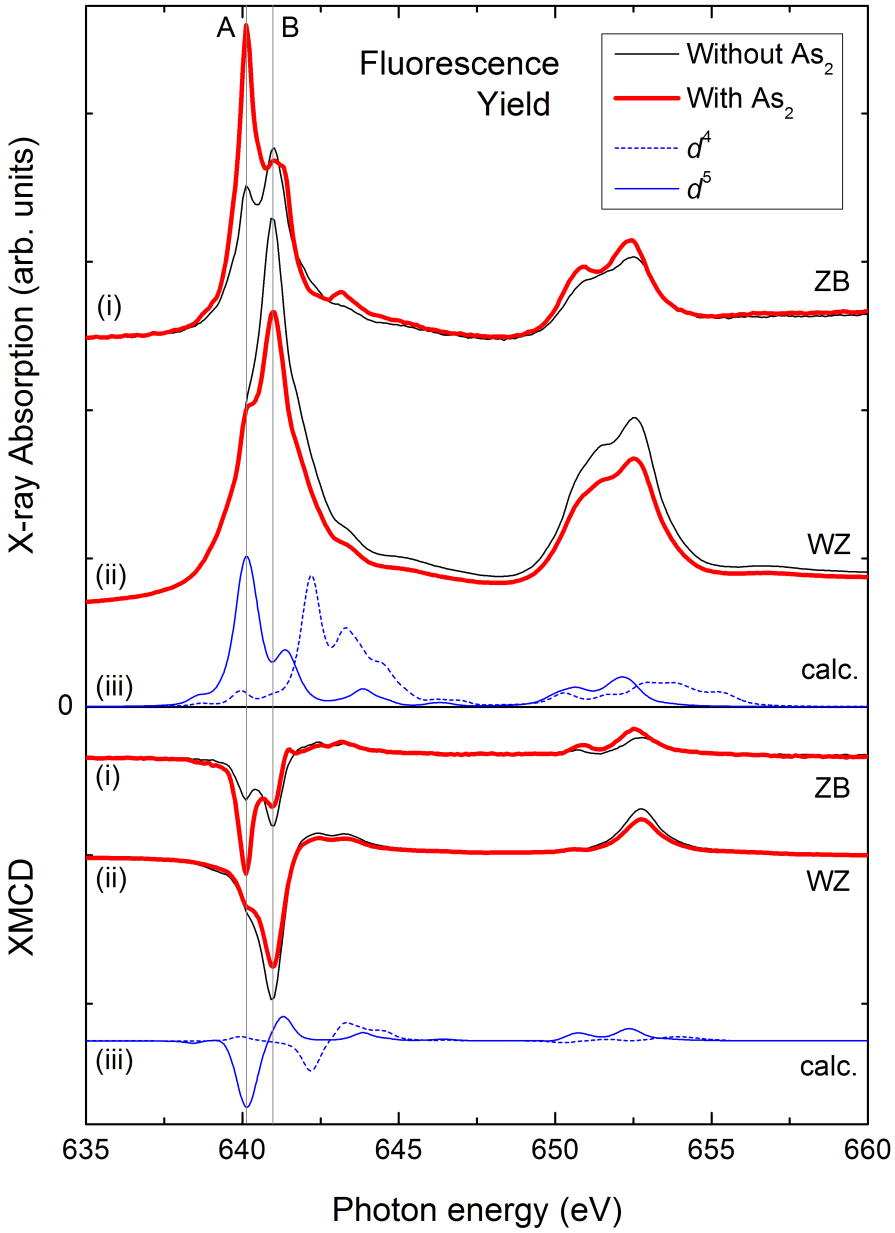

Figure 4.3: Fluorescence yield spectra. Top panel: (i) Mn $L_{2,3}$ absorption spectra for two zinc-blende samples, (ii) for two wurtzite samples, (iii) and calculated spectra for Mn d^5 (line) and Mn d^4 (dashed) (Ref. [16]). The experimental spectra are the sum of polarization-averaged absorption spectra taken at +5 T and −5 T, measured in FY mode at 10 K. Bottom panel: Corresponding XMCD spectra for the same samples at the same applied magnetic field and temperature.

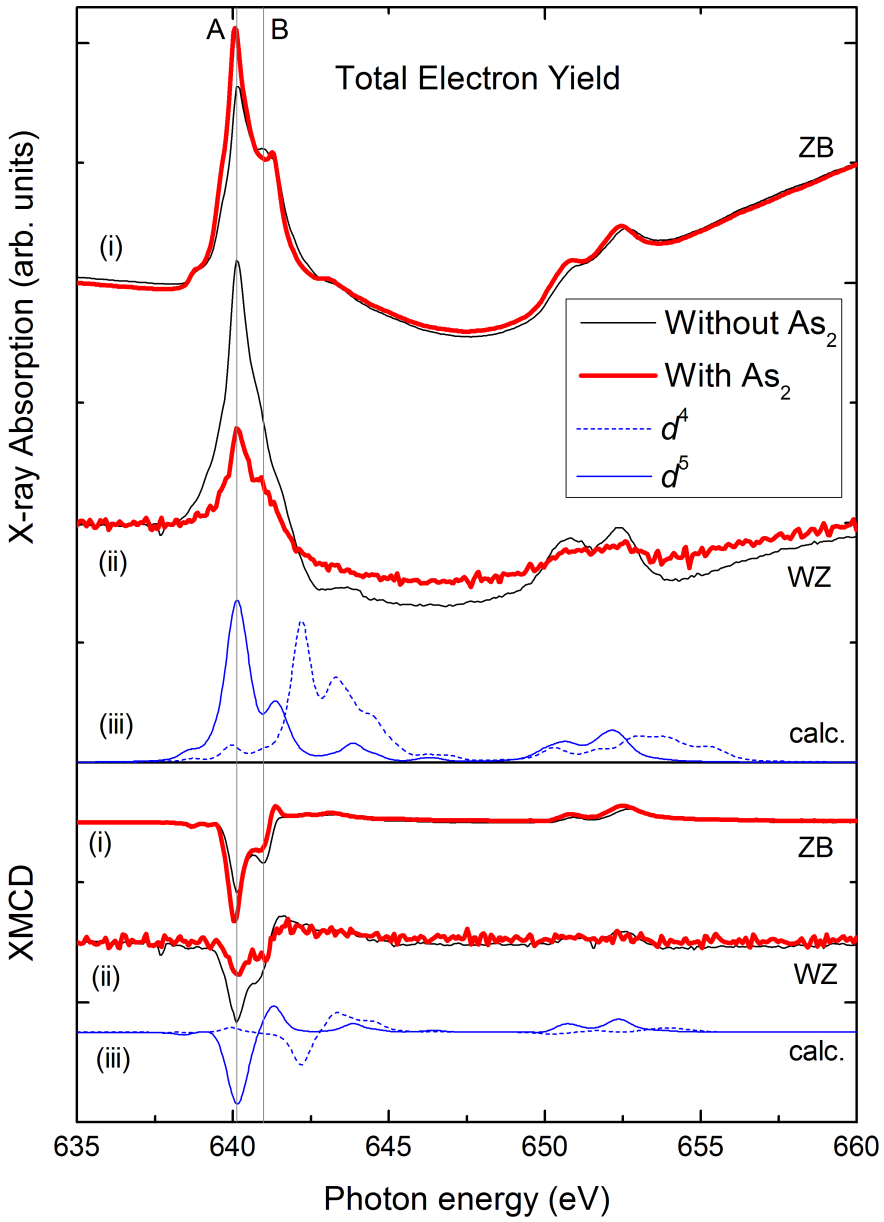

Figure 4.4: Total electron yield spectra. Top panel: (i) Mn $L_{2,3}$ absorption spectra for two zinc-blende samples, (ii) for two wurtzite samples, (iii) and calculated spectra for Mn d^5 (line) and Mn d^4 (dashed) (Ref. [16]). The experimental spectra are the sum of polarization-averaged absorption spectra taken at +5 T and −5 T, measured in FY mode at 10 K. Bottom panel: Corresponding XMCD spectra for the same samples at the same applied magnetic field and temperature.

4.3.2 Comparison of FY and TEY detection modes

Probing depths

The depth from which information may be obtained by TEY is determined by the mean free path of the Auger electrons emitted from the absorbing atom; this predominantly depends upon the electron kinetic energy, and in (Ga,Mn)N is of the order of ∼2 nm [14]. For very strong magnetic fields ($\gtrsim$1 T), the path of the escaped electrons may be bent so strongly that they re-enter the sample, effectively reducing the information depth of the TEY.

Fluorescence photons can travel much further before being re-absorbed: their attenuation length at the L_α emission line (637.4 eV) of Mn in (Ga,Mn)N is calculated to be 262 nm for a wurtzite structure and 273 nm for zinc-blende*. Most spectra were taken with photons emitted at 30° to the sample surface, so the information depth of the FY data is 131 nm for wurtzite and 137 nm for zinc-blende.

It is possible to infer information about the depth profile of the states corresponding to peaks A and B, because of the different probing depths of the FY and TEY and their significantly differing x-ray absorption lineshapes. For all samples, measurements obtained in the more surface-sensitive TEY mode show a larger A/B ratio than measurements in FY mode — in fact peak A is consistently dominant in the absorption spectrum from TEY. To illustrate this, figure 4.5 compares x-ray absorption measurements for zinc-blende sample Ms758 measured in FY and TEY modes. From this we can conclude that the Mn in the configuration corresponding to peak A resides towards the surface, while the higher energy peak B corresponds to Mn residing in the bulk of the material.

There is an even more pronounced shift in the A/B ratio in the wurtzite samples. This may be seen by comparing their spectra in figures 4.3 and 4.4, with A dominant in TEY while B is dominant in FY. The zinc-blende sample Ms759 is unusual because there is almost no change in the A/B ratio, and this will be further explored in the following section.

*These were calculated for $Ga_{0.98}Mn_{0.02}N$, using mass densities of 1.035 g cm^{-3} for wurtzite and 0.9932 g cm^{-3} [17].

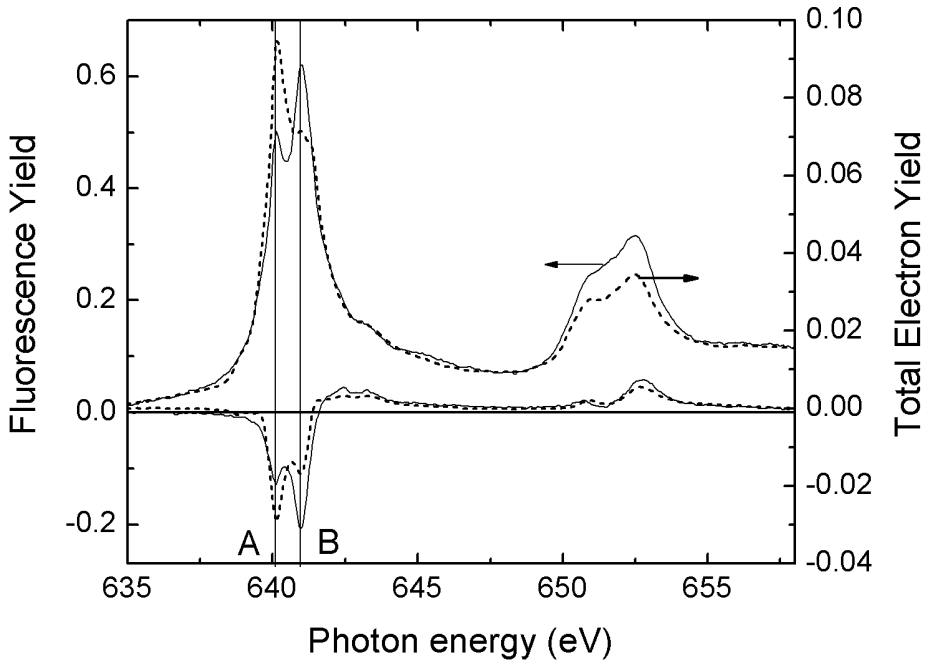

Figure 4.5: Field-summed polarization-averaged Mn $L_{2,3}$ x-ray absorption spectra of a (Ga,Mn)N zinc-blende sample measured at 10 K, using TEY (dotted lines) and FY (solid lines). XMCD spectra are shown for TEY and FY modes (lower spectra).

Branching ratios

The *branching ratio* (the ratio of the integrated x-ray absorption intensity at the L_3 edge to that of the whole $L_{2,3}$ integrated x-ray absorption intensity), is an indicator of the valency of the Mn ion: calculations of Mn d^4 show it has a significantly lower branching ratio than Mn d^5 [15].

In Section 2.7 of Chapter 2, the fluorescence measurements exhibited a lower branching ratio than for the electron yield, with the lowest value for the sample with more Mn content. This is due to distortion of the FY absorption spectra by the saturation effect. This effect complicates matters for the current study, because the branching ratio becomes an unreliable gauge of the d-electron count.

The current samples display a scatter of branching ratios, from which it is difficult to pick out a trend based upon variables such as detection mode, polytype, or As incor-

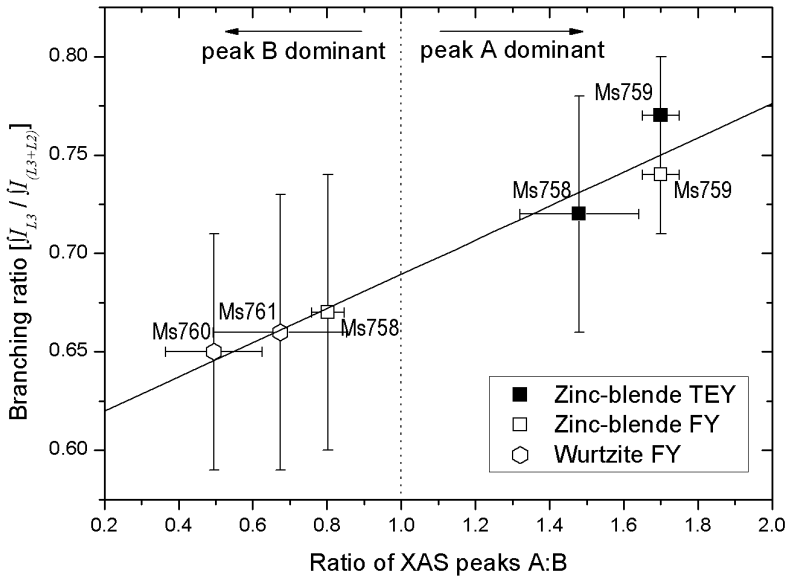

Figure 4.6: Branching ratio plotted against A/B ratio, for the zinc-blende (squares) and wurtzite (hexagons) samples, measured in TEY (filled symbols) and FY (open symbols).

poration. Already used as a crude qualitative indicator of the valency of these samples, large A/B ratios from the absorption spectra point to a prevalence of pure Mn d^5, but are similarly prone to the effects of saturation. Plotting the branching ratio against the A/B ratio may therefore give a meaningful comparison of different samples measured by the two detection modes; both should increase in magnitude as the material becomes more Mn d^5-like — and indeed the data shown in figure 4.6 seems to follow this trend. The sizable error bars reflect the large uncertainty involved in subtracting a complicated background from absorption spectra.

It was not possible to extract a branching ratio for every type of spectrum. Most of the absorption spectra required some form of background fitting and subtraction (see Section 4.2.3), and one should be aware of the large uncertainty in the branching ratios yielded by the resulting spectra. No branching ratios are included for the wurtzite TEY data, because of their very distorted backgrounds.

In figure 4.6, the wurtzite samples have both the smallest branching ratios and A/B ratios; unfortunately only FY data from these could be used in this comparison. The data

from FY give consistently smaller branching ratios and A/B ratios, with the exception of Ms759. The most interesting sample Ms758 shows the largest difference between its FY and TEY data, with the latter showing both a significantly larger branching ratio, and a shift in the dominant absorption spectrum peak from B to A. The other zinc-blende sample Ms759 interestingly shows no change in A/B ratio between the two detection modes, and the branching ratio from each are within the error bars; this would imply that Mn at the probing depths of either mode (i.e. ∼2 nm and ∼130 nm) share the same Mn valency.

Generally it can be said that for the spectra where peak B is dominant, the branching ratio is consistently smaller: this is evidence supporting the idea that peak B corresponds to Mn states closer to Mn^{3+} than pure Mn^{2+}.

4.4 XMCD results

4.4.1 FY data: Saturation correction, angle-dependence

The angle-dependent data taken for Ms761 can give information about anisotropies of the magnetic moments. Orbital and spin magnetic moments may be resolved using XMCD sum rules [18, 19]. These were most successfully applied to the FY spectra, because the TEY spectra suffered from poor signal-to-noise and prohibitively distorted background signals. However, it has already been established that distortion of FY data by the *saturation effect* makes any quantitative interpretation dubious. The distortion is most significant at grazing angles of incidence, and normal angles of fluorescence emission.

By applying a method to account for the distortion caused by saturation, it is possible to reverse the effect, to make better use of the angle-dependent FY results for sample Ms761. The saturation correction procedure is described in detail in Chapter 2; therein correction curves are calculated for the three angles of incidence, displayed in figure 2.11.

Unfortunately, unexpected behaviour is seen in the absorption spectra when the post-edge region is normalized to unity; the spectra for x-rays incident at 90°, 60° and 20° to the sample surface are shown in figure 4.7. The spectra from grazing incidences should show more strongly diminished L_3 peaks; instead the data at 60° shows the strongest L_3 peak, with the 20° data being the most curbed (as expected), but the 90° data in between.

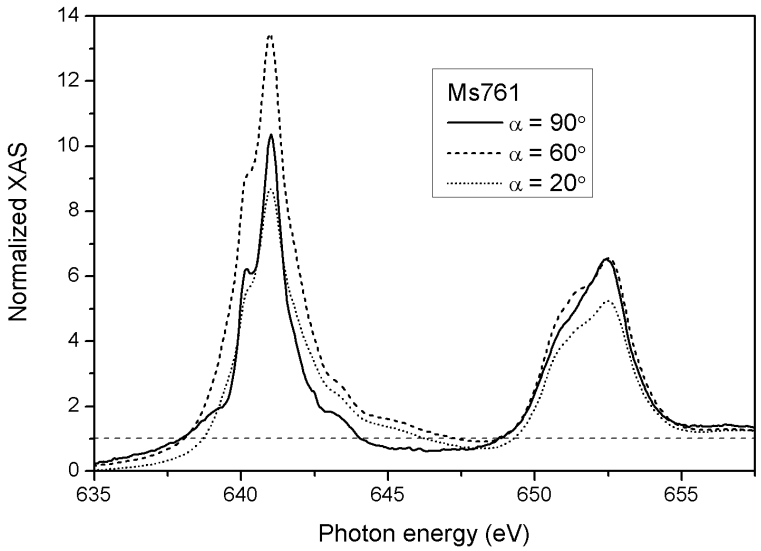

Figure 4.7: The magnetization-averaged FY absorption spectra for Ms761, obtained for x-rays incident at 90°(solid), 60° (dashes) and 20° (dots) to the sample plane, normalized to unity at the post-edge region ($\sim$ 670 eV), indicated by the dotted line.

While keeping this problem in mind, the saturation correction procedure was nevertheless performed on these data to estimate how strongly they are affected by saturation.

Figure 4.8 shows the results of saturation correction performed on the FY spectra of sample Ms761, with the sample surface at 90°, 60° and 20° to the incoming x-rays and an applied magnetic field of $\pm$5 T. The spectra taken at 60° and 20° show substantial changes upon performing the saturation correction, most notably at the L_3 peak, and to a lesser extent at the L_2 peak. These differences are also seen in the summed and difference spectra in figure 4.8. At 90° (normal incidence) there was no visible change in the lineshape of the spectra, indicating that the saturation effect is not significant at this orientation.[†] The increase in the L_3 peak intensity for the 60° and 20° data is roughly the same, even though it should be substantially greater for grazing incidences. This has occurred as a result of the unexpected difference in the absorption spectra referred to above and shown in figure 4.7.

[†]It must be noted that the raw absorption spectrum at $\alpha = 90°$ required the subtraction of a 6th order polynomial background signal, before saturation correction or sum rules could be performed. The spectra from other angles required only the removal of a straight line background.

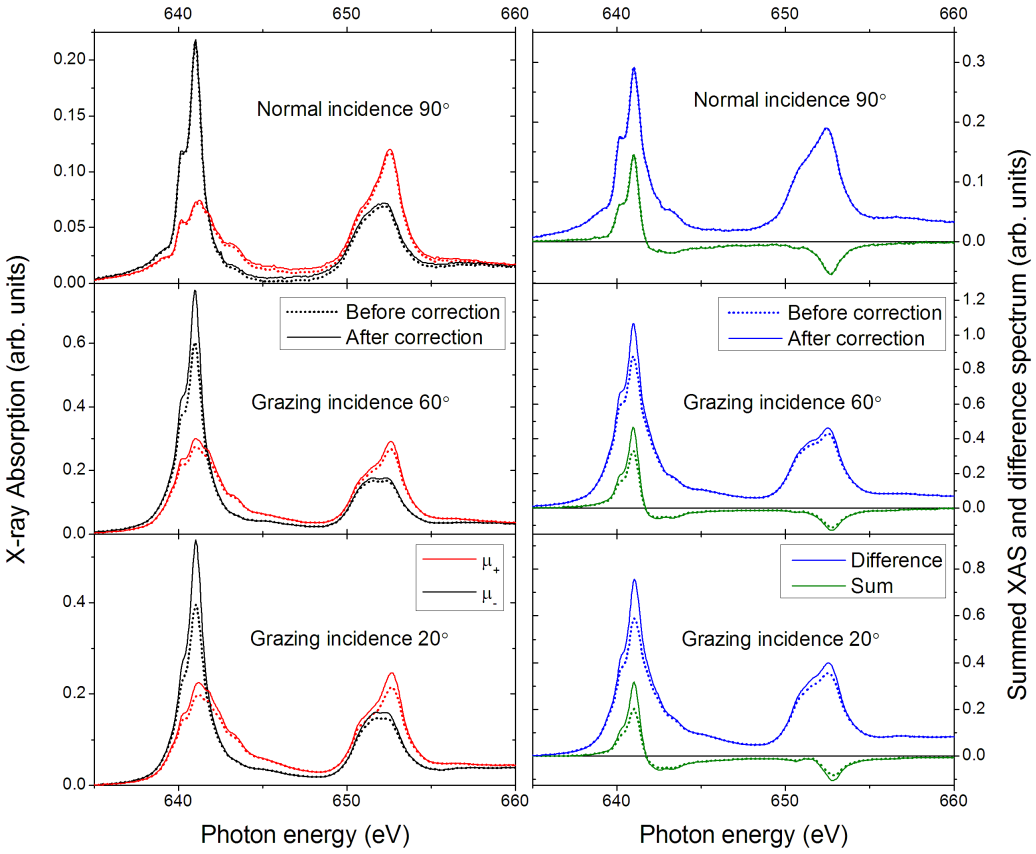

Figure 4.8: Spectra for Ms761 before (dots) and after (solid lines) saturation correction. Left panels show absorption spectra for parallel (red) and antiparallel (black) orientations of magnetic field (5 T) and photon helicity. Right panels show the corresponding difference spectra (green) and summed absorption spectra (blue). Spectra taken with photons incident normal to sample surface (top) show negligible distortion, while those at increasingly grazing angles of incidence of 60° (middle) and 20° (bottom) are altered significantly with saturation correction.

Table 4.2 shows the results of sum rules performed on the spectra in figure 4.8, before and after saturation correction. The magnetic moments are for measurements in a magnetic field of 5 T, which it should be noted is not enough to fully align all the moments in this material. At 90° the magnetic moments are calculated only for the saturation-corrected spectra, since they are virtually identical to the original spectra. For the grazing angles of incidence, the stronger L_3 peak in the corrected spectra moves both the spin and orbital magnetic moments in the positive direction (i.e. increasing and decreasing the magnitudes of m_{spin} and m_{orb} respectively). This has a very large effect on the m_{orb}/m_{spin} ratio, but the branching ratios are not so strongly affected; nevertheless this demonstrates how the saturation effect may change the apparent valence state of the absorbing ion. It is noted that the orbital moment is antiparallel to the sample magnetization, in agreement with the findings of K-edge XMCD [7].

α	Sat. Correction?	m_{orb}	m_{spin}	m_{orb}/m_{spin}	Branching ratio
90°	corrected	-0.20 ± 0.06	4.2 ± 0.5	-0.047 ± 0.015	0.54 ± 0.05
60°	original data	-0.16 ± 0.07	3.5 ± 0.6	-0.049 ± 0.021	0.65 ± 0.03
	corrected	-0.03 ± 0.03	3.8 ± 0.4	-0.009 ± 0.009	0.66 ± 0.04
20°	original data	-0.30 ± 0.08	3.2 ± 0.6	-0.094 ± 0.032	0.61 ± 0.03
	corrected	-0.21 ± 0.12	3.4 ± 0.84	-0.062 ± 0.039	0.62 ± 0.04

Table 4.2: Spin and orbital magnetic moments calculated by sum rules, along with branching ratios and m_{orb}/m_{spin} ratios for different angles of photon incidence α, calculated before and after saturation correction. The spectra were measured at an applied field of 5 T.

Unfortunately, the field-dependence of the XMCD or magnetic moments at different angles cannot be compared: the inconsistent absorption spectra shown in figure 4.7 will cause incorrect scaling of the XMCD signal at each angle. Therefore these data cannot be used to investigate anything about the magnetic anisotropy.

4.4.2 TEY data: Field-dependence of XMCD

Turning now to consider the XMCD spectra, we investigate the effect of varying the applied magnetic field on the two peaks in the L_3 region, at a constant temperature of 10 K. In this part of the analysis, the relative intensities of peaks A and B of the XMCD spectra are scrutinized; it is important that the spectra be free from saturation effects, so we consider

only the TEY spectra here.

Zinc-blende samples

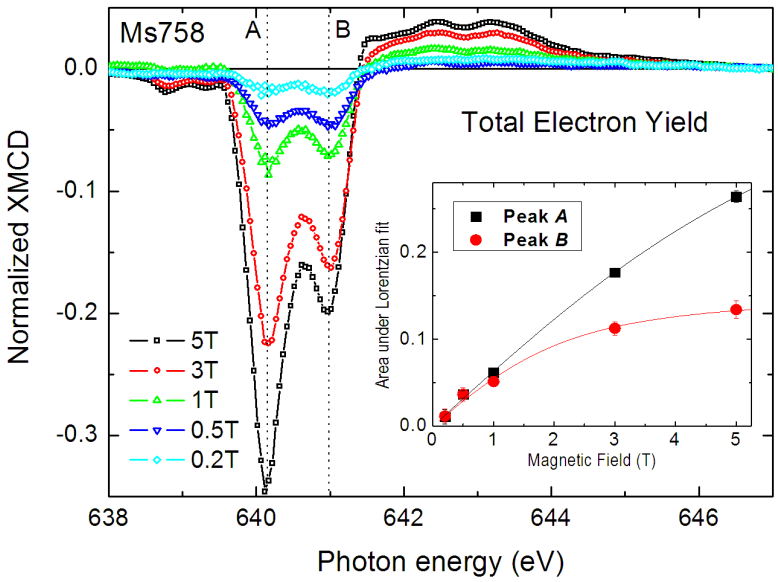

Figure 4.9: Mn L_3 XMCD spectra (normalized to the L_3 absorption edge) taken in TEY for a (Ga,Mn)N zinc-blende sample at different applied magnetic fields at 10 K. Inset: area of Lorentzian fits to the XMCD peaks occurring at A and B. Brillouin functions fits using $j = 5/2$ and $g = 2$ are shown (full lines).

Figure 4.9 shows XMCD spectra taken in TEY for the zinc-blende sample Ms758, using applied magnetic fields between 0.2 T and 5 T. The XMCD spectra shown here have been normalized so that the largest L_3 edge peak in the polarization-averaged absorption spectra is unity. It is clear that the two components show a different dependence on the applied field: at 0.5 T the two XMCD peaks are of similar size, while at 5 T peak A is almost a factor of two larger than peak B.

The close proximity of the two L_3 components causes an inevitable overlap of intensity. This means their different field dependent behaviours are not unambiguously distinguishable by simply measuring the XMCD peak heights. To separate the contribution of each peak to the total XMCD, the two main peaks in the L_3 XMCD spectra were fitted with Lorentzian functions, using constant full-width half-maximum (FWHM) and peak separa-

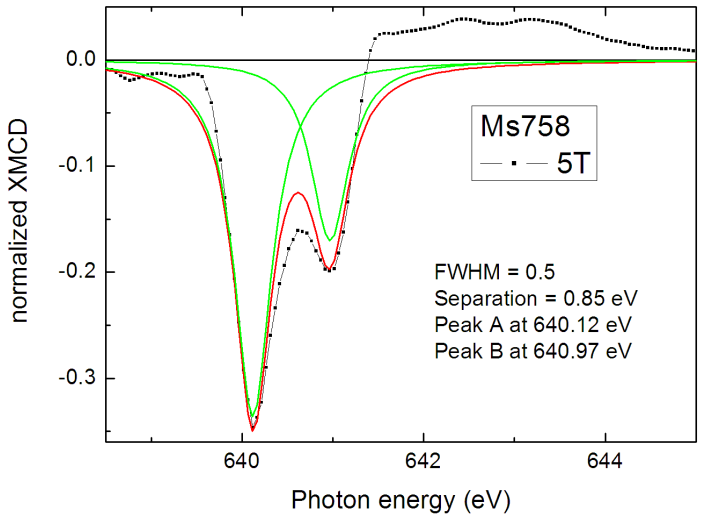

Figure 4.10: This graphs shows how the two Lorentzian curves were used to fit the features of the L_3 edge XMCD of sample Ms758.

tions (0.5 and 0.85 eV, respectively).

The L_3 region of Ms758 was satisfactorily fitted with two Lorentzian functions, centred at about 640.15 and 641 eV, as shown in figure 4.10. The magnitude of the area under each Lorentzian is plotted against the applied field in the inset to figure 4.9. Both curves show a paramagnetic response, but with a faster approach to saturation for peak B than for peak A.

For systems that have more than two possible spin-states ($j > 1/2$), a Brillouin function may be used to model their magnetization as they approach magnetic saturation. The field-dependence of the XMCD at peaks A and B were fitted with Brillouin functions, using j=5/2 and a g-factor of 2. The fitting parameters were the saturation XMCD intensity and the effective temperature of the spin system, $T_{\text{eff}} = T - T_0$, where T is the measurement temperature and T_0 is a measure of the magnetic coupling between the Mn ions. The Brillouin function is of this form:

$$B_J = 1.2 \coth\left(4.0339 \frac{B}{T_{\text{eff}}}\right) - 0.2 \coth\left(0.6723 \frac{B}{T_{\text{eff}}}\right) \tag{4.1}$$

Such an approach is widely used to describe the magnetization of paramagnetic DMS [20].

The fits are shown in the inset to figure 4.9. For peak A, $T_{\text{eff}} = 11 \pm 1$ K; this is about equal to the measurement temperature, indicating almost pure paramagnetism. For peak B, the Brillouin fit yields $T_{\text{eff}} = 4 \pm 1$ K, so $T_0 \approx 6$ K. The positive value of T_0 signifies a ferromagnetic interaction between the Mn corresponding to peak B. However, the observed paramagnetic behaviour indicates that the Curie temperature is less than 10 K.

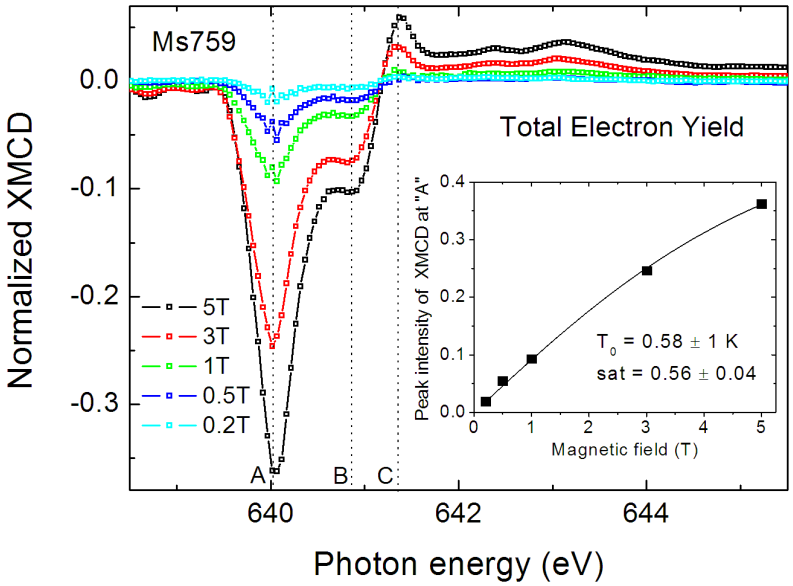

Figure 4.11: Mn L_3 XMCD spectra (normalized to the L_3 absorption edge) taken in TEY for zinc-blende sample Ms759 at different applied magnetic fields at 10 K. Inset: peak intensity at A as a function of applied magnetic field, with Brillouin function fitted using $j = 5/2$ and $g = 2$.

The field-dependence of the XMCD of the other zinc-blende sample, Ms759, is shown in figure 4.11. The shape of the spectrum varies very little for different applied magnetic fields, unlike the behaviour of the other zinc-blende sample. Because peaks A and B maintain a roughly constant ratio, there is no need to fit the peaks. Instead, the field-dependence of the intensity of peak A is plotted in the inset to figure 4.11, along with a Brillouin fit. The ferromagnetic ordering temperature obtained is $T_0 = 0.6 \pm 1$ K: this confirms the paramagnetic behaviour of peak A.

Wurtzite samples

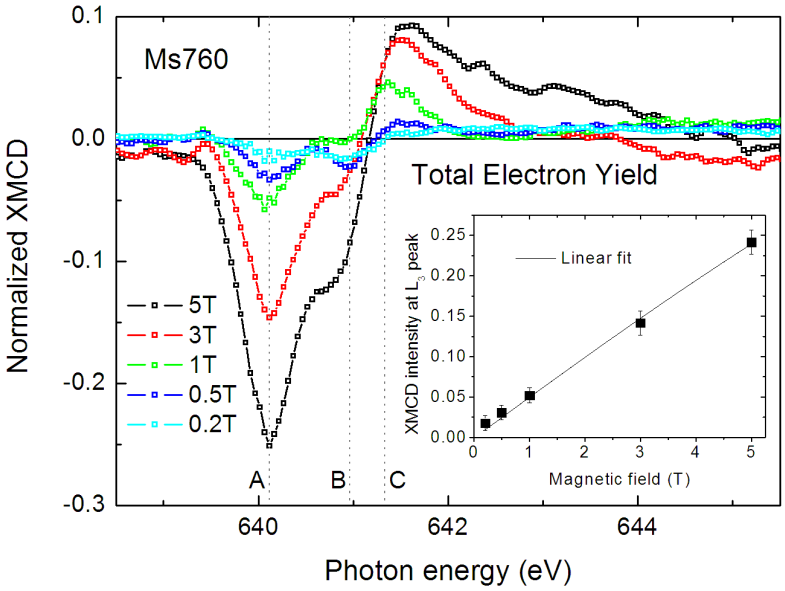

Figure 4.12: Mn L_3 XMCD spectra (normalized to the L_3 absorption edge) taken in TEY for wurtzite sample Ms760 at different applied magnetic fields at 10 K. Inset: area of Lorentzian fits to the XMCD peaks occurring at A and B, with a linear fit.

The L_3 XMCD of sample Ms760 is shown in figure 4.12. Again, peaks A and B do not display significantly different behaviour, so only the field-dependence of peak A is analyzed. The intensity of peak A against applied magnetic field is shown in the inset of figure 4.12, apparently following a linear function of magnetic field. A similar linear magnetic field dependence has been previously observed in (Ga,Mn)As [21, 22], which was concluded to be caused by antiferromagnetic coupling, corresponding to a negative ordering temperature. Because the field dependence of this sample is approximately linear, it is not useful to attempt to fit it with a Brillouin function. The upper limit of T_0 would be 0 K.

The features of the XMCD of sample Ms761 exhibit a more interesting behaviour: like Ms758, the A/B ratio in the XMCD increase with applied magnetic field. In this case it is again worth fitting Lorentzian functions to the features of the L_3 region. For this sample, field-dependent measurements were made with the x-ray incidence at 90°, 60° and 20° to the sample surface (as shown in figure 4.1). The TEY spectra of this sample were generally

very noisy with very distorted backgrounds, especially so for $\alpha = 60°$. Lorentzian fits were more easily made to the data at $\alpha = 90°$ and 20°. The XMCD at these two geometries are shown in figure 4.13. A large, broad, positive feature is present in the XMCD, occurring ∼0.48 eV above peak B. It is likely that this feature reduces the apparent intensity of peak B, thereby potentially obscuring its magnetic field dependence. The fitting range for the Lorentzian fits to peaks A and B was restricted to $\sim 639.4 - 641$ eV, to try to avoid the influence of this feature; however, its close proximity means it is still likely to curb peak B somewhat.

Sample	Incidence Angle	Peak	T_0 (K)
Ms758	60°	A	-1 ± 1
		B	6 ± 1
Ms759	60°	A	-0.6 ± 1
Ms760	60°	A	negative
Ms761	90°	A	5.1 ± 1
		B	6.4 ± 1
	20°	A	6.2 ± 1
		B	9.3 ± 1

Table 4.3: Summary of the ferromagnetic ordering temperature, T_0, obtained from the Brillouin fits to the field-dependence of each peak.

Let us first consider $\alpha = 90°$ (figure 4.13(a)). As seen in the zinc-blende Ms758, in the XMCD of peak B saturates more quickly than peak A, betraying a more ferromagnetic character: at 0.2 T the peaks are about equal, but as the field is increased towards 5 T, A becomes about twice the height of B. However, peak A also begins to saturate by 5 T. The field-dependence of the two components were separated using the same Lorentzian fitting method as for sample Ms758. The Brillouin fits, shown in the inset to figure 4.13(a), indicate that both features are weakly ferromagnetic, with a slightly higher ferromagnetic ordering temperature in peak B.

Turning to the TEY XMCD at $\alpha = 20°$ in figure 4.13(b), there is a more dramatic shift of dominance from B to A as the magnetic field is increased. Again, both peaks display some weak ferromagnetism, though the ferromagnetic ordering temperatures are slightly higher at this grazing incidence than normal incidence; in particular, it seems that peak B here saturates at a lower magnetic field.

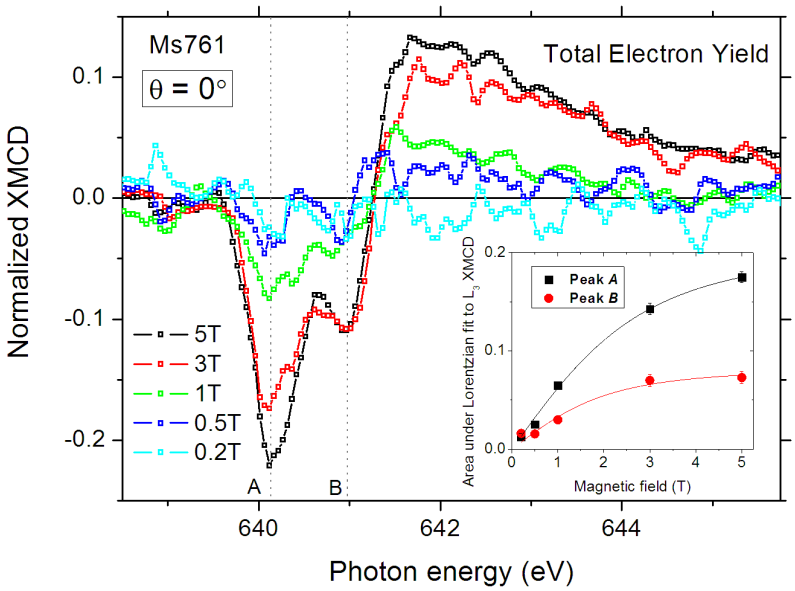

(a) $\alpha = 90°$

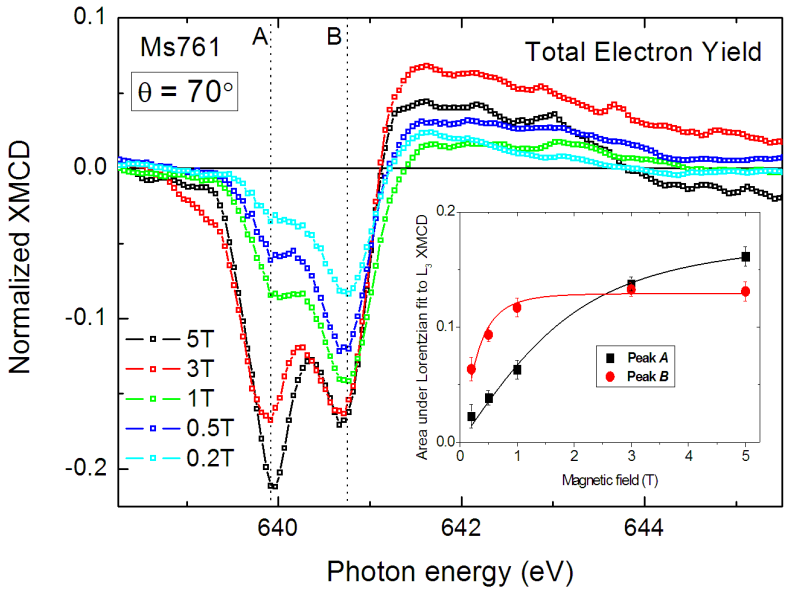

(b) $\alpha = 20°$

Figure 4.13: Mn L_3 XMCD spectra (normalized to the L_3 absorption edge) taken in TEY for wurtzite sample Ms761 at different applied magnetic fields at 10 K, for normal incidence ($\alpha = 90°$) and grazing incidence ($\alpha = 20°$).

Table 4.3 shows the T_0 values obtained from the Brillouin fits to the field dependence of the individual peaks for the zinc-blende and wurtzite samples. A negative T_0 indicates antiferromagnetic ordering. Peak B is found to have a consistently higher ferromagnetic ordering temperature, indicating it corresponds to Mn states with a ferromagnetic coupling.

In this analysis there is some uncertainty in the XMCD peak intensity, particularly for those samples which suffer from distorted absorption spectrum backgrounds (i.e. the TEY of the wurtzite samples, see figure 4.2(c)), because they must be normalized to the absorption spectrum L_3 peak.

4.5 Discussion

By considering the absorption spectra, two distinct Mn valencies are identified; by the XMCD, the magnetic coupling of the two components is inferred. The low energy L_3 peak A occurs at the expected Mn d^5 energy, and matches calculated d^5 spectra. The higher energy peak B occurs at a lower photon energy than expected for a Mn d^4 ion, and its profile does not match that of a calculated d^4 spectrum. Peak B would therefore seem to correspond to a mixed-valency ion: the energy shift of 0.85 eV is slightly less than half the separation of calculated d^5 and d^4 peaks; roughly $d^{4.5}$. This conclusion is supported by the relationship of branching ratio to A/B ratio: the spectra for which peak B is more intense exhibit a smaller branching ratio. A reduction in the branching ratio indicates a shift away from d^5 towards d^4. The wurtzite samples generally have lower branching ratios and A/B ratios than the zinc-blende samples, implying they contain a greater proportion of Mn in the $d^{4.5}$ configuration.

Comparison of the spectra from different detection modes reveals a depth-dependence of the L_3 features: the more surface-sensitive TEY spectra have a more intense peak A, while the more deeply probing FY generally exhibits a stronger peak B. The exception is for Ms759: it has the same A/B ratio for either detection mode, very strongly weighted towards A. This implies that the the Mn is of the same valency at each probing depth ($\sim$2 nm and $\sim$130 nm).

A range of magnetic behaviours are observed in these samples: para-, ferro- and anti-

ferromagnetic interactions appear to be present. The presence of As_2 flux during growth did not have a clear effect on the magnetic behaviour, nor did the type of host structure. For the samples where there is a significant difference in the behaviour of the two L_3 features, peak B consistently shows a stronger ferromagnetic character than peak A. The magnetic field-dependence of the features of the L_3 XMCD supports our interpretation of the absorption spectrum: generally the samples exhibit a paramagnetic peak A, pertaining to isolated Mn d^5 moments which are prevalent towards the surface. Peak B demonstrates a faster approach to saturation, indicating a weak ferromagnetic interaction between Mn in mixed d^4/d^5 states existing in the bulk material, mediated by a short-range double-exchange mechanism.

Ms759, which displays equally paramagnetic behaviour for A and B, is interpreted to have Mn in the d^5 state to at least a depth of ∼100 nm. The relatively poor quality of the data for Ms760 means it is uncertain whether the behaviour is paramagnetic or weakly antiferromagnetic. The absolute values of the fitting parameters obtained from the Brillouin fits are subject to some considerable uncertainty (especially in the wurtzite samples), but do serve as a useful comparison of the relative magnetic behaviours of each component of the XMCD spectra. Ferromagnetic ordering temperatures (T_0) deduced from the Brillouin fits to the features of the L_3 XMCD are expected to be close to the Curie temperature. They are in agreement with *ab initio* calculations of T_C by Sato et al. [23], assuming a short-range exchange interaction.

A GaN (0 0 0 1) surface is known as a 'polar' surface, because it is terminated by either N or, more commonly, Ga atoms. With alternative substrates, growth of N-terminated $(0\,0\,0\,\overline{1})$ GaN is possible. Polar surfaces are energetically unfavourable; to compensate for this in an N-terminated surface, there is a transfer of electrons from Ga to N. A build-up of negative charge at the surface sets up an electric field which causes electrons to move further into the bulk, forming a depletion layer just below the surface. The surface states pin the Fermi level to the middle of the band gap; this is further from the valence band than it is within the bulk. The resultant band-bending is depicted in figure 4.14. This is very well established in GaN [24], and in most other III-V semiconductors. The figure shows how the Fermi level, pinned mid-gap at the surface, intersects the Mn^{2+}/Mn^{3+} band

in the bulk; the impurity band is therefore filled near the surface to give Mn^{2+}, while both Mn^{2+} and Mn^{3+} can coexist within the bulk.

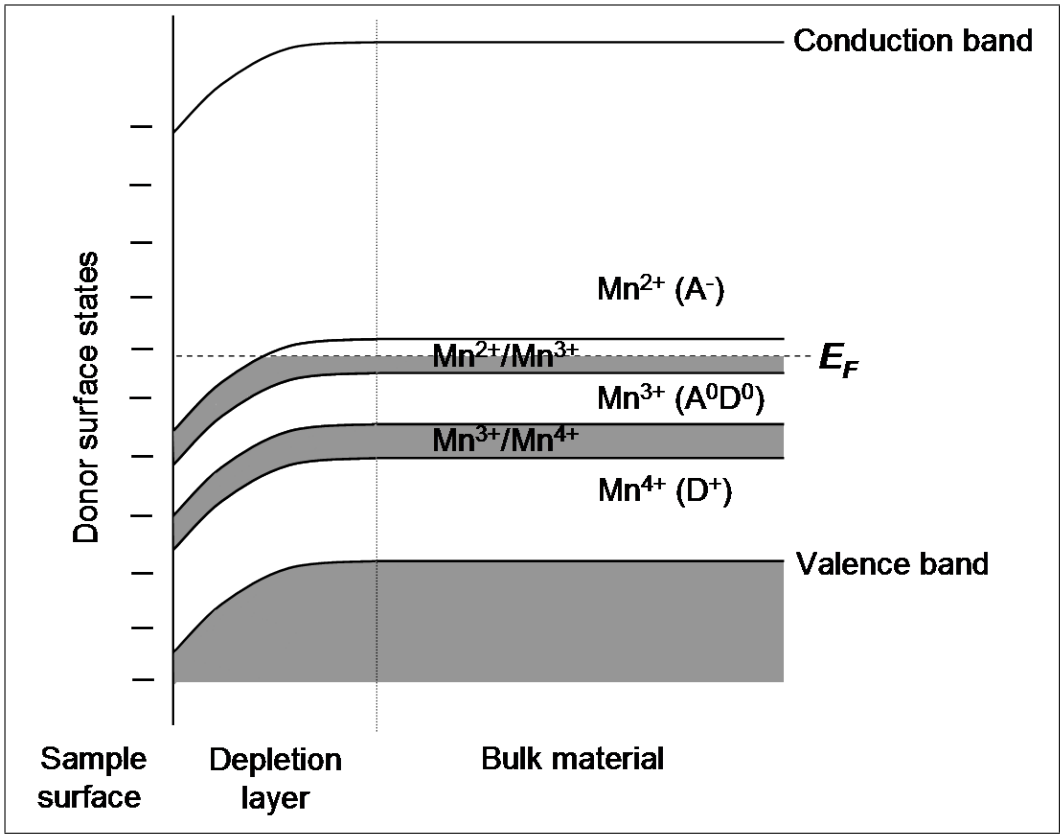

Figure 4.14: Schematic diagram of the Mn impurity bands in (Ga,Mn)N. At the surface the Fermi level is pinned mid-gap. Surface donor states can cause the bands to bend downwards towards the surface.

Towards the surface, the band-bending causes the Mn^{2+}-Mn^{3+} acceptor level to become filled, resulting in a pure Mn^{2+} configuration; in the bulk, the Fermi level intersects the acceptor level, allowing the mixed valency $Mn^{2+/3+}$ state. The width of the depleted region, and thus the relative heights of peaks A and B, will depend on the relative concentrations of surface states and Mn at the near-surface region. There is limited potential for control over these: the surface states depend somewhat on the surface preparation, which can alter the ratio of surface Ga to N atoms; the Mn concentration is very non-uniform in the top 50 nm, and SIMS data indicate there is a peak in Mn concentration at ∼20 nm below the surface. In the case of a completely filled impurity band, there is no ferromagnetic interaction between the Mn [25]. This is in agreement with the observed paramagnetic

behaviour of the low-energy peak.

It appears that there is not a link between the presence of an As_2 flux during growth and the relative intensities of the two L_3 peaks of the absorption spectrum. The large variations in lineshape of the absorption spectra are more likely to be related to surface states and Mn concentration as already mentioned, and as mentioned in Section 4.2.1, the SIMS results seem to contradict the As fluxes used in the growth conditions.

One might infer that the stark difference between the FY absorption spectra of Ms758 and Ms759, and relative similarity of Ms760 and Ms761 in figure 4.3, may imply that (Ga,Mn)N in the zinc-blende structure incorporates As into its structure more readily than into the wurtzite structure, and as such may be more receptive to modification of its band-gap for prospective enhancement of carrier-mediated ferromagnetism. However, in the case of the current materials, the As — if indeed responsible for enhancement of the Mn^{2+} concentration — only causes paramagnetic behaviour rather than ferromagnetism, since the samples are insulating and would require a much greater hole concentration in order to mirror the itinerant exchange interaction seen in (Ga,Mn)As.

4.6 Summary

The behaviour of features of the L_3 XMCD of (Ga,Mn)N have been analyzed using data from FY and TEY detection modes. Two components of the L_3 region are resolved and shown to be depth-dependent. The two components correspond to Mn ions of different valency and magnetic behaviour. Toward the surface (within the top ∼10 nm), paramagnetic Mn^{2+} ions are prevalent. In the bulk a mixed Mn^{2+}/Mn^{3+} state exists, which is weakly ferromagnetic due to carrier hopping.

References

[1] T. Dietl, H. Ohno, F. Matsukura, J. Cibert, and D. Ferrand, *Science* **287**, 1019 (2000).

[2] T. Graf, M. Gjukic, M. S. Brandt, M. Stutzmann, and O. Ambacher, *Applied Physics Letters* **81**, 5159 (2002).

[3] J. Gosk, M. Zajac, A. Wolos, M. Kaminska, A. Twardowski, I. Grzegory, M. Bockowski, and S. Porowski, *Physical Review B* **71**, 094432 (2005).

[4] T. Jungwirth, J. Sinova, A. H. MacDonald, B. L. Gallagher, V. Novák, K. W. Edmonds, A. W. Rushforth, R. P. Campion, C. T. Foxon, L. Eaves, E. Olejník, J. Mašek, S.-R. E. Yang, J. Wunderlich, C. Gould, L. W. Molenkamp, T. Dietl, and H. Ohno, *Physical Review B* **76**, 125206 (2007).

[5] J. I. Hwang, Y. Ishida, M. Kobayashi, H. Hirata, K. Takubo, T. Mizokawa, A. Fujimori, J. Okamoto, K. Mamiya, Y. Saito, Y. Muramatsu, H. Ott, A. Tanaka, T. Kondo, and H. Munekata, *Physical Review B* **72**, 085216 (2005).

[6] K. W. Edmonds, N. R. S. Farley, R. P. Campion, C. T. Foxon, B. L. Gallagher, T. K. Johal, G. van der Laan, M. MacKenzie, J. N. Chapman, and E. Arenholz, *Applied Physics Letters* **84**, 4065 (2004).

[7] E. Sarigiannidou, F. Wilhelm, E. Monroy, R. M. Galera, E. Bellet-Amalric, A. Rogalev, J. Goulon, J. Cibert, and H. Mariette, *Physical Review B* **74**, 041306 (2006).

[8] D. J. Keavney, S. H. Cheung, S. T. King, M. Weinert, and L. Li, *Physical Review Letters* **95**, 257201 (2005).

[9] J. I. Hwang, M. Kobayashi, G. S. Song, A. Fujimori, A. Tanaka, Z. S. Yang, H. J. Lin, D. J. Huang, C. T. Chen, H. C. Jeon, and T. W. Kang, *Applied Physics Letters* **91**, 072507 (2007).

[10] A. A. Freeman, K. W. Edmonds, N. R. S. Farley, S. V. Novikov, R. P. Campion, C. T. Foxon, B. L. Gallagher, E. Sarigiannidou, and G. van der Laan, *Physical Review B* **76**, 081201 (2007).

[11] L. X. Zhao, R. P. Campion, P. F. Fewster, R. W. Martin, B. Y. Ber, A. P. Kovarsky, C. R. Staddon, K. Y. Wang, K. W. Edmonds, C. T. Foxon, and B. L. Gallagher, *Semiconductor Science and Technology* **20**, 369 (2005).

[12] F. M. F. de Groot, M. A. Arrio, P. Sainctavit, C. Cartier, and C. T. Chen, *Solid state communications* **92**, 991 (1994).

[13] M. O. Krause, *J. Phys. Chem. Ref. Data* **8**, 307 (1979).

[14] R. Nakajima, J. Stöhr, and Y. U. Idzerda, *Physical Review B* **59**, 6421 (1999).

[15] B. T. Thole and G. van der Laan, *Phys. Rev. B* **38**, 3158 (1988).

[16] G. van der Laan and I. W. Kirkman, *Journal of Physics: Condensed Matter* **4**, 4189 (1992).

[17] B. Henke, E. Gullikson, and J. Davis, *Atomic Data and Nuclear Data Tables* **54**, 181 (1993).

[18] B. T. Thole, P. Carra, F. Sette, and G. van der Laan, *Physical Review Letters* **68**, 1943 (1992).

[19] P. Carra, B. T. Thole, M. Altarelli, and X. Wang, *Physical Review Letters* **70**, 694 (1993).

[20] M. Zając, J. Gosk, M. Kaminska, A. Twardowski, T. Szyszko, and S. Podsiadlo, *Applied Physics Letters* **79**, 2432 (2001).

[21] A. Oiwa, S. Katsumoto, A. Endo, M. Hirasawa, Y. Iye, H. Ohno, F. Matsukura, A. Shen, and Y. Sugawara, *Solid State Communications* **103**, 209 (1997).

[22] K. W. Edmonds, N. R. S. Farley, T. K. Johal, G. van der Laan, R. P. Campion, B. L. Gallagher, and C. T. Foxon, *Physical Review B* **71**, 064418 (2005).

[23] K. Sato, W. Schweika, P. H. Dederichs, and H. Katayama-Yoshida, *Physical Review B* **70**, 201202 (2004).

[24] T. D. Veal, P. H. Jefferson, L. F. J. Piper, C. F. McConville, T. B. Joyce, P. R. Chalker, L. Considine, H. Lu, and W. J. Schaff, *Applied Physics Letters* **89**, 202110 (2006).

[25] P. Boguslawski and J. Bernholc, *Physical Review B* **72**, 115208 (2005).

Chapter 5

Induced orbital moment of itinerant holes in (III,Mn)As

5.1 Introduction

The large magnetic anisotropy seen in (Ga,Mn)As thin films is closely correlated to the lattice symmetry. For samples in the ferromagnetic regime, a large uniaxial MCA is observed which is strongly dependent on epitaxial strain [1]. MCA arises from the spin-orbit interaction, which permits the coupling of magnetization to the symmetry of the crystal lattice, making it energetically favourable for the spins to align along certain crystallographic directions. Though there is strong experimental evidence of this coupling in (Ga,Mn)As, it is difficult to prove through direct measurement.

The Zener mean-field theory indicates that the ferromagnetism in (Ga,Mn)As is mediated by an antiferromagnetic p-d exchange coupling between the Mn d^5 moments and the itinerant holes [2]. There is some debate whether the character of the holes is closer to the impurity d states or the valence band p states [3]. For higher Mn concentrations ($> 2\%$), the prevailing view is that the holes are delocalized from the d states and are predominantly of As $4p$ character.

A semiquantitative model [4] indicates that the MCA in (Ga,Mn)As originates from a strong spin-orbit interaction in the $j = 3/2$ valence band holes, coupling the hole spins to the lattice symmetry. This model predicts a sizable magnetization of the hole subsystem,

which is of opposite sign to the Mn magnetization [5], because of the antiferromagnetic p-d exchange interaction. A Mn d^5 ion has zero orbital angular momentum ($L = 0$), negating a spin-orbit interaction in the ground-state ion. However, a small positive orbital magnetic moment is observed in the Mn $3d$ shell in (Ga,Mn)As [6], suggesting that the average $3d$ electron count is slightly higher than 5. Although there is zero anisotropy of the Mn $3d$ spin and orbital moments in (Ga,Mn)As within experimental uncertainty [7], a uniaxial anisotropy in the fine structure of the XMCD spectrum indicates that the Mn $3d$ states are sensitive to strain [8]. This supports the idea that the MCA comes from valence band states in the host crystal, but this is difficult to prove experimentally. Direct evidence is presented in this chapter.

The technique of XMCD is ideal for probing the character of the $4p$ states of the semiconductor lattice, providing element- and shell-specific information unattainable by other methods. Previously, optical magnetic circular dichroism has been used to measure the antiferromagnetic coupling between Mn local moments and holes [9], but the interband transitions probed in the optical regime make a quantitative interpretation difficult.

Recently, the presence of induced magnetic moments was clearly demonstrated in the host ions of (Ga,Mn)As, by using XMCD to separately probe the magnetic moments at the Ga and As $L_{2,3}$ edges [10]. Unfortunately, such measurements do not probe the $4p$ valence band holes: the dipolar orbital selection rule ($\Delta l = \pm 1$) allows accession of both d and s shells from the p initial state, so the experiment probes a mixture of both $3d$ and $4s$, with uncertainty as to which would dominate. The authors assert that the spectra correspond to the $4s$ final state; if this is correct, these valence band states in the semiconductor cannot explain the MCA in (Ga,Mn)As, because their orbital component of angular momentum is zero.

This present study uses K-edge XMCD to directly probe the $4p$ valence band states which are instrumental in the mediation of ferromagnetism in the (III,Mn)As family of magnetic semiconductors. The XMCD study has been published in a peer-reviewed journal [11]. Complimentary measurements are made by magnetometry and magnetotransport. These are used to characterize the magnetic anisotropies of the material, to assess the compositional quality of the material and estimate its hole concentration.

5.2 Sample details and preparation

To explore how epitaxial strain is linked to the magnetic anisotropy observed in materials such as (Ga,Mn)As, it was necessary to probe orbital magnetic moments of each element. As already mentioned, the strain is linked to the itinerant hole subsystem in (Ga,Mn)As, which can be investigated by probing the $4p$ shells of Ga, Mn and As using K-edge x-ray spectroscopy techniques. However, this requires high energy x-rays whose penetration depths (several decades of µm) are greater than the typical film thickness; this would result in a significant proportion of the absorption signal arising from the substrate if it were made of the usual GaAs. There are two ways to circumvent this problem: either remove the film from its substrate, or grow the film upon another type of substrate without Ga or As but of similar lattice parameter; both of these methods were employed in this study. The following two materials were used for the studies detailed in this chapter:

(Ga,Mn)As sample, Mn184 1 µm of (Ga,Mn)As was grown upon a 100 nm AlAs buffer layer on GaAs(0 0 1). The Mn flux during growth corresponds to an incorporated Mn content of ∼8% with respect to the As. This film was not annealed as part of its processing. The magnetotransport measurements in section 5.5 used Mn184 on its original AlAs/GaAs substrate. For the XMCD study in section 5.3.5, the thin film layer was released from the substrate by using HF to etch away the AlAs layer. It was then remounted on a sapphire substrate, glued in place using GE varnish and photoresist. In this arrangement, epitaxial strain is sacrificed to avoid complication of the x-ray absorption signal from the substrate, yet this serves as a useful contrast to the strained (In,Ga,Mn)As material.

(In,Ga,Mn)As sample, Mn386 500 nm of (In,Ga,Mn)As was grown on a 30 nm (In,Ga)As buffer layer, on an InP(0 0 1) substrate. The (In,Ga)As layer was included to aid the quality of the growth. The nominal Mn content was ∼ 6% with respect to As, estimated from the Mn flux as calibrated from SIMS data from (Ga,Mn)As. It should be emphasized that this estimation is reasonably accurate for the growth of (Ga,Mn)As material with similar nominal Mn content [12], but for (In,Ga,Mn)As the amount of Mn incorporated into the lattice may be quite different; the Mn concentration is estimated again

from SQUID measurements in section 5.4.4. The ratio of In:Ga in the magnetic layer was tuned for lattice matching to the substrate, which allows control over the epitaxial strain being compressive or tensile. Samples of this material were annealed for around 100 hours at a temperature of 190°C. This was done to improve the magnetic and electronic properties, and to allow comparison with the as-grown material. X-ray diffraction measurements of sample Mn386 confirm that this film is under a small amount of compressive strain.

5.3 XMCD study

This XMCD study directly probed the magnetism of the semiconductor valence band states, namely the As and Ga $4p$ shells; in these transitions core $1s$ electrons are excited to just above the Fermi level, referred to as the K absorption edge. The K-edge Mn XMCD was also measured to compare the sign of its dichroism with that of the other elements.

5.3.1 Experimental details

The XMCD measurements were performed on ID12 of the ESRF at Grenoble. A magnetic field of 2 T was applied along the axis of photon propagation, with photons meeting the sample at either normal incidence or a 15° grazing angle to the sample surface. The sample temperature was held at 10 K. Ga, As and Mn K-edge absorption spectra were obtained from total fluorescence yield measurements. The detector was positioned at 45° from the direction of the incident x-rays.

The photon energy was scanned over the relevant absorption edge, first with photon helicity parallel to the magnetic field, then antiparallel. The photon polarization was reversed after each energy scan. To eliminate any spurious asymmetry arising from experimental artifacts, this procedure was repeated with the direction of the magnetic field reversed. Because changing the magnetic field direction took several minutes, it was only reversed after every ten pairs of absorption spectrum scans. The XMCD signal was obtained from the difference in absorption for parallel and antiparallel alignments of the x-ray polarization vector (or *helicity*) with respect to an external magnetic field. The XMCD spectra were scaled to account for the 98% circular polarization of the photons.

5.3.2 Processing the data

The weak K-edge XMCD signal measured in this experiment demands many repeated scans to improve the signal to noise ratio, requiring continuous measurements over several hours at a time. While beamline ID12 at the ESRF has excellent beam stability, over such long data acquisition periods it is not unknown for small drifts in beam position, footprint, or photon energy to occur (see Chapter 2 for a more detailed description of problems that can occur with synchrotron measurements). Such changes can cause spurious results, therefore significantly deviating spectra must be eliminated before averaging the spectra.

In this particular experiment, ten pairs of absorption spectra (flipping the photon helicity between each scan) would be measured for a given magnetic field direction; this process was repeated for several reversals of field direction. The difference spectrum of each XANES pair was then compared with all those for like field direction, and discarded if necessary.

Weeding of unwanted spectra

A shift in alignment of the energy axis between a pair of XANES spectra often occurred during this experiment, and resulted in their difference spectrum strongly resembling the derivative of the XANES. This was the most commonly occurring problem, and it was necessary to examine and compare the individual difference spectra, and weed out any which look like the derivative of the XANES spectrum. It was also important to look out for derivative character mirrored about $y = 0$, which would arise if there were a negative shift in the photon energy.

Figure 5.1 (a) shows a pair of absorption spectra which have not suffered an energy shift; their difference spectrum, though similar to the derivative XANES, differs from it significantly: the main peak is about 0.5 eV lower on the energy axis and the post-edge behaviour is very different. This is an example of a spectrum which would be included in the averaged difference spectrum. In figure 5.1 (b), a significant shift in the energy of the K absorption edge has occurred; the resulting difference spectrum is almost identical in shape to the derivative of the XANES spectrum, shown as a thick black dashed line (scaled

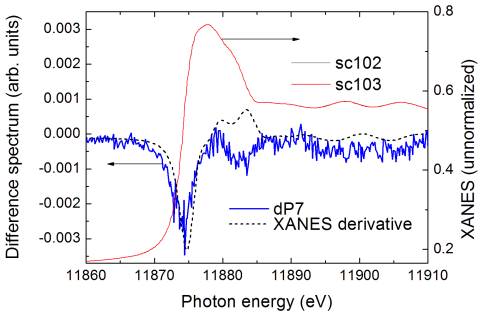

(a) Difference spectrum from a pair of absorption spectra. Notice how it is similar yet quite distinct from the derivative XANES

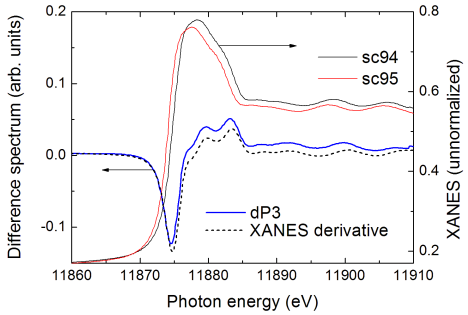

(b) Difference spectrum from a pair of absorption spectra which have suffered a significant energy shift between them. Notice it is nearly identical to the derivative, and the larger scale of the left y-axis

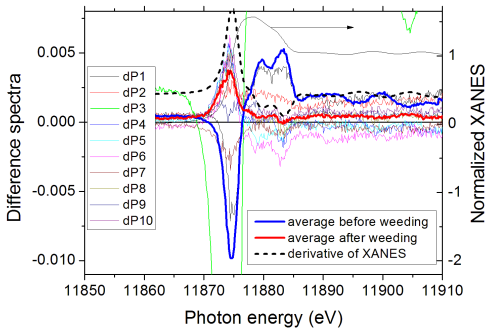

(c) B = +2T. dP1, dP3 and dP6 were weeded

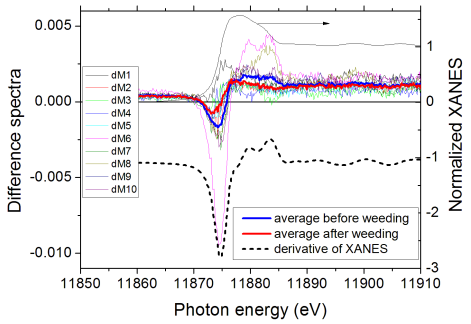

(d) B = –2T. dM6, dM8 and dM10 were weeded

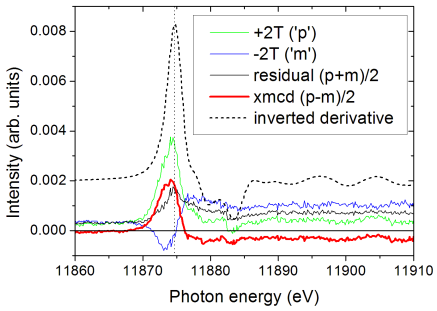

(e) Averaged diff spec from the +2T and –2T magnetic field directions, with residual spectrum (thin black line), XMCD (thick red), and derivative XANES (thick black dashes)

Figure 5.1: Weeding of 'bad' spectra from Mn386 data at grazing incidence. In (a) and (b) the thin coloured lines are the difference spectra from pairs of individual XANES scans; the average XANES (thin black line) is plotted against the right y-axis; the derivative of the average XANES spectrum is the thick black dotted line; the average difference spectrum before and after weeding are shown in thick blue and red respectively.

to aid comparison). The effect of this particular difference spectrum can be seen in 5.1 (c), where it is shown as a thin green line (off the scale of the y-axis). The average difference spectrum before weeding (thick blue line) is dominated by the green line and strongly resembles the derivative XANES. After discarding the worst-affected spectra, the average of the remaining scans is now much smaller magnitude and opposite sign. Figure 5.1 (d) shows another ten scans with the magnetic field in the opposite direction. This time, the magnitude of the derivative effects are much smaller, and so the averages before and after weeding are closer in shape, but notice that the main peak after weeding is lower in energy as noted in figure 5.1 (b). Finally, figure 5.1 (e) shows the averaged difference spectra from (c) and (d); the difference of these two is the dichroism. Also shown on this graph is the derivative XANES (inverted to aid comparison). Note that this example XMCD is only pertains to the ten difference spectra shown in (c) and (d); this weeding procedure was applied to the whole set of results for each sample at each angle of incidence.

To summarize: difference spectra were weeded if they resembled the XANES derivative, or deviated vastly from the average difference spectrum*. The intention was to eliminate the worst of the spectra, though it is quite possible that any of the spectra could have some derivative component arising from energy shifts of various magnitudes. The smaller shifts should hopefully be eliminated in the averaging of the spectra, given that the photon energy shifts could be either up or downward; also one does not wish to be overzealous with removing suspect spectra, lest some true dichroism spectra are eliminated. All the results in the following sections have been processed in this way.

5.3.3 As and Ga K-edge XMCD

Figure 5.2 shows the As K-edge absorption spectrum from the (Ga,Mn)As film; figures 5.3 (a) and (b) show the As and Ga K-edge absorption spectra from the (In,Ga,Mn)As film. There is a clear dichroism at the onset of the As absorption edge, indicating a polarization of the As $4p$ states at the valence band edge. The position and shape of the XMCD spectrum is similar for the two films, and also qualitatively similar to the main feature

*roughly speaking, this would include any difference spectra with negative peaks of <100% or positive peaks of >200% of that of the average difference spectrum for a group of scans

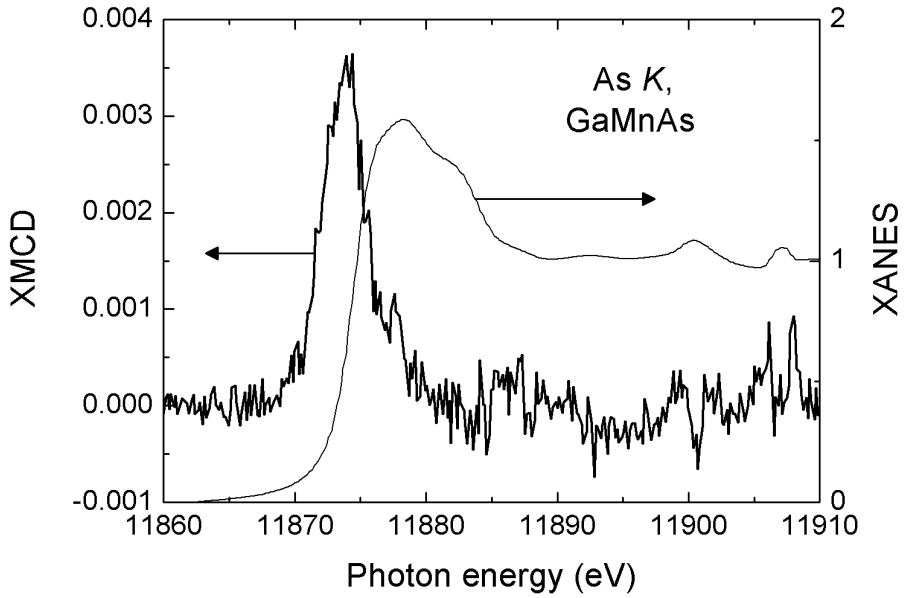

Figure 5.2: As K-edge x-ray absorption (thin line) and XMCD spectra (thick line) for (Ga,Mn)As sample, measured at normal incidence at T=10 K

observed in As L_3 XMCD from (Ga,Mn)As [10]. The As XMCD of the (Ga,Mn)As sample is somewhat noisier than that of the (In,Ga,Mn)As, because the freestanding film was somewhat buckled and the dichroism was averaged over fewer scans. From the positive sign of the dichroism we are able to conclude that the As $4p$ orbital polarization is antiparallel to the net magnetization. At the Ga edge the XMCD is much weaker, scarcely visible above the noise level.

Strain-induced anisotropy

A substantial anisotropy of the As XMCD signal is observed in the strained (In,Ga,Mn)As film, with a larger signal obtained in grazing incidence, as shown in figure 5.3(a). This stronger signal for the in-plane orbital moments is concordant with magnetometry and magnetotransport measurements, which find the easy magnetic axis of the film to be in-plane. Easy axis saturation typically occurs at a field of around 500 Oe, which to a first-order approximation matches the anisotropy field, although to rotate 100% of the

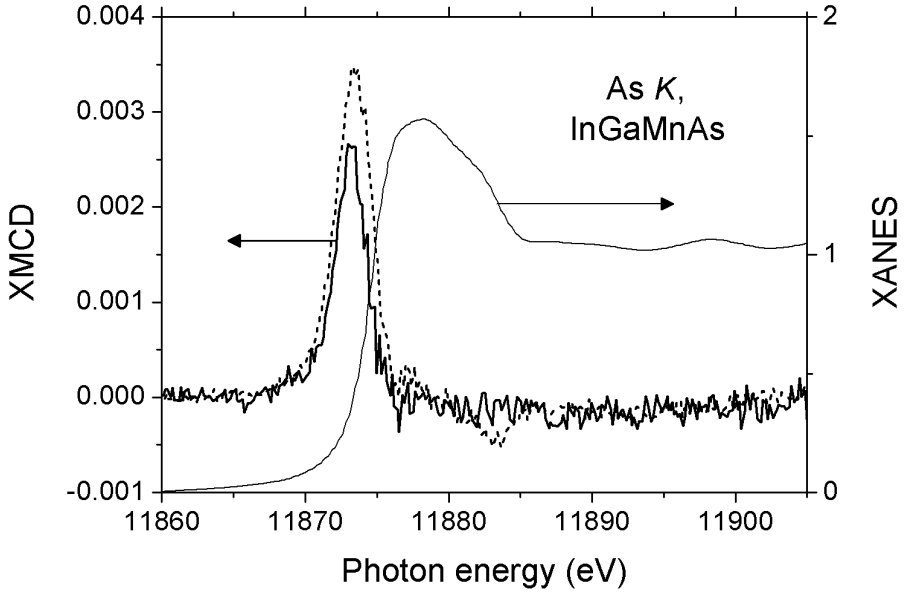

(a) As K-edge at normal (thick solid line) and grazing incidence (thick dotted line)

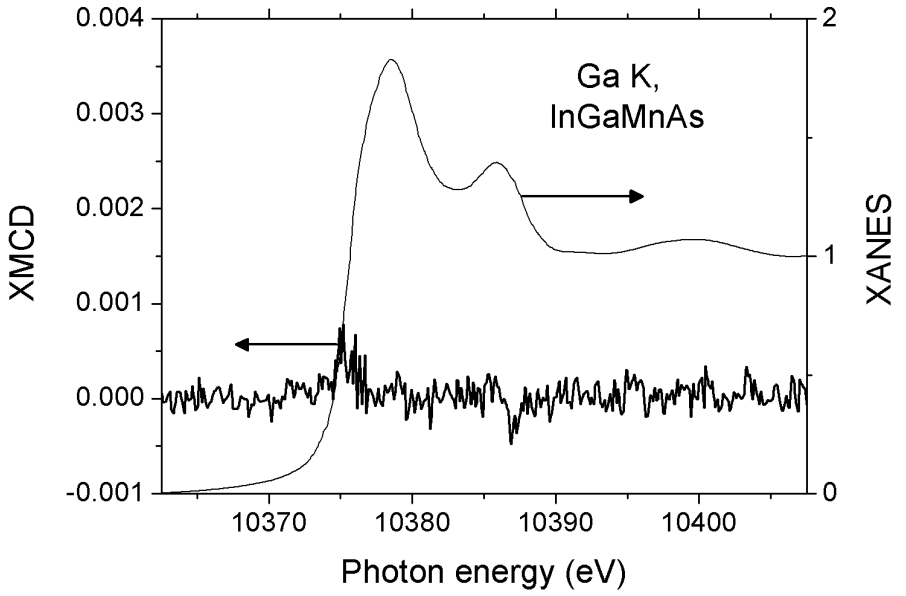

(b) Ga K-edge measured at normal incidence

Figure 5.3: XAS and XMCD spectra for (In,Ga,Mn)As sample at T=10 K

moments to become parallel to the magnetization axis may require fields greater than the 2 T used in the XMCD experiment.

Model calculations have shown that in the absence of strain, crystalline anisotropy in the hole magnetization is negligible [5]. Our present result clearly indicates that the magnetic anisotropy is reflected in the valence band of the semiconductor crystal. The complete absence of anisotropy seen in the Mn $3d$ moments in (Ga,Mn)As [7] implied that the magnetic anisotropy in this material is governed by the electronic orbitals of the semiconductor crystal valence band, rather than the magnetic impurities.

Second Phase: effect on the XMCD

Here, it is important to consider the magnetometry measurements in the later section 5.4.3. These show that the (In,Ga,Mn)As material contains a considerable proportion of Mn which may be in either a precipitate Mn_xAs_y phase or metallic Mn clusters. This might well raise some concern for the implications of the XMCD results: XAS measurements would access Mn atoms in substitutional positions and second phases alike; likewise As in a MnAs phase, if present, would be measured the same as As in anion positions of the (III,Mn)As material. However, there are two important pieces of evidence against the XMCD spectra being influenced by the second phase:

(i) the As K-edge spectra for the (In,Ga,Mn)As Mn386 exhibit the same shape as the Mn184 (Ga,Mn)As sample, which is known to have *much* less second phase from magnetometry measurements, contributing to $< 1\%$ of the remanent magnetization at $T = 10$ K (shown later in figure 5.8(a)).

(ii) the findings of section 5.4.3 indicates the second phase easy axis is perpendicular to plane, whereas the As XMCD signal is larger for the grazing angle measurements which indicates the easy axis of the (In,Ga,Mn)As is in-plane.

Therefore, although it is not desirable in this study to have a precipitate ferromagnetic second phase in the material, the results show that its has a very limited effect, if any, on the final results.

5.3.4 Orbital magnetic moments from Sum Rule analysis

The orbital sum rule for K-edge XMCD is derived from the general orbital sum rule given by equation 2.11 in Chapter 2:

$$\langle L_z \rangle = \frac{2q(6 - n_{4p})}{3r} \tag{5.1}$$

where

$$\begin{aligned} q &= \int_{4p} (\mu_+ - \mu_-) d\omega \\ r &= \int_{4p} (\mu_+ + \mu_-) d\omega \end{aligned}$$

as previously mentioned. Before the results are shown, the uncertainties involved in the calculations are considered

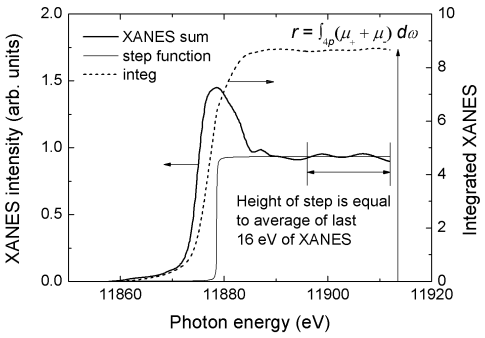

(a) Fitting of step function to the summed XANES spectrum

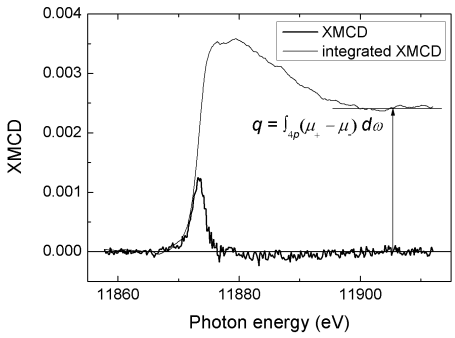

(b) The XMCD and its integrated spectrum, showing where the value q

Figure 5.4: XAS and XMCD spectra for (In,Ga,Mn)As sample

Systematic uncertainties

The quantitative application of the sum rule to these data requires knowledge of the occupancy of the final state. Atomic Ga and As are $4s^2 4p^1$ and $4s^2 4p^3$ respectively, but in the covalently bonded semiconductor GaAs, the $4p$ states of the As and Ga are mixed so each atom has $4s^1 4p^3$; therefore in the sum rule calculations $n_{4p} = 3$ is used, for both As and Ga.

It is also necessary to separate the contributions of the transitions from $1s$ to the continuum and from $1s$ to $4p$ states to apply the sum rule. To do this, a step function is removed from the summed absorption spectrum before integration to obtain r. An alternative to this crude step-function approach is described in Ref. [13]. Therein, an asymmetric function is used to model the contribution of transitions to continuum states for the absorption cross-section. However, this method was compared to the square step removal, and the difference was negligible within the experimental error.

Therefore for our purposes, the square step removal is adequate, and its precise shape is unimportant if it is symmetric, because the sum rule analysis is only concerned with the integrated intensity. The choice of the step's position on the energy axis will strongly affect the quantitative analysis. This is an easily made decision for absorption edges such as the Mn L_3-edge where a strong 'white line' exists; in the case of the K-edges of As and Ga, the energy at which absorption energy is strongest is chosen as the position of the step.

Figure 5.4(a) shows the summed XANES spectrum with its integrated spectrum and an asymmetric step function, whose height is set to the average of the last 16 eV of the XANES; figure 5.4(b) shows the XMCD with its integrated spectrum. The XMCD required some linear background subtraction to flatten the extrema of its integrated spectrum; noisy spectra meant this was subject to some amount of error, which is carried on to the determined value of q.

It is stressed that these uncertainties are sources of error in the *absolute values* of the magnetic moments, but not for their relative values, since the sum rule method is applied consistently. The sum rule analysis also required careful removal of a linear background from the XMCD spectra to account for offsets between the intensities of the XANES pairs. The raw data did not have constant point separation on the energy axis, so the spectra were interpolated to a sufficient number of points.

Results

The results from the sum rule analysis are shown in Table 5.1. The As $4p$ orbital moment is $10^{-3}\mu_B$ per As atom, while the Ga $4p$ orbital moment is an order of magnitude smaller. From room temperature Hall effect measurements (later in section 5.5.4), the hole con-

centration in the films is estimated to be around 10^{20} cm^{-3}, which gives an As $4p$ orbital moment per valence band hole of around -0.1 to -0.2 μ_B.

Extracting ground state moments from the more complex Mn K-edge XMCD would require separation of the mixed contributions from dipolar and quadrupolar transitions to the spectrum; this would be a very difficult and likely futile task, for reasons that are explained in Section 5.3.5.

Magnetic moment	Direction	Sample (a) (Ga,Mn)As	Sample (b) (In,Ga,Mn)As
$m_{\mathrm{orb}}^{\mathrm{As}}$	normal	-1.3 ± 0.2	-0.6 ± 0.1
$m_{\mathrm{orb}}^{\mathrm{Ga}}$	normal	-	-0.08 ± 0.04
$m_{\mathrm{orb}}^{\mathrm{As}}$	grazing	-	-1.0 ± 0.2

Table 5.1: As $4p$ and Ga $4p$ orbital magnetic moments ($\times 10^{-3}$ μ_B per Ga or As atom) obtained from sum rule analysis.

Saturation effect on Fluorescence Yield measurements

The samples measured in this study are relatively thick (500-1000 nm), they have a high concentration of As atoms (roughly half of the constituent atoms), the measurements include were made in FY in grazing and normal incidence. In section 2.7 of Chapter 2, such conditions were established as causes of saturation in the absorption spectra. To allay these concerns, it is necessary to estimate the size of the effect, using the same method as in section 4.4.1 of Chapter 4.

First, the penetration depth of x-rays at the As K-edge is estimated and compared to the sample thickness, to determine whether the effect is likely to be large enough to warrant consideration. The penetration depth of x-rays is estimated for $In_{0.47}Ga_{0.47}Mn_{0.06}As$, using the method described in section 2.7. The attenuation lengths of photons at 10543.5 eV (the $K_{\alpha 1}$ emission energy for As) are used to determine the absorption coefficients for the constituent elements of the material. The estimated penetration depth as $\approx 19.2 \pm 0.1$ µm, much greater than the sample thickness in normal incidence. However, at an angle of 15° to the surface, a photon would travel 4.9 µm in passing through the film. Although this is less than the escape length of fluorescent photons, it is thick enough that saturation would

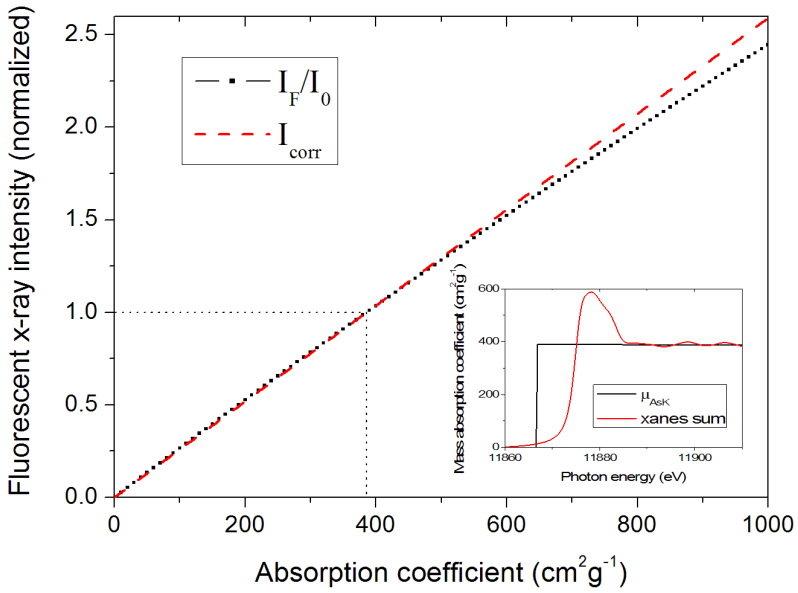

Figure 5.5: Calibration curve showing the non-linearity of I_f with respect to mass absorption coefficient. Inset: the XANES spectrum normalized μ_{AsK} taken from tabulated values [14]

be a concern.

The x-ray fluorescence intensity can be modelled as a function of the absorption coefficient of the As K-shell (μ_{AsK}), using equation 2.31 shown in Chapter 2. The relationship is shown in figure 5.5. For the conditions which are likely to yield saturation (i.e. small α, large β, $t \gtrsim$ penetration depth of fluorescence photon, large ρ, etc...), I_f becomes nonlinear as a function of mass absorption coefficient of the As K-shell, μ_{AsK}.

The inverse equation of a quadratic fit to this I_f (*i.e.* μ_{AsK} as a function of I_f) gives the function necessary to convert it to being linear with mass absorption coefficient (I_{corr}). The post-edge region of the XANES data (at ~11905 eV) are normalized to the post-edge region of μ_{AsK} obtained from tabulated mass absorption data [14] (see inset of figure 5.5), which equates both I_f and I_{corr} to unity at about 387 $\mathrm{cm^2 g^{-1}}$. The calibration curve in figure 5.5 shows I_f and I_{corr}. The small curvature to I_f visible on the graph indicates a relatively small amount of saturation occurring; the difference becomes greater for larger mass absorption coefficients ($\gtrsim$600 $\mathrm{cm^2\ g^{-1}}$). The conversion is then applied to the XANES

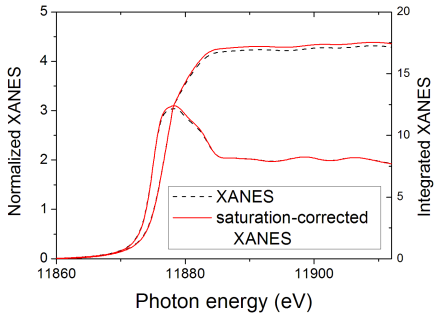

(a) The XANES summed spectrum, before (black dashes) and after (red line) saturation correction. Its integrated spectrum shows a 1.6% increase after correction.

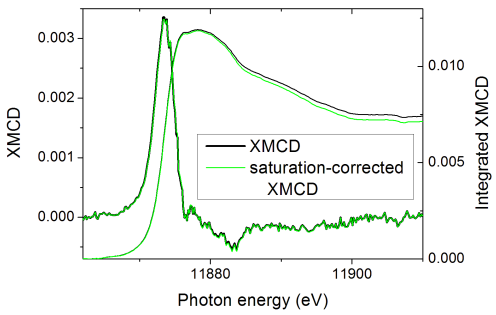

(b) XMCD before (black) and after (green) saturation correction. The integrated spectrum shows a 3.6% decrease after correction.

Figure 5.6: The saturation correction procedure applied to As K-edge spectra take at 15° photon incidence.

for parallel and antiparallel alignments of magnetization and photon helicity.

The results in figure 5.6 show the effect of the saturation correction on spectra at grazing incidence. The XANES shows only a small discernable difference, most pronounced over the peak region. The effect on the XMCD appears almost negligible, but is clearly visible in the integrated spectrum. The respective increase and decrease in the integrated XANES and XMCD spectra signifies that, in the case of this particular experiment, saturation has the effect of *increasing* the apparent magnetic moment, to the order of ∼4%. This figure is well within the error bars of the orbital magnetic moment calculated from these spectra; thus, the saturation effect is shown to be small enough to not affect the quantitative results of this study.

5.3.5 Mn K-edge XMCD

The Mn K-edge XANES and XMCD spectra for (In,Ga,Mn)As and (Ga,Mn)As are shown in figure 5.7. The main absorption edge of the K-edge XANES is due to the dipolar $1s \rightarrow 4p$ transition, while the small but clearly visible pre-edge peak is formally associated with very weak electric-quadrupolar transitions from the $1s$ core orbital to the localized $3d$ orbital. Despite this, it is possible for stronger electric-dipole character to mix in due to a direct p-d hybridization on the excited atom, so that the positive XMCD peaks occurring

in the pre-edge region could be related to the strong dipolar $1s \rightarrow 4p$ transitions.

The Mn and As K-edge XMCD are of the same sign and have comparable magnitudes. The XMCD consists of three major peaks: the first two occur around the pre-edge feature with a splitting of around $\sim$1.4 eV, and the third around the leading edge of the main peak. It has been suggested that one or two peaks present in the pre-edge region can indicate the presence of Mn^{2+} or Mn^{3+}, respectively [15]. The structure of the Mn K-XMCD is not yet well understood; though it is interesting to speculate over the mechanisms causing the splitting of the two pre-edge peaks and controlling their relative intensities, these details are beyond the scope of this work and somewhat of a distraction from the main story. Nevertheless, it is possible to infer something useful merely from the sign of the Mn XMCD peaks, compared to those of the As and Ga.

The positive sign of the As and Ga K-XMCD yields $4p$ orbital moments which are negative with respect to the net magnetization of the sample; likewise the positive sign of the Mn K-XMCD must indicate a similarly negative Mn $4p$ orbital magnetic moment. As shown in Chapter 3 and reported elsewhere [6, 16], the $3d$ orbital moment is positive with respect to net magnetization. This leads us to infer that the Mn $3d$ and $4p$ orbital moments are antiparallel, and therefore the Mn K-XMCD probes the dipolar transitions to $4p$, rather than to $3d$, permitted by direct p-d hybridization on the excited atom. Finally, the direction of the Mn $4p$ spin moment is determined by Hund's third rule: the shell is less than half-filled, so the spin lies antiparallel to the orbital moment, and hence positive with respect to the net magnetization.

The alignments of the element- and shell-resolved spin and orbital magnetic moments are compared in table 5.2. As discussed above, this present study shows that the As and Ga $4p$ orbital moments are antiparallel to the Mn $3d$ spin moment, and imply that the Mn $4p$ orbital and spin moments are respectively antiparallel and parallel to the Mn $3d$ spin moment. Additionally, the Ga and As $4s$ spin moments have been reported to be respectively parallel and antiparallel to the Mn $3d$ spin moment [10] (though this could be alternatively interpreted as being due to As and Ga spin moments of opposite sign).

It is useful to compare these conclusions about moment alignments with those first-principles calculations in Ref. [17]. Herein they determine the s, p, d and total local

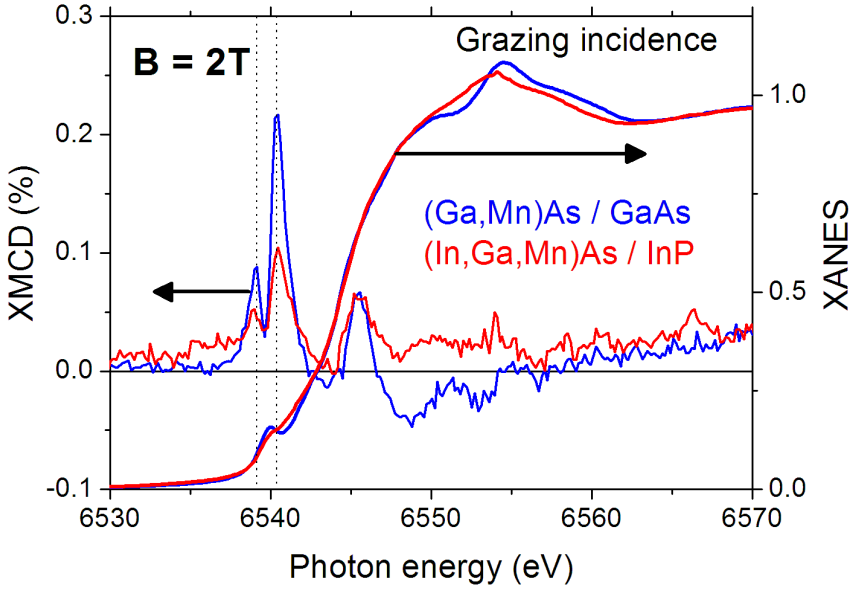

Figure 5.7: Mn K edge XMCD for (In,Ga,Mn)As and (Ga,Mn)As, measured in grazing incidence at T=10 K

moments for Mn, As and Ga in (Ga,Mn)As. Although they ignore orbital moments entirely, they state that the Mn p and d shells are parallel, and the As p moment is antiparallel to these, in agreement with our conclusions of the spin moments. However the authors report that the Ga p moment is parallel the Mn d, which contradicts our results.

	Mn $3d$	Mn $4p$	As $4s^\star$	As $4p$	Ga $4s^\star$	Ga $4p$
m_{spin}	↑	↑	↓	↓	↑	↓
m_{orb}	↑	↓	0	↓	0	↓

Table 5.2: Alignment of element- and shell-specific spin and orbital magnetic moments in (Ga,Mn)As, as determined from XMCD measurements. Note that the orientations of the As and Ga $4s$ moments ($\star$) are obtained from $L_{2,3}$ edge measurements [10], which alternatively could be interpreted as being due to As and Ga $3d$ spin moments of opposite sign.

If it were possible, we would try to determine the orbital magnetic moment of the Mn $4p$ shell from these spectra. However, the proximity of these features means there is an inevitable overlap, so that the spectral signals pertaining to the dipolar and quadrupolar

transitions are not separable, making the application of sum rules futile.

5.3.6 Summary

This study directly measured the orbital polarization of As and Ga $4p$ states in Mn doped DMS. The Ga $4p$ states are an order of magnitude less, confirming the predominantly As-like nature of the valence band itinerant holes. The As $4p$ orbital moment (under a saturating magnetic field of 2 T) is larger along the material's easy magnetic axis, in agreement with the prediction that the magnetic anisotropy is caused by the orbital momentum of holes in the semiconductor valence band.

5.4 SQUID magnetometry study

This study was used to characterize the magnetic anisotropy of the samples measured by XMCD, including estimates of the anisotropy constants and the Mn concentration.

5.4.1 Experimental details

These measurements were performed on the same samples used in the XMCD experiment. For temperature-dependent measurements of magnetization, the sample is cooled from room temperature to 2 K under a field of 1000 Oe (which gives the saturation magnetization), and warmed in remanence (which indicates the low-energy orientation of the magnetic spins and the Curie temperature). Field dependent measurements were usually made at 2 K between ±3 kOe. Measurements were made along the [0 0 1], [1 1 0] and [1 $\bar{1}$ 0] axes. The diamagnetic signal originating from the substrate was subtracted from the data; this appears as a constant offset in the temperature-dependent magnetization, and as a constant negative gradient in the field-dependent magnetization. The signal is normalized to the volume of the sample, to give the magnetic moment density in emu cm^{-3}.

5.4.2 (Ga,Mn)As sample

The freestanding (Ga,Mn)As sample was measured with the magnetic field in-plane, but since it was unstrained this does not necessarily correspond to an easy or hard mag-

netic axis. Figure 5.8(a) shows its temperature dependence in a magnetic field of 3 kOe and in remanence. The Curie temperature is about 54 K. In the figure inset, there is a temperature-dependent remanence above the transition temperature, indicating there may be a small amount ($< 1\%$) of ferromagnetic second phase in the sample. The hysteresis loop in figure 5.8(b) is fairly square with a small coercivity of ~ 30 Oe. The magnetization is measured in emu, rather than in emu cm^{-3} because the volume of the sample could not be accurately obtained.

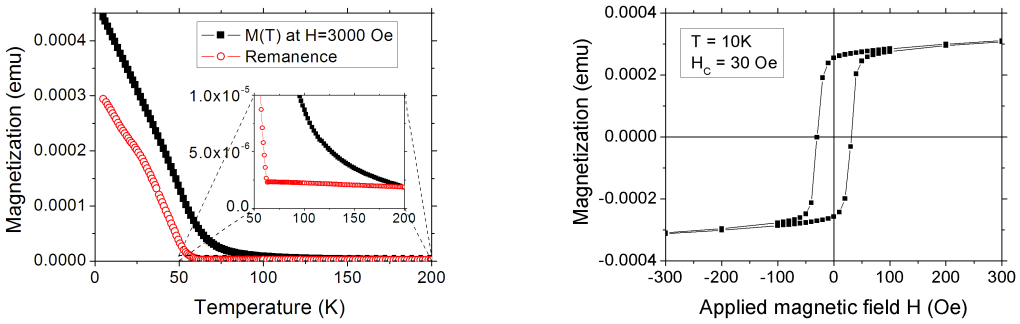

(a) M(T) at H=3000 Oe and in remanence. Inset: remanence above T_C.

(b) M(H) at $T = 10$ K.

Figure 5.8: Temperature- and field-dependent magnetization behaviour of (Ga,Mn)As sample Mn184.

5.4.3 (In,Ga,Mn)As sample

Temperature-dependent measurements of sample magnetization for Mn386 in a field of 1 kOe and in remanence are shown in figure 5.9. The perpendicular [0 0 1] axis and the two in-plane [1 1 0] and [1 $\bar{1}$ 0] axes are measured. The annealed film exhibits a clear ferromagnetic transition at about 27 K; this is very low compared to typical annealed (Ga,Mn)As material of a similar nominal Mn percentage [18], and lower than the as-grown (Ga,Mn)As film. From the magnetization in remanence it can be seen that the easy magnetic axis of Mn386 lies parallel to the short in-plane sample axis. The largest magnetization under an applied field occurs along the perpendicular and short in-plane axes.

The volume of Mn386 is estimated to be $1.454 \pm 0.08 \times 10^{-5}$cm^3. Its maximum remanence at 5 K the its maximum remanence is 17.92 emu cm^{-3}, which is 2.606×10^{-4} emu

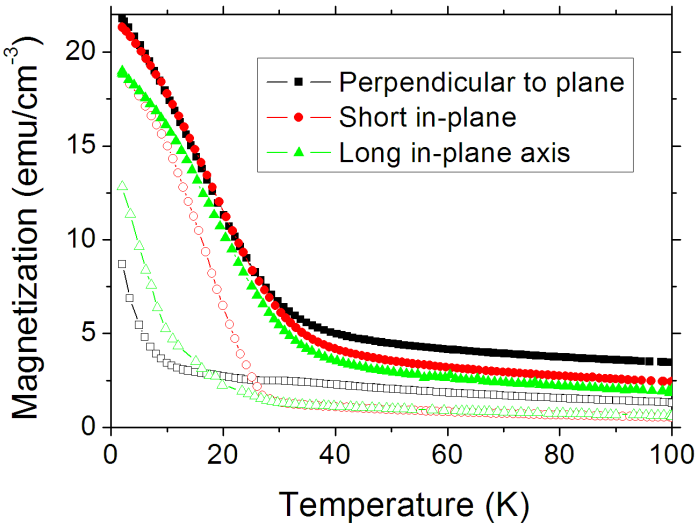

Figure 5.9: Temperature-dependent magnetization behaviour of annealed (In,Ga,Mn)As sample Mn386 for different crystalline axes, at H=1000 Oe (closed symbols) and in remanence (open symbols).

for the entire sample. This is similar to the remanence of Mn184 at the same temperature, which is 2.940×10^{-4} emu (figure 5.8(a)).

Secondary magnetic phases

For Mn386, there is a nonzero remanence along [0 0 1] above T_C, of the order of ∼20% that of the remanence at 2 K, implying that a similar proportion of the Mn in Mn386 exists in a secondary ferromagnetic phase with a much higher T_C, such as Mn_xAs_y, with the remainder incorporated substitutionally. The remanence along [0 0 1] is significantly larger than along the in-plane axes, indicating the easy axis of the second phase is perpendicular to the sample surface. Interestingly, from the magnitude of the magnetization curves in figure 5.9, it seems possible to persuade the orientation of the second phase along the short (easy) in-plane axis, but not along the long (harder) in-plane axis, for temperatures below T_C as $T \to 2$ K.

In the field-dependent measurements taken at 2 K (figure 5.10(a)) of the short in-plane direction, there is little variation in H_C between the measured axes. 3 kOe is insufficient to

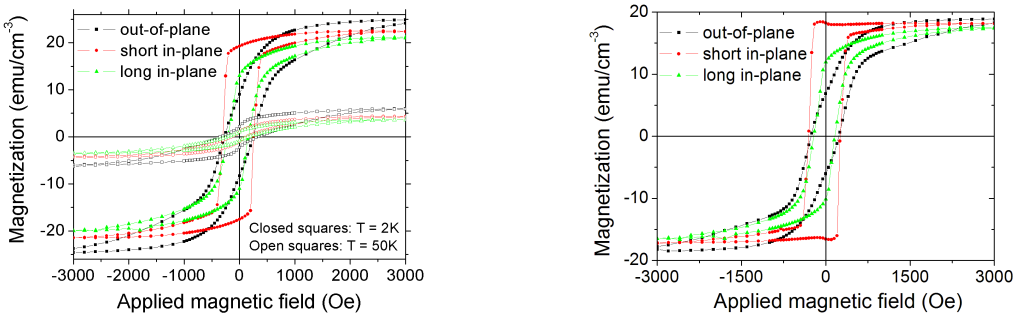

(a) $M(H)$ measured at T = 2 K and 50 K.

(b) $M(H)$ loops at 50 K subtracted from those at 2 K.

Figure 5.10: Field-dependent magnetization behaviour of (In,Ga,Mn)As sample Mn386

overcome the anisotropy field of the second phase, so in the limits of this figure the [0 0 1] axis has a greater magnetization than the in-plane axes. At 50 K the [0 0 1] direction is still the greatest remanence and also now has the greatest coercive field.

In an attempt to eliminate the ferromagnetic contribution which remains above the thin film's Curie temperature (suspected to be a secondary magnetic phase), the data from loops at 50 K were subtracted from those at 2 K, shown in figure 5.10(b), applied to all three measured axes. This results in a more typical square shape for the easy axis. The adjusted [0 0 1] loop still retains an unusual shape, perhaps caused by a transition from a multiple to single domain state when $H > 500$ Oe.

The annealing process usually enhances ferromagnetic coupling between substitutional Mn by removing compensating defects; however it is possible that it may have caused either some clustering of the Mn atoms or the precipitation of a Mn_xAs_y phase. Field-dependent measurements of a very similar sample (Mn387) revealed an increase in H_C at 100 K of $\sim 100\%$ upon annealing; an increase in H_C has been previously attributed to MnAs clusters [19]. Therefore the annealing process may have exacerbated the extent of the secondary phase in sample Mn386.

Diamagnetic substrate

Removing the diamagnetic signal from the field-dependent data was straightforward, and required only a straight line background to be fitted to the data from the [0 0 1] direction

(for the other directions the diamagnetic signal was negligible). However, this was not so simple for the temperature dependent magnetization data. The diamagnetic signal normally manifests simply as a negative offset under an applied field, but this is complicated by the presence of a secondary magnetic phase, which gives a positive offset, making it difficult to deduce the contributions from each of these sources. The magnitude of the diamagnetic signal was estimated by comparing the difference in M(H = 1 kOe) before and after the linear background subtraction. This was found to be $\sim$ 0.41 emu cm^{-3}, corresponding to a rather small offset on the M(T), around $\sim$10% of the total signal along [0 0 1].

5.4.4 Estimate Mn concentration

From measurements of the fluxes during growth (calibrated to SIMS data), it is estimated that the nominal Mn concentration in the (In,Ga,Mn)As sample Mn386 is 6%. Mn concentrations of a few percent in (Ga,Mn)As are measured reasonably accurately by SIMS [20], but the Mn atoms may not be so readily incorporated in (In,Ga,Mn)As. Annealing would cause this nominal value to be an overestimate, as demonstrated in Chapter 3. With the assumption that the entire Mn content is magnetically active and there are no interstitial Mn, it is possible to estimate the incorporated Mn from the value of the saturation magnetization:

$$\rho_{Mn} = \frac{M_{sat}}{V \times \rho_{anion} \times \mu_B \times \mu_T} \tag{5.2}$$

where the volume $V = (1.45 \pm 0.08) \times 10^{-5}$ cm^{-3}, $M_{sat} = 2.69 \times 10^{-4}$ emu, the Bohr magneton is $\mu_B = 9.274 \times 10^{-24}$ J T^{-1} and the total magnetic moment per Mn is taken as $\mu_T = 4.5\ \mu_B$/Mn. The anion density is assumed equal to $\rho_{\text{anion}} = 1.966 \times 10^{22}$ cm^{-3}, the same as InP (since the film is nearly lattice-matched to the substrate). This results in an estimated Mn concentration of 2.3 ± 0.2%, much lower than the 6% from the growth fluxes. This implies that the Mn does not incorporate into the thin film lattice when growing (In,Ga,Mn)As as well as it does in typical (Ga,Mn)As. It is also possible that there are some sources of compensation acting to lower the ferromagnetic signal, caused by defects such as interstitial Mn or possibly As antisites.

5.4.5 Anisotropy constants

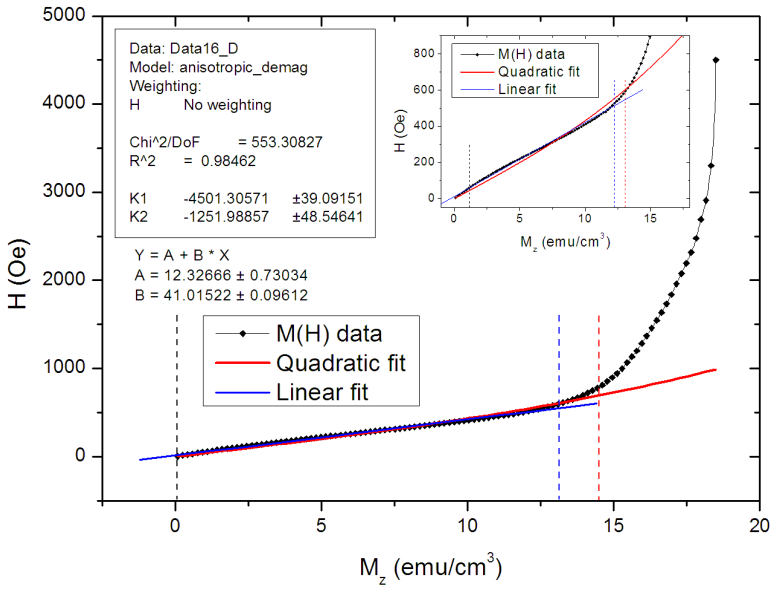

Figure 5.11: Fitting equation 5.4 to the perpendicular field-dependent magnetization data in figure 5.10(b). The ranges of the fits are marked by dotted lines.

It is possible to make a rough estimate of the anisotropy constants by treating the present material as a single-domain particle, by means of the Stoner-Wohlfarth model. This is not strictly accurate, since there is a significant hysteresis and remanence along the hard axis as seen in from figure 5.11 (a) unlike single-domain behaviour, yet it is possible to fit a straight line to the average of the up and down field scans to gain an estimate of K_1.

The free energy of the crystal in a magnetic field may be expressed as follows [21, 22]:

$$F = K_1 \cos^2\theta + K_2 \cos^4\theta - 2\pi M_{sat}^2 \cos^2\theta - M_{sat} H \cos(\theta - \phi) \tag{5.3}$$

Where θ and ϕ are the angles from the [0 0 1] axis to the magnetization vector **M** and applied field **H**, respectively; in this experiment they are equal. The first three terms are the uniaxial, biaxial and shape anisotropies respectively, the final term is due to the applied

field. Setting the derivative with respect to θ to zero allows us to find the conditions of the energy minima, i.e. $\theta = 0$ or 90°. In the case of this sample, the minimum occurs at θ = 90°, because its easy magnetic axis is in-plane. Using the substitution $M_z = M_{sat}\cos\theta$, we arrive at the equation:

$$H = 4\pi M_z - 2K_1\frac{M_z}{M_{sat}^2} - 4K_2\frac{M_z^2}{M_{sat}^4} \tag{5.4}$$

By plotting applied field H as a function of the magnetization along the z-axis M, it is possible to fit this function to the data and extract the anisotropy constants K_1 and K_2 as fitting parameters.

The data in figure 5.10(b) for the [0 0 1] axis is shown again in figure 5.11, plotted as $H(M)$. To minimize any offset of asymmetry in the H(M) curve, the up and down field sweeps were averaged, and the sign of the negative field and magnetization quadrant was reversed and averaged with the positive quadrant. A linear and a quadratic (using equation 5.4) fit are also shown. The value of K_1 extracted from the gradient of the linear fit is -4870 ± 150 erg cm^{-3}. Using the quadratic fit of equation 5.4, the anisotropy constants extracted were $K_1 = -4500 \pm 1000$ erg cm^{-3} and $K_2 = -1250 \pm 1000$ erg cm^{-3}. The uncertainties are estimated from the variation in K_1 and K_2 caused by fitting over different ranges. Comparing the relative sizes of the shape anisotropy and MCA (which equate to the the second and first terms in Equation 5.4, respectively) using this value of K_1 and at saturation ($M_z = M_{sat}$), the MCA is just over twice the magnitude of the shape anisotropy. In a high-quality single-domain (Ga,Mn)As sample, the shape anisotropy should be much smaller than the MCA, but the suspected presence of a second magnetic phase and multiple domains could explain this.

5.4.6 Summary

The magnetometry characterization of sample Mn386 leads to the following conclusions about the material. The easy magnetic axis is in-plane. The Ga:In ratio could be tuned (by including more Ga) to give samples with perpendicular anisotropy in growth, which would be interesting to measure with XMCD to compare to the present samples. There is

a substantial amount of the Mn (around 20%) in the sample which collects into a ferromagnetic second phase. The ratio of the shape anisotropy to the MCA is much larger than that of a high quality (III,Mn)As thin film, implying a rather high defect density. The apparent Mn concentration deduced from these magnetometry results is roughly 1/4 of the nominal concentration, implying either there is substantial compensation or that for (In,Ga,Mn)As there is a very low yield of Mn incorporation compared to typical (Ga,Mn)As.

5.5 Magnetotransport study

This section introduces the different type of measurements used in magnetotransport, which are used to further characterize the material and eventually determine its carrier density, a crucial value to the preceding XMCD section.

5.5.1 Background theory

Obtaining T_C from Arrott plots

The Arrott plot [23] is a useful way of using isothermal magnetotransport measurements to determine T_C. The magnetic field, $\mathbf{H}$, is not exactly linear in $\mathbf{M}$ and may be expanded in a power series:

$$\mathbf{H} = \frac{\mathbf{M}}{\chi_0} + \beta\mathbf{M}^3 + \gamma\mathbf{M}^5 + \cdots \tag{5.5}$$

where χ_0 is the initial magnetic susceptibility for fields close to zero. Considering the first two terms of the expansion, H/M is linear with M^2. Extrapolating the straight line of an isotherm to the y-axis gives $1/\chi_0$ in the zero field limit; the sign of the intercept then indicates whether the material is ferro- or paramagnetic. From equation 1.11 in Chapter 1, M can be expressed as $M = (R_{xy} - R_0B)/R_S$. The OHE term R_0B is dwarfed by the AHE near T_C, so may be ignored. As explained in Chapter 1, the proportionality of R_S to ρ_{xx} is either linear or quadratic, but is not important when making the Arrott plot.

The Anomalous Hall Effect

Equation 1.11 may be rewritten as:

$$\rho_{xy} = \rho^{OHE} + \rho^{AHE} = R_O B_z + R_S(\rho) M_z = \frac{B_z}{pe} + \gamma_H \rho_{xx}^{\alpha}(T) B_z \left(\frac{\chi_c}{T - \theta} + \chi_0 \right) \quad (5.6)$$

where p is the hole density, e is the electronic charge, B_z and M_z are the perpendicular components of external magnetic field and magnetization respectively, R_S is the anomalous Hall coefficient and θ is the Curie-Weiss temperature. γ may be taken as a temperature independent parameter provided $T > T_C$ (the Hall conductivity), χ_c is the paramagnetic susceptibility and χ_0 is a temperature independent correction to the susceptibility for fields close to zero. For systems where the skew scattering picture of carrier spin scattering applies, $R_S \propto \rho$; when the side-jump model better fits the system, $R_S \propto \rho^2$. It is assumed in this model that the OHE is independent of temperature.

Obtaining carrier density

To determine carrier density of metallic (Ga,Mn)As using magnetotransport, low temperatures and high magnetic fields are usually employed. This fully saturates the magnetization and AHE, so that the ordinary Hall coefficient R_O can be determined by the gradient of the linear behaviour of $R_H(B)$ [24, 25]. For insulating materials, an alternative method may be used, outlined by Ruzmetov *et al.* [26]. This deduces the carrier concentration by using modest magnetic fields ($\lesssim$ 1 T) and taking measurements up to well above room temperature.

Using equation 5.6, it is possible to gain a very rough estimate of the carrier concentration by simply assuming the contribution of the anomalous component of the Hall resistivity is zero at temperatures high above T_C, so that the hole density is extracted from the OHE: $\rho_{xy} = B/pe$. This method may be useful in some cases for a rough estimate of carrier density, but since the AHE is often the dominant part of ρ_{xy} even above 300 K, the estimate is subject to considerable inaccuracy.

By an alternative method, plotting ρ_{xy}/B against $\rho_{xx}^{\alpha}/(T - \theta)$ using data measured up to 350 K allows a linear extrapolation of ρ_{xy}/B to the abscissa intercept at infinite temperature, where the influence of the AHE would be hypothetically zero. Here, α determines

the linear or quadratic dependence of Hall resistivity upon ρ_{xx}, as described in section 1.6 of Chapter 1; θ is the Curie-Weiss temperature.

A more dependable approach is to evaluate the proportion of ρ_{xy} originating from the AHE at 300 K, so that p may be determined from the OHE with a reasonable level of confidence. This is achieved by considering how much the AHE reduces from its saturated value at $T \lesssim 4\ K$, accordingly determined by the reduction in ρ_{xy} and $\mathbf{M}$ from $T \approx$4 K to 300 K. Equation 5.6 may be re-written:

$$\begin{aligned} \frac{\rho_{xy}}{B} &= R_O + \frac{R_S(\rho_{xx})M_z}{B} \\ &= \frac{1}{pe} + Q\rho_{xx}^{\alpha}(T)B_J \end{aligned} \tag{5.7}$$

where the Brillouin function $B_J = M_z/M_{sat}$ as defined in equation 1.3. This is evaluated for an applied field $B = 0.4$ T and a temperature of $(T - T_C)$, where $T_C = 21$ K. The temperature independent constant $Q = \frac{\gamma M_{sat}}{B}$. The value of e is taken to be $+1.602\times10^{-19}$, so that a p-type material would give a positive value of p.

Using measurements of ρ_{xx} and ρ_{xy} at low and high temperatures gives two simultaneous equations, which allow Q to be eliminated so that p can be determined. The results of this method are shown in section 5.5.4.

5.5.2 Experimental details

Preparation of samples

The samples measured in this part of the study were Hall bars fabricated from cuts of Mn386 and Mn184 (on its original AlAs/GaAs substrate). 8-probe Hall bars were fabricated, etched parallel to one of the cleft edges, with a ratio of probe separation to Hall bar width of 6.3 squares. Samples were measured with the magnetic field applied in-plane along the long axis of the Hall bar, and out-of-plane. Longitudinal voltage V_{xx} was measured between neighbouring probes and the Hall voltage V_{xy} was measured across probes perpendicular to the current direction.

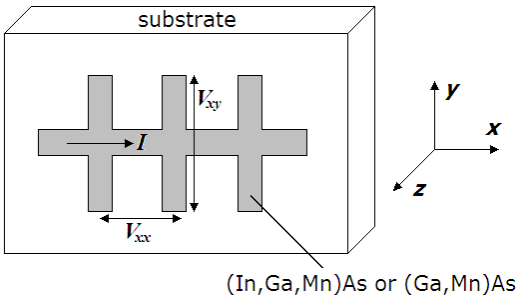

Figure 5.12: Diagram of a Hall bar, showing which probes are used to record V_{xx} and V_{xy}; the magnetic field could be applied along the x, y or z direction.

Experimental procedure

Magnetoresistance measurements were made of R_{xx} and R_{xy} as the temperature or applied magnetic field were scanned, with different orientations of the magnetic field to the sample plane. For temperature dependence, the measurements were recorded at a constant field of 0.1 T as the temperature was slowly reduced from room temperature to below 4 K.

5.5.3 Temperature and field dependence

Determining Curie Temperature

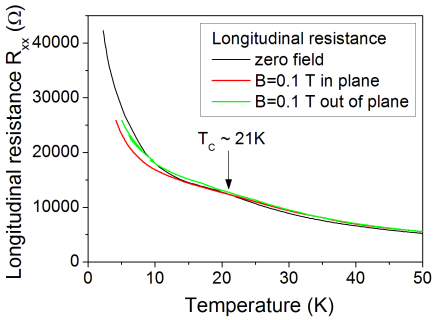

(a) Temperature dependence of R_{xx}

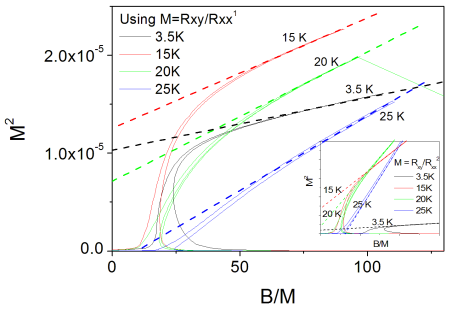

(b) Isotherms of R_{xx} and R_{xy} presented in an Arrott plot, with $M = R_{xy}/R_{xx}$. Inset: the same data is plotted using $M = R_{xy}/R_{xx}^2$

Figure 5.13: Determining the Curie temperature of the sample.

The longitudinal resistance ρ_{xx} in figure 5.13 (a) increases with decreasing temperature,

with a slight shoulder occurring at T_C and an ensuing sharper increase as $T \to 0$. This is a clear indication that the sample is insulating, because in a conducting sample the magnetoresistance would peak around T_C and then fall again as the temperature is reduced further [27].

From the temperature dependent measurements and Arrott plots seen in figure 5.13 (a) and (b), the Curie-Weiss temperature of the sample was determined to be about 21 $\pm$ 2 K. This is slightly lower than the piece of the same sample measured by SQUID and XMCD; this difference may be explained by slight variations in composition of the parent wafer of these pieces of Mn386.

Longitudinal resistance, $\rho_{xx}(B)$

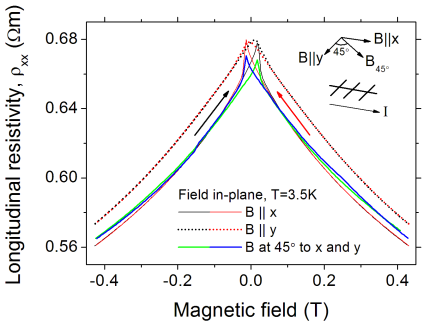

(a) Magnetic field applied in the sample plane

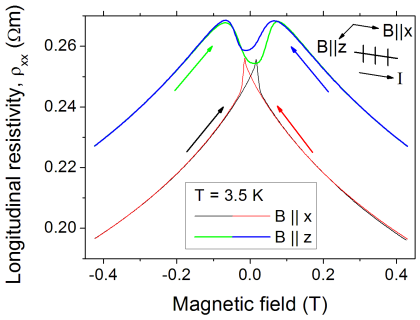

(b) Magnetic field applied parallel to the current direction or perpendicular to sample plane

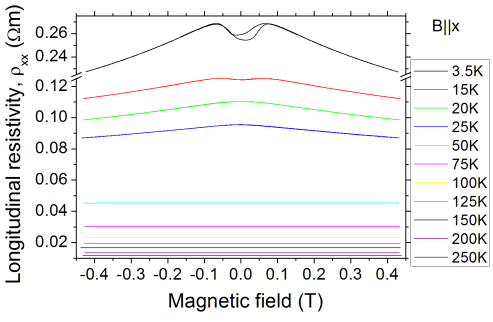

(c) Range of temperatures from 3.5 to 300 K

Figure 5.14: Field dependence of R_{xx} for Hall bar made from Mn386 at 3.5 K. Black and red arrows indicate 'up' and 'down' field-scans respectively.

The field dependence of longitudinal resistivity ρ_{xx} at low temperature ($\sim$4 K), shown in figure 5.14 (a) and (b), confirms the easy magnetic axis is orientated in-plane, indicated by sharp peaks at the low field region; the hard axis is along [0 0 1], exhibiting broader rounded peaks centred at a greater applied field. This is in agreement with the magnetometry results of section 5.4.3. All orientations exhibit a strongly negative magnetoresistance; this result may be understood in terms of the increasing magnetic field aligning the spins which reduces spin-dependent scattering, and is typical of ferromagnetic (Ga,Mn)As [27]. A sizable anisotropic magnetoresistance (AMR) is evident between the perpendicular and in-plane field directions in figure 5.14(b). The conspicuous difference in the magnetoresistance between figure 5.14 (a) and (b) is because a different set of contacts to the Hall bar were used for these measurements.

Figure 5.14(c) shows the field dependence of ρ_{xx} at a range of temperatures from 3.5 K to 300 K, and it can be seen that the negative magnetoresistance flattens with increasing temperature; though not possible to see from the scale of the figure, above 150 K the magnetoresistance becomes positive, remaining so to 300 K.

Hall resistance, $\rho_{xy}(B)$

When the magnetic field is applied perpendicular to the plane (along [0 0 1]), the Hall resistance as a function of the applied field strength is an antisymmetric hysteresis loop. This is because at low temperatures where the AHE dominates, ρ_{xy} scales with $\mathbf{M}$. Above the Curie temperature, as the AHE diminishes, the dependence of ρ_{xy} upon $\mathbf{B}$ becomes more apparent. Figure 5.15(a) shows the ρ_{xy} against applied field at a range of temperatures from 3.5 K to 300 K.

Figure 5.15(b) shows the Hall resistance as a function of magnetic field applied along [0 0 1] at $\sim$3.5 K, shown as dashed black and red lines. It can be seen that the Hall resistance generally describes an open, antisymmetric hysteresis loop which saturates at around 0.1 T. However, the loop is not centred at the origin and slopes downwards at large positive and negative magnetic field. This offset and slope are due to a slight misalignment of the Hall bar arms in the x direction, so that the transverse resistance signal contains a very small component of the negative magnetoresistance. In figure 5.15(b), the data from

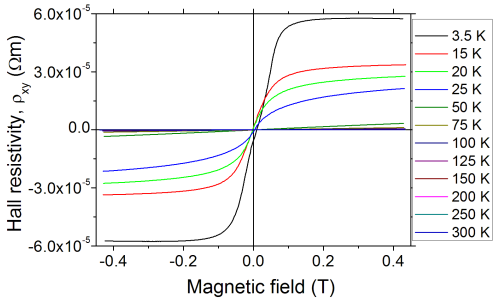

(a) Averaged 'up'- and 'down'-scans of ρ_{xy} at T = 3.5 to 300 K

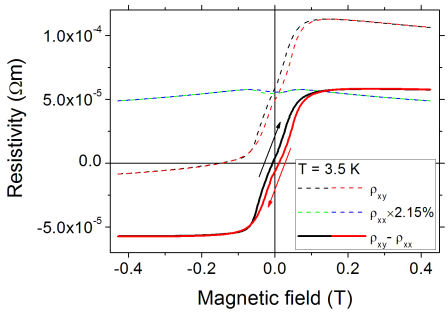

(b) Scaled component of ρ_{xx} subtracted from ρ_{xy}, for $T = 3.5\ K$

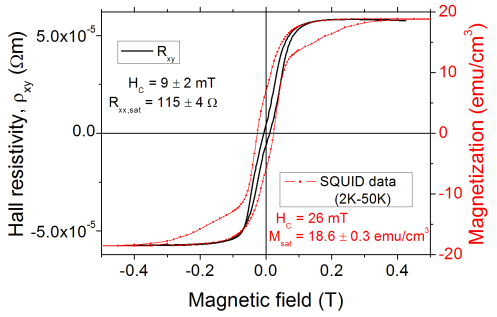

(c) Hall resistivity overlaid with SQUID magnetometry data, both with field applied perpendicular to the sample plane

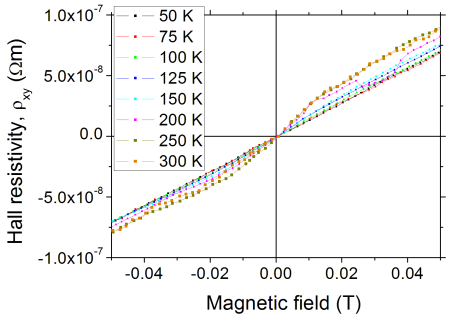

(d) Field dependence of ρ_{xy} over a range of temperatures from 50 K to 300 K, normalized to allow comparison of the low-field behaviour

Figure 5.15: Hall resistivity against applied field, applied along [0 0 1].

the longitudinal resistance has been scaled to 2.15% and subtracted from the unscaled ρ_{xy} data. In the resulting ρ_{xy} loop (thick black and red lines), the influences of the negative magnetoresistance and the asymmetric behaviour of ρ_{xx} near zero field have been eliminated.

In Figure 5.15(c) it can be clearly seen that the field dependence of ρ_{xy} resembles the magnetization hysteresis loops from magnetometry, sharing the same approximate saturation field but with a notably smaller coercive field: $H_C = 9 \pm 2$ mT measured from ρ_{xy}, ~26 mT by magnetometry. This discrepancy may be attributed to the existence of a secondary magnetic phase in this sample, which is not detected by transport because the Coulomb repulsion at the interface of the clusters causes the current to bypass them. As mentioned in section 5.4.3, the existence of a second phase is known to cause an en-

hancement of the coercivity in (Ga,Mn)As samples [19]; while an attempt was made to eliminate its influence from the SQUID data, it is possible that this was not adequate to fully account for it.

Although the Hall resistance should be linear with applied magnetic field at temperatures far above T_C, figure 5.15(d) clearly shows a 'kink' or deviation from linear behaviour between $B = \pm 0.01$ T. This feature is most clearly manifest at $T = 300$ K; it is probably always present but swamped by the large dominant linear signal at lower temperatures. This feature is observed in both upward and downward scans of the magnetic field, so it is not likely to be an artefact or mistake of the analysis procedure. A way to explain this apparent persisting magnetization-dependence might be that at 300 K the ferromagnetic second phase, while not usually detected in transport, might be weakly magnetizing the paramagnetic (In,Ga,Mn)As.

Relative sign of OHE and AHE

In bulk (Ga,Mn)As, the OHE and AHE are generally always parallel [27,28]. In the case of (In,Mn)As they can be parallel [29] or antiparallel [30]. Since the main sample of interest in this study is (In,Ga,Mn)As, it is useful to know which is the case for this hybrid DMS. Using a 50 nm (Ga,Mn)As sample with 8% Mn content Mn012 as a reference, it is found that both the (In,Ga,Mn)As sample Mn386 and the (Ga,Mn)As sample Mn184 used for the XMCD study share the same positive gradient in the field dependence of Hall resistivity as exhibited by the reference sample.

5.5.4 Estimation of carrier density

By determining the carrier density p of this material, we may determine if there is any compensation of holes compared to typical p of (Ga,Mn)As [24, 26] and (In,Mn)As [27, 31] samples of a similar Mn doping level to the present material. Moreover, by deducing the hole density it is possible to use the values in table 5.1 to estimate the orbital magnetic moment per As $4p$ hole.

As outlined in section 5.5.1, there are several ways of estimating the carrier density. First, ρ_{xy}/B was plotted against ${\rho_{xx}}^{\alpha}/T - \theta$, with the aim of linearly extrapolating ρ_{xy}/B

to infinite temperature, where the line meets the abscissa. Unfortunately the results of this method are very sensitive to the choice of α and θ: the value of p is negative if $\alpha = 1$, and for $\alpha = 1.5$ or 2 it requires an unrealistic value for θ to keep a linear relationship. As such, this method is not appropriate to determine the hole concentration with the available data.

The more dependable approach is to evaluate the proportion of ρ_{xy} originating from the AHE at 300 K, so that p may be determined from the OHE with a reasonable level of confidence. This is achieved by considering how much the AHE reduces from its saturated value at $T \lesssim 4\ K$, accordingly determined by the reduction in ρ_{xy} and $\mathbf{M}$ from $T \approx$4 K to 300 K.

Measurements at $T = 3.5$ K and $T = 300$ K are inserted into equation 5.7 to give:

$$\frac{\rho_{xy}(3.5\ K)}{B} = \frac{1}{pe} Q \rho_{xx}^{\alpha}(3.5\ K) \tag{5.8}$$

$$\frac{\rho_{xy}(300\ K)}{B} = Q \rho_{xx}^{\alpha}(300\ K) B_J \tag{5.9}$$

The hole density is then evaluated for the limiting values of the exponent α. For $\alpha = 1$, $p = 1.219 \times 10^{20}\ cm^{-3}$;for $\alpha = 2$, $p = 5.372 \times 10^{19}\ cm^{-3}$.

These estimates are within the expected range of hole densities, as suggested from the literature [24, 26, 27, 31].

5.5.5 Summary

This magnetotransport study has shown that the easy axis of the (In,Ga,Mn)As is in-plane, in agreement with magnetometry. The [0 0 1] ρ_{xy} hysteresis loop shape differs somewhat from the hysteresis seen by magnetometry because the former (generally) neglects contributions from clusters. Finally, the estimation of hole density is about $(9 \pm 4) \times 10^{19}$ cm^{-3}, with the assumption that the AHE is best described by the skew scattering process. This magnitude of hole density is about the same as that of as-grown (Ga,Mn)As material of the same nominal Mn concentration [32]. Knowledge of the hole density allows an estimation of the orbital magnetic moment *per hole* in the As 4p band.

References

[1] A. Shen, H. Ohno, F. Matsukura, Y. Sugawara, N. Akiba, T. Kuroiwa, A. Oiwa, A. Endo, S. Katsumoto, and Y. Iye, *Journal of Crystal Growth* **175-176**, 1069 (1997).

[2] T. Dietl, H. Ohno, F. Matsukura, J. Cibert, and D. Ferrand, *Science* **287**, 1019 (2000).

[3] T. Jungwirth, J. Sinova, A. H. MacDonald, B. L. Gallagher, V. Novák, K. W. Edmonds, A. W. Rushforth, R. P. Campion, C. T. Foxon, L. Eaves, E. Olejník, J. Mašek, S.-R. E. Yang, J. Wunderlich, C. Gould, L. W. Molenkamp, T. Dietl, and H. Ohno, *Physical Review B* **76**, 125206 (2007).

[4] M. Abolfath, T. Jungwirth, J. Brum, and A. H. MacDonald, *Phys. Rev. B* **63**, 054418 (2001).

[5] C. Śliwa and T. Dietl, *Physical Review B* **74**, 245215 (2006).

[6] K. W. Edmonds, N. R. S. Farley, T. K. Johal, G. van der Laan, R. P. Campion, B. L. Gallagher, and C. T. Foxon, *Physical Review B* **71**, 064418 (2005).

[7] K. W. Edmonds, G. van der Laan, A. A. Freeman, N. R. S. Farley, T. K. Johal, R. P. Campion, C. T. Foxon, B. L. Gallagher, and E. Arenholz, *Physical Review Letters* **96**, 117207 (2006).

[8] K. W. Edmonds, G. van der Laan, N. R. S. Farley, E. Arenholz, R. P. Campion, C. T. Foxon, and B. L. Gallagher, *Physical Review B* **77**, 113205 (2008).

[9] J. Szczytko, W. Mac, A. Twardowski, F. Matsukura, and H. Ohno, *Phys. Rev. B* **59**, 12935 (1999).

[10] D. J. Keavney, D. Wu, J. W. Freeland, E. Johnston-Halperin, D. D. Awschalom, and J. Shi, *Physical Review Letters* **91**, 187203 (2003).

[11] A. A. Freeman, K. W. Edmonds, G. van der Laan, R. P. Campion, A. W. Rushforth, N. R. S. Farley, T. K. Johal, C. T. Foxon, B. L. Gallagher, A. Rogalev, and F. Wilhelm, *Physical Review B (Condensed Matter and Materials Physics)* **77**, 073304 (2008).

[12] R. P. Campion, K. W. Edmonds, L. X. Zhao, K. Y. Wang, C. T. Foxon, B. L. Gallagher, and C. R. Staddon, *Journal of Crystal Growth* **247**, 42 (2003).

[13] G. Dalba, D. Diop, P. Fornasini, A. Kuzmin, and F. Rocca, *Journal of Physics: Condensed Matter* **5**, 1643 (1993).

[14] B. Henke, E. Gullikson, and J. Davis, *Atomic Data and Nuclear Data Tables* **54**, 181 (1993).

[15] A. Titov, X. Biquard, D. Halley, S. Kuroda, E. Bellet-Amalric, H. Mariette, J. Cibert, A. E. Merad, G. Merad, M. B. Kanoun, E. Kulatov, and Y. A. Uspenskii, *Physical Review B* **72**, 115209 (2005).

[16] S. Ueda, S. Imada, T. Muro, Y. Saitoh, S. Suga, F. Matsukura, and H. Ohno, *Physica E* **10**, 210 (2001).

[17] S.-H. Wei, X. G. Gong, G. M. Dalpian, and S.-H. Wei, *Physical Review B* **71**, 144409 (2005).

[18] T. Jungwirth, K. Y. Wang, J. Mašek, K. W. Edmonds, J. König, J. Sinova, M. Polini, N. A. Goncharuk, A. H. MacDonald, M. Sawicki, A. W. Rushforth, R. P. Campion, L. X. Zhao, C. T. Foxon, and B. L. Gallagher, *Physical Review B* **72**, 165204 (2005).

[19] K. Y. Wang, M. Sawicki, K. W. Edmonds, R. P. Campion, A. W. Rushforth, A. A. Freeman, C. T. Foxon, B. L. Gallagher, and T. Dietl, *Applied Physics Letters* **88**, 022510 (2006).

[20] L. X. Zhao, R. P. Campion, P. F. Fewster, R. W. Martin, B. Y. Ber, A. P. Kovarsky, C. R. Staddon, K. Y. Wang, K. W. Edmonds, C. T. Foxon, and B. L. Gallagher, *Semiconductor Science and Technology* **20**, 369 (2005).

[21] X. Liu, Y. Sasaki, and J. K. Furdyna, *Physical Review B* **67**, 205204 (2003).

[22] L. V. Titova, M. Kutrowski, X. Liu, R. Chakarvorty, W. L. Lim, T. Wojtowicz, J. K. Furdyna, and M. Dobrowolska, *Physical Review B* **72**, 165205 (2005).

[23] A. Arrott, *Physical Review* **108**, 1394 (1957).

[24] K. W. Edmonds, K. Y. Wang, R. P. Campion, A. C. Neumann, C. T. Foxon, B. L. Gallagher, and P. C. Main, *Applied Physics Letters* **81**, 3010 (2002).

[25] K. W. Edmonds, R. P. Campion, K. Y. Wang, A. C. Neumann, B. L. Gallagher, C. T. Foxon, and P. C. Main, *Journal of Applied Physics* **93**, 6787 (2003).

[26] D. Ruzmetov, J. Scherschligt, D. V. Baxter, T. Wojtowicz, X. Liu, Y. Sasaki, J. K. Furdyna, K. M. Yu, and W. Walukiewicz, *Physical Review B* **69**, 155207 (2004).

[27] H. Ohno, *Journal of Magnetism and Magnetic Materials* **200**, 110 (1999).

[28] H. Ohno, A. Shen, F. Matsukura, A. Oiwa, A. Endo, S. Katsumoto, and Y. Iye, *Applied Physics Letters* **69**, 363 (1996).

[29] H. Ohno, H. Munekata, T. Penney, S. von Molnár, and L. L. Chang, *Phys. Rev. Lett.* **68**, 2664 (1992).

[30] T. Jungwirth, Q. Niu, and A. H. MacDonald, *Phys. Rev. Lett.* **88**, 207208 (2002).

[31] A. Oiwa, A. Endo, S. Katsumoto, Y. Iye, H. Ohno, and H. Munekata, *Phys. Rev. B* **59**, 5826 (1999).

[32] K. W. Edmonds, K. Y. Wang, R. P. Campion, A. C. Neumann, N. R. S. Farley, B. L. Gallagher, and C. T. Foxon, *Applied Physics Letters* **81**, 4991 (2002).

Chapter 6

Conclusions

This thesis has addressed several important issues of III-V DMS, including the magnetization deficit in (Ga,Mn)As, the origin of its strain-induced magnetic anisotropy, and the magnetic coupling of Mn ions in GaN.

An anisotropic Mn L-edge XMLD signal was reported for the ferromagnetic semiconductor (Ga,Mn)As in Chapter 3. The $\langle 1\,1\,0 \rangle$ to $\langle 1\,0\,0 \rangle$ in-plane directions yield XMLD spectra with substantially different lineshapes and opposite signs. The results are compared to atomic multiplet calculations for Mn $3d^5$ in cubic crystal-field symmetry, which establishes the anisotropy in XMLD as a single-ion effect induced by the crystal field. The anisotropic XMLD may be useful for determining the spin orientation in antiferromagnetic materials [1]. The magnitude of the XMLD signal indicates a large, partially localized moment. Small changes in the XMLD structure suggest that the samples with lower carrier concentration are more localized.

In (Ga,Mn)As, interstitial Mn couple antiferromagnetically with substitutional Mn, forming $\mathrm{Mn_{Ga}}$-$\mathrm{Mn_I}$ pairs. The XMCD and XMLD signals were both suppressed in as-grown (Ga,Mn)As, and both increased upon annealing. This indicated that the antiferromagnetically coupled $\mathrm{Mn_{Ga}}$-$\mathrm{Mn_I}$ pairs have have no preferred axis of orientation. The data combined from XMCD, XMLD and SQUID magnetometry experiments were analyzed to determine if the interstitial-substitutional coupling is the sole source of the magnetization suppression. In heavily Mn-doped material, the magnetic moment 'per ferromagnetic Mn atom' was suppressed, even after accounting for the interstitial Mn. Conversely, in lightly-

doped material, the moment of the ferromagnetic Mn did not seem to be suppressed; the magnetization suppression seemed to come only from the formation of 'spin-zero' Mn_{Ga}-Mn_I pairs.

Hence, the magnetization deficit was generally attributed to Mn_{Ga}-Mn_I pairs. We have identified a possible case where the local moment is also reduced from its full atomic value, caused by non-collinearity of the ferromagnetic ordering. This could be further explored by measuring samples with even higher Mn concentrations. A high energy resolution and photon flux are essential to obtain spectra of sufficient quality to perform this type of analysis; spectral broadening and a low signal-to-noise ratio can distort the apparent relationship of I_{XMCD} to I_{XMLD}.

The XMCD study of (Ga,Mn)N in Chapter 4 yielded several insights into the electronic and magnetic characteristics of the Mn dopant in GaN. Two peaks are commonly observed in L-edge spectroscopy studies of (Ga,Mn)N. The lower energy peak occurs at the expected energy for a Mn d^5 absorption spectrum. The energy separation of the two peaks is approximately half the calculated separation of Mn d^4 and d^5 peaks, so it is inferred that the higher energy peak corresponds to a mixed valence state of Mn^{2+}/Mn^{3+}. The simultaneous collection of FY and TEY data was essential to access Mn ions at different depths within the material. The intensities of the peaks of interest differed for the two detection modes, indicating a Mn^{2+}-rich surface region and a mixed Mn^{2+}/Mn^{3+} state within the bulk. It was found that the two L_3 peaks in the XMCD spectra responded differently to an applied magnetic field. The higher energy peak had a consistently stronger ferromagnetic coupling than the lower energy one, for all samples. The extracted ferromagnetic ordering temperature, a close indication of the Curie temperature, is in accordance with *ab initio* calculations which assume a short-range interaction. This agrees with the suggestion that the mechanism behind the weak ferromagnetism observed in (Ga,Mn)N is double-exchange.

The picture that emerges is a coexistence of Mn^{2+} and $Mn^{2+/3+}$ in (Ga,Mn)N. The valence of the Mn is depth-dependent as a result of band-bending caused by deep donor levels at the surface. There are reports that only either Mn^{2+} or Mn^{3+} is present in (Ga,Mn)N; these may be limited by the use of only one measurement mode and its associated prob-

ing depth. Since itinerant exchange is not possible for the Mn^{2+} deep acceptor level in (Ga,Mn)N, only a weak ferromagnetic coupling is allowed by double exchange between states of mixed valency. Consequently, (Ga,Mn)N is a useful system to study, but is unlikely to have applications in spintronic devices.

The spin-orbit interaction is very important in the DMS (Ga,Mn)As. The Mn $3d$ moments have no intrinsic contribution to the magnetic anisotropy. Instead, it is thought that the MCA stems from a strong spin-orbit coupling between the Mn $3d$ spins and the semiconductor valence band p states, permitted by p-d hybridization. The orbital polarization of the valence band p states is measured in Chapter 5. The As K-edge XMCD of (In,Ga,Mn)As displayed a substantial anisotropy, mirroring the bulk magnetic anisotropy observed by magnetometry. This constitutes direct evidence of the coupling of the magnetization of a ferromagnetic impurity to the orbital moment of the host semiconductor lattice, confirming the origin of the MCA in DMS. The hole concentration was estimated from magnetotransport measurements. Since the holes predominantly reside at the top of the valence band on As sites, an estimate of the orbital magnetic moment per As $4p$ hole could be made. The orbital moment of the Ga $4p$ shell was found to be an order of magnitude less than that of the As, demonstrating that the valence band holes have predominantly As character. In the K-edge XMCD of Mn, strong peaks occur at photon energies coinciding with the XANES pre-edge region, which is formally associated with weak quadrupolar transitions to $3d$ states. The strength of these peaks could be caused by intensity mixing in from the preponderant dipolar transitions, permitted by direct on-site p-d hybridization.

A systematic study of the effects of strain on the As and Ga orbital magnetic moments would be desirable. By varying the Ga:In ratio for several different (In,Ga,Mn)As samples, it would be possible to tune the epitaxial strain from compressive to tensile; ideally a range of strain anisotropies could be investigated, with the easy magnetic axis crossing over from in-plane to perpendicular. As with this study, x-rays at normal and grazing incidence would be used to probe the orbital moment anisotropy. Additionally, the effect of Mn dopant concentration could be investigated by measuring 2% and 8% Mn samples, each under

tensile and compressive strains. Accurately achieving the desired Mn concentration is not a simple matter for (In,Ga,Mn)As; it seems the Mn does not incorporate as readily as for (Ga,Mn)As, so some calibration growths might be needed to find the necessary Mn/Ga/In fluxes. Hopefully, the proportion of Mn incorporated in the secondary phase could be minimized or eliminated. Although the results of XMCD are not compromised by the presence of a second phase, it is desirable to have a pure single-phase crystal to work with. The (In,Ga,Mn)As sample studied here was probably not optimally annealed, so higher Curie temperatures should be attainable. If samples with higher Curie temperatures could be grown (ideally at least ∼80 K), it would be worth measuring the temperature dependence of the XMCD.

The current prospects for room-temperature ferromagnetism in Mn-doped III-V DMS appear to be waning. Itinerant exchange does not occur in (Ga,Mn)N. For (Ga,Mn)As, the Curie temperature is limited by the increasing difficulty to incorporate Mn substitutionally in GaAs as its concentration is increased. Alternative combinations of group III and group V elements may yet allow improvement of the maximum T_C. For example, it has been predicted that (Ga,Mn)(As,P) could yield higher Curie temperatures due to a similar band-gap to (Ga,Mn)As but a smaller lattice parameter, which may give fewer compensating defects [2]. Magnetic spectroscopy techniques using synchrotron radiation will be invaluable for strengthening our understanding of these.

References

[1] G. van der Laan, E. Arenholz, A. Schmehl, and D. G. Schlom, *Physical Review Letters* **100**, 067403 (2008).

[2] J. Mašek, J. Kudrnovský, F. Máca, J. Sinova, A. H. MacDonald, R. P. Campion, B. L. Gallagher, and T. Jungwirth, *Physical Review B (Condensed Matter and Materials Physics)* **75**, 045202 (2007).

Appendix A

Acronyms

AHE anomalous Hall effect

AMR anisotropic magnetoresistance

DLM disordered local moment

DMS dilute magnetic semiconductors

DOS density of states

EXAFS extended x-ray absorption fine structure

FY fluorescence yield

GMR giant magnetoresistance

MBE molecular beam epitaxy

MCA magnetocrystalline anisotropy

MAE magnetocrystalline anisotropy energy

OHE ordinary Hall effect

SIMS secondary ion mass spectroscopy

SQUID superconducting quantum interference device

TEY total electron yield

XAS x-ray absorption spectroscopy

XANES x-ray absorption near-edge structure

XMCD x-ray magnetic circular dichroism

XMLD x-ray magnetic linear dichroism

Appendix B

List of Publications

- A. A. Freeman, K. W. Edmonds, G. van der Laan, R. P. Campion, A. W. Rushforth, N. R. S. Farley, T. K. Johal, C. T. Foxon, B. L. Gallagher, A. Rogalev, and F. Wilhelm, *Valence band orbital polarization in III-V ferromagnetic semiconductors*, PRB **77** 073304 (2008)

- A. A. Freeman, K. W. Edmonds, N. R. S. Farley, S. V. Novikov, R. P. Campion, C. T. Foxon, B. L. Gallagher, E. Sarigiannidou, and G. van der Laan, *Depth dependence of the Mn valence and Mn-Mn coupling in (Ga,Mn)N*, Physical Review B **76**, 081201(R) (2007)

- A. A. Freeman, K. W. Edmonds, G. van der Laan, N. R. S. Farley, T. K. Johal, E. Arenholz, R. P. Campion, C. T. Foxon, and B. L. Gallagher, *Giant anisotropy in x-ray magnetic linear dichroism in (Ga,Mn)As*, Physical Review B **73** 233303 (2006)

- N. R. S. Farley, K. W. Edmonds, A A Freeman, G. van der Laan, C. R. Staddon, D. H. Gregory, and B. L. Gallagher, *Magnetic properties of solgel-derived doped ZnO as a potential ferromagnetic semiconductor: a synchrotron-based study*, New Journal of Physics 10 055012 (2008).

- K. W. Edmonds, A. A. Freeman, N. R. S. Farley, K. Y. Wang, R. P. Campion, B. L. Gallagher, C. T. Foxon, G. van der Laan and E. Arenholz, *Secondary magnetic phases in (Ga,Mn)As determined by x-ray magnetic circular dichroism*, Journal of Applied Physics **102** 023902 (2007)

- K. W. Edmonds, G. van der Laan, A. A. Freeman, N. R. S. Farley, T. K. Johal, R. P. Campion, C. T. Foxon, B. L. Gallagher, and E. Arenholz, *Angle-dependent x-ray magnetic circular dichroism from (Ga,Mn)As Anisotropy and identification of hybridized states*, Physical Review Letters **96** 117207 (2006)

- K. Y. Wang, M. Sawicki, K. W. Edmonds, R. P. Campion, A. W. Rushforth, A. A. Freeman, C. T. Foxon, B. L. Gallagher, and T. Dietl, *Control of coercivities in (Ga,Mn)As thin films by small concentrations of MnAs nanoclusters*, Applied Physics Letters **88** 022510 (2006)